DEPARTMENT OF EXPERIMENTAL MEDICINE

PhD COURSE IN EXPERIMENTAL MEDICINE

Curriculum of

MOLECULAR AND CELLULAR PATHOLOGY OF AGE-RELATED DISEASES

A Multi-Faceted Approach to Uncover Novel Vulnerabilities in Uveal Melanoma: From Etiology to the Identification of Prognostic Biomarkers.

Candidate

Dr. Marianna Ambrosio

Tutor

Prof. Barbara Marengo

Co-tutor

Dr. Ulrich Pfeffer

PhD Program Coordinator

Prof. Ernesto Fedele

Academic Year 2024-2025

ABSTRACT

Background. Uveal Melanoma (UM) is the most common primary intraocular malignancy in adults. Its clinical management, in the metastatic state, remains a significant challenge, characterized by inherent aggressiveness and limited systemic therapeutic options. Despite substantial progress in genomic prognostic stratification, the unpredictable nature of the disease in some patients and the lack of effective treatments underscore the urgent need for a deeper understanding of both etiological factors and molecular mechanisms driving progression.

Aims. This study adopted a multi-faceted approach focused on three main objectives: i) To elucidate the potential etiological role of Blue Light (BL) exposure; ii) To develop genetically defined cellular models to reproduce the key molecular alterations of aggressive UM (GNA11 and BAP1 mutations); and iii) To identify and validate novel prognostic biomarkers within the Chromosome 8q gain region.

Results. BL exposure in melanocyte models generated mutational signatures (SBS1 and SBS5) aligned with those typical of UM, providing direct evidence that BL may act as an "additional hit" in tumorigenesis, distinct from UV-induced damage. Unexpectedly, a BL complex oxidative stress response was observed, characterized by an overall increase in ROS but a reduction in H_2O_2 production. In parallel, the first GNA11Q209L cellular models were successfully generated to reproduce the key alterations driving aggressive UM for *in vitro* and *in vivo* functional studies. Furthermore, bioinformatic, immunohistochemical and NGS analysis of two UM's patients cohorts for the Chr 8q status identified NDUFB9 and LAPTM4B as potential functional drivers, whose expression enabled the development of a robust Multigene Score (MGS) highly potent in stratifying patients at high risk of disease-specific mortality.

Conclusion and Discussion. This work provides novel etiological insights into the potential role of BL and introduces a reliable prognostic tool (MGS) superior to single markers. The identification of NDUFB9 (involved in mitochondrial metabolism) and LAPTM4B (implicated in autophagy and drug resistance) as probable functional drivers of the metastatic phenotype suggests these genes are not merely passenger, but represent promising therapeutic targets, particularly within the context of UM's intrinsic resistance. Further functional validation of these genes is crucial. Future studies will focus on completing the creation of more complex *in vivo* mouse models (GNA11+BAP1) for metastatic evaluation. Furthermore, the application of spatial transcriptomics (Xenium) on metastatic samples treated with Tebentafusp will be essential to map therapeutic cellular interactions within the tumor microenvironment and spatially validate the 8q drivers at high resolution, guiding the next generation of treatment strategies.

CHAPTER I
INTRODUCTION

1. Anatomy of the Uvea

The human eye has a diameter of approximately 22–27mm anteroposterior and a 69–85mm circumference. Structurally, it is composed of three concentric layers. The outermost layer is composed of the cornea (transparent), the sclera (opaque), and the limbus (transitional zone). The middle layer is known as uvea or uveal tract and constitutes the eye's vascular component. It includes the iris, ciliary body, and choroid. The innermost layer is the retina, which functions as the neural apparatus responsible for phototransduction[1].

The uvea, the anatomical site in which originates uveal melanoma (UM), plays a critical role in ocular homeostasis. In fact, in addition to its vascular and nutritive functions, it contributes to intraocular physiology through: i) the regulation of aqueous humor dynamics, ii) the accommodation via the intrinsic ocular muscles, and iii) the modulation of lens shape for visual focus. In addition, the uveal pigment epithelium also minimizes intraocular light scatter, enhancing retinal image contrast.

The choroid, the most posterior and largest segment of the uvea, constitutes roughly two-thirds of the internal ocular surface. It contains abundant melanocytes, especially in its outer layer adjacent to the sclera, where they aid in pigmentation and help limit internal light reflection.

2. Uveal Melanoma – General Overview

UM accounts for approximately 5% of all melanomas and is the most common primary intraocular malignancy in adults, representing about 80% of all non-cutaneous melanomas [2].

Despite significant insights into its molecular underpinnings, UM remains largely incurable once metastasis occurs. Five-year survival rates for metastatic UM have shown little improvement in recent decades prior to the advent of novel immunotherapies, which have begun to shift this paradigm[3]. Compared to cutaneous melanoma (CM), UM presents marked differences in etiology, incidence, mutational profile, and clinical behavior, particularly its resistance to both targeted therapies and immune checkpoint inhibitors.

UM arises from melanocytes within the vascular uveal tract, namely the iris, ciliary body, and choroid, and is classified as anterior (iris) or posterior (ciliary body and choroid) based on its site of origin. Anterior UM, which represents up to 10% of cases, generally follows an indolent course and rarely metastasizes. Conversely, posterior UM is more aggressive and constitutes approximately 90% of cases[4] .

In a cohort exceeding 8,000 UM patients, 10-year metastasis rates were reported at 33% for ciliary body melanoma, 25% for choroidal melanoma, and 7% for iris melanoma. Mortality typically occurs within 1–3 years post-treatment and is often associated with mutations in the BAP1 and SF3B1 genes[2].

It is essential to distinguish UM from conjunctival melanoma, which originates in the mucosa of the conjunctiva. These tumors differ significantly in clinical, histopathological, and molecular characteristics: UM shares similarities with central nervous system melanocytic tumors, whereas conjunctival melanoma more closely resembles CM in its mutational landscape[5].

2.1. Epidemiology

While some studies report a balanced sex distribution for UM, others note a slight male predominance. Incidence rates vary significantly, ranging from <1 to >9 cases per million per year. In Europe, incidence increases along a northward gradient—from <2 cases per million annually in southern countries such as Spain and Italy to >8 cases in nations like Ireland, Norway, and Denmark.

Similarly elevated rates are observed in Australia (9.8/million/year) and New Zealand (9/million/year). In contrast, incidence is markedly lower in Asian populations—0.4/million/year in South Korea and 0.6/million/year in Japan—and in Africa, where it remains around 0.3/million/year[2].

2.2. Classification

Historically, UM was considered a uniformly characterized disease, despite early recognition of a correlation between tumor cell morphology and disease progression. An initial hypothesis proposed distinct carcinogenic development models for tumors with monosomy 3 and those with chromosome 6 alterations. However, subsequent research revealed that individual tumors often harbored cells exhibiting both monosomy 3 and chromosome 6 alterations simultaneously[6].

In 2004, Harbour's classification system refined this understanding, incorporating chromosome 3 status, gene expression profiles, and metastatic potential. This updated classification effectively stratified patients into two distinct risk classes:

- Class 1: Tumors characterized by disomy 3, which are associated with a low risk of metastasis.
- Class 2: Tumors characterized by monosomy 3, indicating a high metastatic potential.

Class 1 UM often shows amplifications of chromosome arms 6p and 8p associated with mutations in the SF3B1 and/or EIF1AX genes. Studies suggest that the gene expression patterns in these tumors resemble those found in normal uveal melanocytes and neural crest-derived cells[7]. UM cases within this class typically have a favorable prognosis.

Conversely, Class 2 UM frequently exhibits aneuploidy, including losses of chromosome arms 1p, 3, and 8p, and amplifications of 8q. Class 2 is strongly associated with inactivating mutations in the BAP1 gene on chromosome 3p21 and, as previously mentioned, are linked to an unfavorable prognosis[8]. The gene expression profile of Class 2 tumors is reminiscent of primitive cells with a stem-like phenotype[9].

A key factor distinguishing metastatic from non-metastatic UM is the former's tendency towards melanocytic de-differentiation and the acquisition of a stem-like phenotype. Histopathological risk factors for metastasis, such as epithelioid cell type and an inductive neoangiogenesis profile, likely reflect this de-differentiated state[9].

Early classification models hypothesized that different classes of UM tumors originated from distinct melanocyte precursors[10]. This hypothesis gained further support from observations of differential epigenetic mechanisms associated with chromosome 3 status and metastatic progression[11]. To identify genes distinguishing these tumor classes, supervised learning techniques were employed. An initial filtering process yielded 3,075 highly significant genes for UM that underwent further analysis. The median expression for these 3,075 genes was compared between Class 1 and Class 2 using a signal-to-noise algorithm. Genes were initially filtered for a signal-to-noise score of ≥ 0.25 and a significance level of $p \leq 0.01$ (1% permutation level). This filtering process resulted in 62 discriminant genes, including significant gene clusters on chromosome 3 ($P=0.002$) and 8q ($P=0.004$), which were, respectively, down-regulated and up-regulated in Class 2 tumors. However, when this gene set was further enriched using a threshold signal-to-noise score of ≥ 0.3 and a significance level of $p \leq 0.001$ (0.1% permutation level), most genes on chromosomes 3 and 8q were excluded[12].

Gene Ontology biological function annotations for the top genes included cell communication (13 genes), development (11 genes), cell growth (7 genes), cell motility (4 genes), and cell death (3 genes). Interestingly, a majority of the developmental genes (including KIT, ERBB3, EDNRB, SPP1, FZD6, TFAP2A, and SCDGF-B) have been implicated in the development of the neural crest, from which melanocytes originate[12]. Leveraging expression data from three distinct sample sets (snap-frozen, fine-needle aspiration biopsy [FNAB], and formalin-fixed paraffin-embedded [FFPE]), 22 candidate discriminant genes were mathematically classified

based on their weighted contribution or relevance to the overall gene expression signature, as well as their lack of redundancy with other discriminant genes. The rankings from each of the three training sets were then combined to generate a final list of 12 discriminant genes[13].

A more recent alternative model of progression posits that tumors originate from a single precursor melanocyte that retains both copies of Chromosome 3[14]. During the advanced stages of UM progression, a subset of cells loses one copy of chromosome 3, thereby acquiring metastatic capabilities. These observations are supported by analyses of certain tumors that contain regions with both monosomic and disomic cells for chromosome 3. Furthermore, some UMs have been identified in transitional states from Class 1 to Class 2, suggesting a potential progression from a pre-malignant nevus to a Class 1 melanoma and then to a Class 2 melanoma[15].

In a comprehensive multi-platform analysis of 80 uveal melanomas, Robertson et al. identified four clinically relevant molecular subtypes. Two of these subtypes were associated with monosomy of chromosome 3 (M3) and an unfavorable prognosis, while the other two exhibited disomy of chromosome 3 (D3) and a more favorable prognosis. The loss of BAP1 is associated with the occurrence of M3 and correlates with a global DNA methylation state that is distinct from D3 UMs. Importantly, uveal melanoma with monosomy of chromosome 3, despite its generally unfavorable prognosis, further subdivides into subsets with divergent genomic aberrations, transcriptional characteristics, and clinical outcomes[16].

2.3. Molecular Carcinogenesis, Driver Mutations and Pathways

Understanding how a tumor originates and progresses is rooted in three fundamental and interconnected concepts:

- Knudson's Two-Hit Hypothesis: This hypothesis posits that the transformation of a normal cell into a neoplastic cell requires at least two irreversible events, typically involving mutations in proto-oncogenes and tumor suppressor genes[17].
- Multistep Carcinogenesis Model: This model describes distinct morphological changes during tumor development, driven by specific molecular lesions[18].
- Hallmarks of Cancer: These define the distinct processes that characterize cancer evolution. These processes include: sustained proliferative signaling, evasion of growth suppressors, resistance to cell death, enabling replicative immortality, genome instability and mutation, induction of angiogenesis, deregulation of cellular energetics, avoiding immune destruction, tumor-promoting inflammation, and activation of invasion and metastasis[19].

Specifically, studies on UM have shown that nearly all UMs are characterized by mutations in GNAQ, GNA11, PLCB4, or CYSLTR2. However, these mutations alone are likely insufficient to initiate the neoplastic process. A "second hit" could involve an additional mutation or a concomitant systemic condition such as chronic inflammation or neoangiogenesis.

In recent decades, cytogenetic analyses have identified significant chromosomal aberrations in UM cells, particularly involving chromosomes 3, 6, and 8. The loss of chromosome 3 and mutations in BAP1 serve as key drivers in the process of invasion and metastatic progression. It is important to note that a partial deletion of chromosome 3 only occasionally results in a metastatic phenotype, suggesting the presence of additional pro-metastatic factors on chromosome 3[20].

While the precise molecular mechanisms underpinning the protective effect are not yet fully elucidated, amplification of the short arm of chromosome 6 (6p) has been shown to offer an apparent protective effect against metastatic UM. Chromosome 6p harbors genes crucial for eye development, and congenital deletions of this region lead to ocular malformations primarily affecting the anterior chamber. Furthermore, 6p also hosts the loci for HLA genes. Though HLA genes themselves are not directly associated with UM risk, they might play a role in UM progression by enabling target cells to evade NK cell-mediated lysis[5].

In contrast, amplifications of the long arm of chromosome 8 (8q) independently contribute to a metastatic phenotype. Although the oncogene MYC is located on 8q, its expression does not appear to be amplified in this context. Instead, the ASAP1 gene has been proposed as a mediator of the effects associated with 8q amplification. Of particular interest is the involvement of ARF6 in UM progression, as ASAP1 functions as a GTPase-activating protein for both ARF1 and ARF6[21].

The activation of mutations within the oncogenes GNAQ and GNA11 drives UM carcinogenesis. These mutations primarily occur at two hotspots within both genes, Q209 and, less frequently, R183, located in the Ras-like GTPase domain. GNAQ and GNA11 activate the G protein signaling cascade and the YAP/TAZ transcription factor complex, which is associated with organ size control. This consequently triggers downstream intracellular signaling pathways that are no longer inhibited by GTPases, thus representing potential therapeutic targets. These signaling pathways include the phospholipase C-beta (PLC-b)/protein kinase C (PKC) and Rac1/RhoA pathways, leading to the activation of ERK, p38, JNK, and YAP, and subsequent AP-1 and YAP/TEAD-mediated transcription.

Among the molecules involved, the small GTPase ARF6 is a particularly intriguing clinical candidate. It acts as a proximal node, or effector, of oncogenic Gaq signaling, inducing all these pathways, as well as beta-catenin signaling. ARF6 regulates the trafficking of GNAQ and beta-catenin from the plasma membrane to cytoplasmic vesicles and the nucleus, respectively. However, these G proteins have proven elusive for direct therapeutic targeting, leading most efforts to individually target each divergent pathway, thereby blocking only a subset of the critical pathways. The oncogene GNAQ induces its multiple signaling pathways through a single node, the small GTPase ARF6. Blocking ARF6 with an inhibitor reduces UM cell proliferation and tumorigenesis in a mouse model, confirming the functional relevance of this pathway and offering a therapeutic strategy for G-alpha-mediated diseases[21].

Less frequently, alterations in the CYSLTR2 gene or the phospholipase C beta 4 (PLCB4) gene has been observed as initiating mutations in UM. However, approximately one-third of UM also exhibit mutations in the BAP1 gene, which is responsible for the metastatic evolution of the disease[4]. BAP1 is a tumor suppressor gene whose function is typically depleted through mutation of the first allele and loss of the second[8]. Alternatively to BAP1, an unfavorable prognosis can also be indicated by hotspot mutations in the SF3B1 and SRSF2 genes[22]. These mutations likely influence the splicing of various genes, thereby creating oncogenic splicing variants. BAP1 mutations are associated with a high metastatic risk, whereas SF3B1 mutations are linked to an intermediate metastatic risk[19]. Cases without mutations in either of these two genes generally have a low risk of metastasis[19]. Additionally, frequent gain-of-function mutations are found in the 5' coding sequence of the EIF1AX gene and are associated with a low metastatic risk.

Therefore, UMs with a low metastatic risk typically present with a single recurrent mutation in GNAQ, GNA11, CYSLTR2, or PLCB4, sometimes with an additional mutation in EIF1AX. High-risk cases, conversely, harbor two recurrent mutations: one from the initial four and one from either BAP1 or SF3B1. The combination of a hotspot mutation in a G protein alpha subunit and a protein-truncating mutation in a tumor suppressor gene is thus considered sufficient to form a highly aggressive metastatic tumor that is resistant to conventional chemotherapy, to targeted therapy, and to the use of immune checkpoint blockers, often leading to patient mortality within one year of metastasis diagnosis[2].

2.3.1. GNAQ and GNA11

GNAQ and GNA11 are considered the primary drivers of UM carcinogenesis, with mutations occurring in over 80% of cases[23]. These mutations are typically mutually exclusive, affecting GNAQ in approximately 45% of patients and GNA11 in 42%.

GNAQ/GNA11 signaling occurs through the activation of YAP, a protein that controls tissue growth and cell fate by regulating cell proliferation and apoptosis. Inhibiting YAP with verteporfin has shown promise in blocking tumor growth[4]. Furthermore, functionalized gold nanoparticles targeting GNAQ mRNA have been developed. These nanoparticles can inhibit GNAQ activity, leading to reduced downstream signaling and decreased cell viability in UM cells[19]. GNAQ/GNA11 mutations may also impact the BET protein family. These proteins are involved in regulating key cellular division processes such as DNA replication, chromatin remodeling, and mRNA transcription. BET inhibitors, such as JQ1, can significantly inhibit growth in UM cells harboring GNAQ/GNA11 mutations.

The functional small G protein ARF6 acts immediately downstream of Gα-q and is responsible for activating several signaling cascades[2], including the mitogen-activated protein kinase (MAPK), β-catenin, RhoA–Rac, and Yes-associated protein (YAP) pathways[21]. Although activating mutations in the Gα-q pathway are found in almost all UMs, the individual contributions of these pathways to oncogenesis remain unclear. Multiple studies strongly support a prominent role for YAP activation in UM[24,25], where Gα-q triggers focal adhesion kinase (FAK) via the TRIO–RhoA pathway, with FAK subsequently activating YAP through Mps one binder 1 (MOB1)[26]. Interfering with this cascade is currently considered a potential treatment option for metastatic disease. While Gα-q mutations activate the MAPK pathway[27,28], the observed clinical inefficacy of MAPK inhibitors in UM patients suggests that this pathway holds only an accessory role in tumorigenesis. Furthermore, drugs designed to directly inhibit Gα-q, such as FR900359 and YM-254890, do not differentiate between the wild-type and mutated forms of G alpha-q, making them toxic and unsuitable for therapeutic use[29,30].

GNAQ is the most frequently mutated gene in this disease. Most melanoma-associated mutations in GNAQ are found at codon 209 within exon 5, a region within the catalytic (GTPase) domain of GNAQ. A mutation at this site inactivates the GTPase domain, resulting in a constitutively active GNAQ protein capable of promoting neoplastic transformation of melanocytes. GNAQ mutations are observed in tumors across all stages of malignant progression and are independent of chromosome 3 status or gene expression profiling (GEP), suggesting that GNAQ mutation is an early event in UM development[31]. GNAQ has been shown to influence multiple cellular signaling pathways through a single node known as ARF6. Blocking ARF6 can reduce the growth of GNAQ/11-dependent UM cells, suggesting another potential therapeutic strategy[19].

GNA11 mutated uveal melanoma, instead, has a worse prognosis and it is associated with high risk cytogenetic, mutational and molecular tumor characteristics that might be determined at

least in part by differential DNA-methylation. In fact, GNA11 mutation was associated with: i) an increased frequency of loss of BRCA1-associated protein 1 (BAP1), ii) monosomy of chromosome 3, iii) amplification of chr8q, iv) the combination of the latter two, and inversely with v) chr6p gain[5]. The analysis also showed a shorter disease-specific survival of GNA11-mutated cases as compared to those carrying a GNAQ mutation. GNAQ and GNA11 encoded G-proteins have different protein interaction partners. Specifically, the Tet Methylcytosine Dioxygenase 2 (TET2), a protein that is involved in DNA demethylation, physically interacts with the GNAQ protein but not with GNA11, as confirmed by immunoprecipitation analyses. High-risk UM cases show a clearly different DNA-methylation pattern, suggesting that a different regulation of DNA methylation by the two G-proteins might convey a different risk of progression[19].

2.3.2. BAP1

The BAP1 gene is inactivated in UM following the deletion of one allele and a mutation on the second, leading to the complete loss of the gene[32]. The localization of BAP1 to 3p21 partially explains the association between chromosome 3 loss and the development of metastatic UM. This gene encodes an enzyme that removes single ubiquitin components from various substrates, including histone H2A, HCF-1, and BRCA. Despite its ubiquitin-related function, BAP1 does not appear to be involved in the proteasome-dependent degradation mechanism. Instead, it is implicated in regulating critical cellular functions such as gene expression, cell cycle checkpoint control, maintenance of cellular differentiation, and DNA repair following double-strand breaks.

2.3.3. SF3B1

Splicing Factor 3B subunit 1 (SF3B1) is a crucial protein in the spliceosome, anchoring the U2 snRNP to pre-mRNA to facilitate the removal of introns. Its structure features HEAT repeats essential for protein interactions, and it is also involved in the minor U12-type spliceosome. Mutations in the SF3B1 gene are frequently found in various cancers, such as myelodysplastic syndromes, where they lead to aberrant splicing and altered gene expression. These mutations serve as important diagnostic markers and potential therapeutic targets.

In UM, mutations in the SF3B1 gene are characterized by four key features: primarily point mutations affecting Arginine-625, monoallelic mutations, mutual exclusivity with BAP1 mutations, and association with Class 1 tumors, which carry a positive prognosis even if within Class 1, SF3B1 mutation confers, however, a metastatic risk.

2.3.4. EIF1AX

Eukaryotic translation initiation factor 1A (eIF1A) is a core component of the 43S pre-initiation complex (PIC), a key step in protein synthesis. Encoded by the EIF1AX gene, its primary function is to recruit the 40S ribosomal subunit to the messenger RNA (mRNA) 5' cap. Functionally analogous to bacterial initiation factor 1 (IF1), eIF1A binds near the ribosomal A-site. Mutations in the EIF1AX gene have been linked to diseases like thyroid cancers and uveal melanoma. Mutations in the EIF1AX gene, located on chromosome X, are associated with Class 1 UMs and a favorable prognosis. Intriguingly, EIF1AX-mutated UMs do not develop metastatogenic mutations, and EIF1AX does not contribute to the formation of metastases. While these mutations are selected during tumorigenesis, suggesting they confer a growth advantage, they do not truncate the protein and occur in heterozygosity, characteristics typically associated with dominantly acting oncogenes[33].

2.3.5. TERT

The identification of a UV-induced cytidine-to-thymidine driver mutation in the TERT gene promoter in cutaneous melanoma prompted researchers to investigate the occurrence of these mutations in UM. A study of 50 UM cases identified a single instance reporting this mutation alongside GNA11 and EIF1AX mutations, which are typical of UM and absent in CM and conjunctival melanoma. Increased expression of the catalytic subunit of TERT promotes the immortalization of somatic cells, a critical stage in neoplastic transformation. However, data regarding the prognostic effects of mutated TERT in UM are not yet available[34].

2.4. Malignant Transformation

Highly recurrent mutations in UM strongly support the idea that subsequent malignant transformation in choroidal melanocytes is driven by the combination of two main events: an alteration in the Gαq pathway and mutations in either BAP1, SF3B1 or EIF1AX. A mutation in a GNA family gene is believed to be the initial event, as these mutations are found in benign blue nevi and uveal nevi. However, the exact mechanism of progression from a benign nevus to UM still needs to be fully elucidated[35]. Furthermore, more recent genomic analyses support an alternative model, known as punctuated equilibrium or punctuated evolution, where a burst of oncogenic events, including chromosome copy number changes and driver mutations, appears to occur almost simultaneously rather than through a gradual accumulation[36]. This model suggests that the key genetic alterations for malignant transformation can emerge rapidly in a single catastrophic event, leading to the abrupt onset and progression of the disease.

2.5. Metastasis

The liver is the most common site for UM metastasis, although secondary tumors can also arise in other organs such as the lungs, lymph nodes, bones, skin, and brain. The complex metastatic process of UM can be conceptualized in three phases: the primary tumor, the hematopoietic tissue, and the distant metastatic site, predominantly the liver[37].

Invasion of blood vessels by UM cells occurs at the primary tumor site. Tumor cells then enter the systemic circulation, traversing the right side of the heart, the lungs, the left side of the heart, and the aorta before being introduced by systemic circulation into hematopoietic tissues, including the bone marrow and spleen. Direct evidence indicates that the expression of cMET by tumor cells plays a role in their affinity for the liver. Hepatocyte growth factor (HGF), the ligand for cMET, is produced by hepatic stellate cells; the involvement of the cMET-HGF axis has been demonstrated in murine models of metastatic UM. Further explaining the liver's role as the primary metastatic target, primary UM cells have also been observed to express CXCR4. Its ligand, CXCL12, is produced by hepatic sinusoidal endothelial cells and hepatic stellate cells. In mice, blocking either the CXCR4-CXCL12 or the cMET-HGF axis inhibits the development of metastases[35].

Within the liver, direct evidence from both human samples and murine models indicates that individual UM cells can infiltrate the hepatic parenchyma or exhibit periportal localization, eventually demonstrating angiogenesis, which is essential for tumor growth in this metastatic site[38].

Metastatic UM in the liver can be categorized into two types based on their localization and behavior: infiltrative and nodular[38]. When present within the sinusoidal spaces, UM exhibits an infiltrative growth pattern. Conversely, if localized in the periportal areas, it displays a nodular growth pattern. Both growth patterns can be present simultaneously within the same liver, and in some cases, the nodular pattern may give rise to the infiltrative pattern. The infiltrative growth pattern of UM relies on the creation of pseudo-sinusoidal spaces by hepatic stellate cells, whereas the nodular growth pattern depends on angiogenesis in the periportal areas.

Metastatic growth in both the infiltrative and nodular patterns is primarily induced by hypoxia. In the infiltrative model, hypoxia promotes collagen production by hepatic stellate (Ito) cells. Conversely, in the nodular pattern, it drives the production of vascular endothelial growth factor (VEGF) by the melanoma cells themselves. Typically, VEGF activity is counterbalanced by the production of pigment epithelium-derived factor (PEDF) from hepatic stellate cells. However, melanoma cells counteract this by producing platelet-derived growth factor and transforming

growth factor-β, which actively inhibit PEDF production. This disruption of the PEDF-VEGF equilibrium, shifting the balance in favor of VEGF, fosters metastatic melanoma growth[39].

It is also important to note that a larger primary melanoma correlates with a higher generation of cells exhibiting pro-metastatic mutations, notably those with BAP1 and SF3B1 alterations. The loss of BAP1 expression can serve as an indicator to differentiate tumors with an overall low or high risk of metastasis[32].

Furthermore, additional recurrent copy number alterations have been associated with tumor progression, including losses of 1p, 6q, and 8p, and gains of 1q, 6p, and 8q, as well as isodisomy 3. Finally, mutations in chromatin remodeling factors, such as PBRM1 and EZH2, appear to occur as late events in tumor evolution. These findings support a sequence of events in UM progression that begins with BAP1 and subsequently involves PBRM1, EZH2, and likely other genes in later stages.

2.5.1. Role of Chromosome 8q and ASAP1

Gain of the long arm of Chromosome 8 (8q) is a recurrent chromosomal aberration observed in UM, strongly correlating with increased metastatic risk and poorer patient prognosis[40]. While MYC, a well-known oncogene, resides on 8q, detailed genomic analyses have consistently shown that its amplification is generally not the primary driver or a highly recurrent event within this gain in UM[41] . Instead, the 8q gain in UM encompasses a broader region containing multiple genes whose increased expression collectively contributes to tumor progression and metastatic dissemination. Among these, ASAP1 (ArfGAP with SH3 domain, Ankyrin repeat and PH domain 1) has emerged as a key candidate driver gene. ASAP1 is an actin-binding protein involved in membrane protrusion, cell migration, and invasion, processes critical for metastasis. Its elevated expression, resulting from 8q gain, serves as a robust prognostic marker for metastatic progression in UM and is actively being explored for its functional contribution to the aggressive phenotype of these tumors[42–44].

2.6. Pathophysiology

It is plausible that genetic variants associated with an elevated risk of developing UM, including variants in pigmentation genes, largely explain its epidemiological trends. The roles of different melanin types in early malignant transformation are currently under investigation. Genetic variants on chromosome 15q13.1, located near the HERC2 and OCA2 gene loci (on 15q12) involved in determining eye color, have been associated with UM risk. Similarly, mutations in

the G proteins GNAQ and GNA11, which are involved in skin color determination in mice, have also been linked to UM risk[2].

In contrast to epidemiological data, molecular data on UM onset can clearly exclude the mutational spectrum typically associated with UV radiation. Whole-exome sequencing of UM, in fact, demonstrates a relatively low mutational burden and no enrichment in dipyrimidine C>T transitions, which are characteristic of UV exposure[22]. UV-induced mutations in the promoter of the human telomerase reverse transcriptase (TERT) gene occur in approximately 70% of CM cases but are rare in UM. This suggests that if light plays a role in UM carcinogenesis, its mechanism of action is distinctly different from that observed in CM[5].

Considering the risk factors, there is a clear association between light eye color and a higher predisposition to developing UM. Blue or grey irises are associated with pheomelanin (a yellow-brown pigment), while brown irises are associated with eumelanin (a black-brown pigment). More specifically, pale skin, red hair, freckles, and an inability to tan are correlated with inactivating variants in the gene encoding the melanocortin-1 receptor (MC1R), which results in relatively high levels of pheomelanin. Furthermore, in melanocytes lacking functional OCA2 (necessary for normal melanin production), 5,6-dihydroxyindole-2-carboxylic acid (DHICA), a precursor in eumelanin synthesis, is not correctly transported into the cell and is retained in compartments between the endoplasmic reticulum (ER) and Golgi apparatus. This accumulation leads to defective eumelanin synthesis but does not affect pheomelanin synthesis. DHICA accumulation can cause single-strand breaks in plasmid DNA (both with and without UV exposure). Consequently, a low eumelanin-to-pheomelanin ratio and a high concentration of reactive oxygen species (ROS) may represent a risk factor for the acquisition of somatic mutations in ocular melanocytes[2].

2.7. Etiology Known to Date

The etiology of uveal melanoma (UM) remains largely unclear, despite the well-established role of ultraviolet (UV) radiation as a primary risk factor for cutaneous melanoma[45,46] (CM). This has prompted considerable interest in investigating the potential involvement of UV exposure in UM development.

To this end, a recent study applied regularized dictionary learning[19] to 139 UM cases, identifying two novel mutational signatures and their associated exposures. These new signatures, while correlating with those derived from Alexandrov's algorithm (which is commonly used for CM signatures[45,46]), provided greater informativeness for UM, attributed to an expanded consensus from NCG to NCG and CCN. Notably, specific GNAQ and GNA11 mutations (A>T or A>C),

although linked to light exposure and iris color[47], did not align with the UM-specific mutational signatures[19] identified in the study.

This finding parallels the observation that BRAF mutations in CM do not align with the UV mutation signature, providing compelling evidence for distinct etiologies for the two tumors: UV light for CM and an unknown etiological factor for UM. This conclusion is consistent with the fact that the vitreous body and lens of the eye absorb the majority of incoming UV radiation[48]. Nevertheless, it is possible that age-dependent alterations in the vitreous body could potentially modify its absorption capacity, which may represent a variable factor.

Therefore, the etiological effect of UV radiation on UM development is considerably less significant than for CM. It is likely too weak to overcome confounding variables such as the co-distribution of lightly pigmented skin and irises with an individual's latitude of birth, the co-occurrence of UV radiation with longer-wavelength light, and the protective vitamin D-mediated effects of sun exposure. A meta-analysis of 133 reports investigating UV-associated risk factors for UM found a significant correlation only among individuals engaged in welding activities, with no significant association observed for recreational or professional outdoor activities or the subject's latitude of birth[49].

Having largely discounted UV radiation as a significant etiological agent, current research is evaluating the potential role of the more energetic part of the visible light spectrum, specifically blue light, in UM etiogenesis. Supporting this hypothesis, the development of ocular tumors has been described in mice exposed to blue light, and such stimulation significantly increased the proliferative capacity of human UM cells in culture compared to shielded controls[50].

2.8. Risk Factors

While the exact causes of UM are not fully understood, age is consistently identified as a significant, albeit non-modifiable, risk factor, with most diagnoses occurring between 50 and 70 years[2]. Beyond age, several other factors are associated with an increased likelihood of developing UM, including fair skin, light-colored irides (particularly blue or gray), and a predisposition to sunburn. Conversely, blond or red hair is not considered a significant risk factor. Individuals with UM are more likely to have dysplastic nevi, a history of cutaneous melanoma, and a positive familial history. Five- and fifteen-year disease-specific mortality rates are approximately 30% and 45%, respectively[51].

Risk factors may be broadly categorized into genetic and environmental domains.

2.8.1. Genetic

Multiple genetic loci are implicated in UM susceptibility and are categorized based on associated risk levels. Among low-risk loci, a study analyzing single nucleotide variants (SNVs)—previously linked to cutaneous melanoma—identified a significant association between UM and SNVs in HERC2, OCA2, and IRF4, all genes involved in pigmentation. These findings corroborate the correlation between fair pigmentation phenotypes and increased UM risk. A subsequent genome-wide association study (GWAS) validated these findings[52], and identified a novel candidate locus on chromosome 5p15.33, encompassing telomerase reverse transcriptase (TERT) and cleft-lip and palate transmembrane protein 1-like (CLPTM1L). Risk variants in this region are associated with increased CLPTM1L expression, which may facilitate RAS-dependent transformation and tumorigenesis.

In terms of high-risk loci, The Cancer Genome Atlas (TCGA) has reported rare germline mutations in seven oncogenes, with BAP1 demonstrating the most compelling link to hereditary UM predisposition. Though BAP1 mutations occur in only 1–2% of the general UM population, their prevalence rises to 18–22% in familial UM (FUM) cases. FUM, defined as UM in two or more biologically related individuals, constitutes approximately 0.6% of all UM cases and typically presents unilaterally.

Additional germline mutations in MLH1, PALB2, and SMARCE1 have been identified in 9% of FUM cases. Broader sequencing studies have uncovered sporadic associations with BRCA1, BRCA2, FLCN, MSH6, and CHEK2. However, the strength of association with these genes remains moderate to limited due to the rarity and heterogeneity of UM[53].

Approximately 12% of UM patients report a strong familial and/or personal history of malignancy. Secondary primary cancers—including cutaneous melanoma, gastrointestinal and genitourinary cancers, breast cancer, non-Hodgkin lymphoma, and multiple myeloma—are common in this cohort. UM may also occur within the BAP1 tumor predisposition syndrome, which includes melanocytic skin tumors, mesothelioma, and renal cell carcinoma, with other associated malignancies including meningioma, basal cell carcinoma, and cholangiocarcinoma[2].

2.8.2. Environmental

Environmental exposures, particularly to chemicals, are implicated in UM pathogenesis. Agents such as asbestos, antifreeze, formaldehyde, and pesticides have been linked to UM development. These exposures may be especially relevant in individuals with BAP1 germline mutations. In animal models, BAP1-mutant mice exhibit increased susceptibility to asbestos-induced

malignancies, likely due to enhanced inflammatory responses. Similarly, asbestos exposure has been shown to potentiate mesothelioma in BAP1-mutated individuals[5].

Epidemiological studies have also highlighted welding as a significant environmental risk factor. The risk profile extends beyond ultraviolet radiation to include visible and infrared light, often in combination with chemical exposures. More recently, emerging evidence, particularly from studies in adolescent and young adult populations, suggests that factors like passive smoking, prior ocular trauma, and even exposure to blue light may also contribute to UM risk[54]. While these associations require further confirmation, they highlight a broadening understanding of environmental influences on UM development.

2.9. Immunity and Inflammation

The eye is considered an immune-privileged organ, meaning it is physiologically protected from inflammatory responses and non-specific immune activation that could potentially impair visual function. This immune privilege is maintained through a variety of mechanisms, including anatomical barriers such as the blood-retinal barrier and the absence of afferent lymphatic drainage. Additionally, the aqueous humor contains the pleiotropic cytokine macrophage migration inhibitory factor (MIF), which suppresses natural killer (NK) cell activity, thereby reinforcing the immunosuppressive environment. Furthermore, epithelial cells of the iris and ciliary body can inhibit T cell activation and proliferation through direct cell-to-cell contact.

Although this immune privilege serves to preserve ocular integrity, it is hypothesized that such an immunosuppressive microenvironment may provide a permissive niche for the development and progression of UM[55]. In this context, UM cells are able to evade both innate and adaptive immune surveillance, allowing for unchecked tumor growth until the tumor breaches the blood-retinal barrier and disseminates systemically. NK cells, along with other innate immune components within the ocular compartment, are capable of preventing metastatic spread by eliminating circulating tumor cells before they reach the liver, which is the predominant site of UM metastases. However, once tumor cells exit the eye, they acquire enhanced metastatic potential by expressing pro-oncogenic and immunoregulatory molecules such as indoleamine 2,3-dioxygenase 1 (IDO-1), MIF, and programmed death-ligand 1 (PD-L1)[5].

Chronic inflammation is also a key factor contributing to tumorigenesis, particularly in the early phases of oncogenic transformation[56]. Recruitment of monocytes from the peripheral circulation and their subsequent differentiation into tumor-associated macrophages (TAMs) is a critical event in the establishment of the tumor microenvironment, which exhibits several hallmarks of chronic inflammation. A variety of chemokines, cytokines, and complement cascade proteins

facilitate monocyte recruitment and TAM differentiation within the tumor site. Once established, TAMs engage in extensive crosstalk with tumor cells, endothelial cells, fibroblasts, and various mesenchymal and lymphoid populations. These interactions promote tumor progression through enhanced cancer cell proliferation and survival, angiogenesis, and suppression of anti-tumor immune responses.

Monocytes and macrophages display high functional plasticity and may undergo divergent polarization in response to different microenvironmental cues. In UM, high TAM density is associated with epithelioid cell morphology, increased pigmentation, and elevated microvascular density—features that correlate with more aggressive clinical behaviour. Notably, the presence of numerous TAMs in primary tumors has been linked to higher UM-specific 10-year mortality rates[57].

Interestingly, a subset of patients exhibited rapid UM regression accompanied by intraocular inflammation and uveitis following I-125 brachytherapy[58]. These patients predominantly harbored class 1 tumors, as determined by gene expression profiling, which are considered low-risk. Class 1 tumors display higher expression of melanocyte differentiation antigens that may be more readily recognized by the immune system, in contrast to class 2 tumors, which are more poorly immunogenic. This suggests that antigen release induced by brachytherapy may unmask class 1 tumors to immune recognition and facilitate immune-mediated tumor clearance.

2.10. Diagnosis

Symptoms that prompt individuals to investigate potential ocular issues are generally non-specific[53]. UM can be entirely asymptomatic until it extensively invades the central ocular globe, leading to a decrease in vision. Alternatively, it may present with early warning signs such as flashes of light and blurred vision. When preliminary medical examinations, conducted by an optometrist, ophthalmologist, or family physician, reveal alterations in normal ocular anatomy, patients are typically referred to an ocular oncologist.

The ophthalmologist performs a comprehensive eye examination, including the fundus. A UM diagnosis is established by recognizing its classic characteristics, such as pigmentation level, shape, dimensions, thickness, reflectivity, and position. Diagnosis is achievable through biomicroscopy and indirect ophthalmoscopy, combined with results from a wide array of diagnostic tests. Various imaging modalities are crucial for differentiating between benign nevi and malignant melanoma, as well as between melanoma and other tumors. Due to the disease's rarity, population-wide screening for UM is not conducted, and since risk factors are primarily genetic, specific preventive measures cannot be advised[2].

Biomicroscopy with a narrow light beam and indirect ophthalmoscopy are primary imaging modalities, though gonioscopy and transillumination can also be employed[1]. A general ophthalmologist may utilize fluorescein angiography in the differential diagnosis of a fundus lesion and then refer a patient with a suspicious lesion to a specialized ocular oncology center. An ophthalmic oncologist will further employ ultrasonography and anterior segment ultrasound, along with sophisticated techniques such as optical coherence tomography (OCT). Regardless of the technique used, it's essential to consider its limitations, as many of these methods rely on the visual identification of tumor characteristics.

Biopsy is rarely performed to diagnose UM. Nevertheless, it remains a valuable method for confirming a UM diagnosis when clinical examination and imaging are inconclusive. The most commonly employed technique is fine-needle aspiration biopsy (FNAB), where a needle is passed through the sclera and vitreous body under indirect ophthalmoscopy guidance. Other methods involve devices like the Essen forceps, which "bite" a sample from the tumor, or a vitreous cutter. Biopsy is considered a safe procedure when performed by an experienced ocular surgeon.

2.11. Prognosis and Treatment

Several factors influence the prognosis of UM, which can be broadly divided into histopathological parameters, cytogenetic characteristics, and mutational status. Histopathological parameters include patient age and general condition, the size and location of the primary tumor, extraocular invasion, epithelioid or spindle cell morphology, and the basal tumor diameter. Cytogenetic characteristics encompass monosomy of chromosome 3 (Chr.3) and polysomy of chromosome 8q (Chr.8q). Specific prognostic markers identifying the mutational status are represented by mutations in BAP1, GNAQ/GNA11, EIF1AX, and SF3B1, as discussed in the preceding section of this chapter[2].

The metastatic outcome of the disease is strongly correlated with the size of the primary tumor. In a study of 8,033 patients, each millimeter increase in thickness raised the 10-year metastatic risk by 5%. Furthermore, vasculogenic mimicry (VM) patterns have been identified in UM, where tumor cells generate fluid-conducting structures, including branching arches, closed vascular loops, and vascular networks, all associated with an increased risk of metastasis. While the probability of a patient developing metastases can be accurately predicted, the primary ocular treatment of the eye with UM does not prevent the development of these metastases. This suggests that tumor cells must have disseminated prior to treatment. Currently, despite

advancements in targeted therapies, effective adjuvant therapy for preventing metastatic growth after primary tumor treatment remains an unmet clinical need[2].

2.11.1. Radiotherapy: Brachytherapy and Teletherapy

Radiotherapy remains the most common globe-preserving treatment for UM. There are two primary forms: brachytherapy (plaque radiotherapy) and teletherapy (charged particle radiotherapy or stereotactic radiotherapy)[59].

Plaque radiotherapy, a form of brachytherapy, employs various radioisotopes. This treatment involves suturing a curved, radioactive plaque directly onto the sclera, precisely over the tumor, to deliver trans-scleral radiation to the UM. The total treatment duration is determined by the plaque's radioactive activity. To minimize radiation-induced morbidity, intravitreal steroids or anti-angiogenic agents are often administered. When performed by experienced specialists and with careful patient selection, plaque radiotherapy can achieve tumor control and eye preservation in up to 98% of cases, with globe salvage in approximately 95% of patients, often with good visual acuity preservation. This treatment is applicable to both small and large UMs.

With stereotactic radiotherapy, multiple photon beams are focused on the tumor from various directions, either simultaneously or sequentially. This approach delivers a high radiation dose to the tumor while minimizing collateral damage to surrounding healthy tissues. For instance, there is growing interest in image-guided and robot-assisted radiosurgery, such as CyberKnife[2].

2.11.2 Surgery

Local Resection

Local resection of UM involves the surgical removal of the tumor either en bloc through a scleral window (exoresection) or in a fragmented manner using a vitreous cutter passed through the retina (endoresection). These methods are typically reserved for circumscribed tumors considered unsuitable for radiotherapy due to their large size or juxta-papillary location. In addition to tumor removal, resection provides tissue for diagnostic confirmation and prognostication, while aiming to preserve the globe and vision[60].

Potential complications include retinal detachment, hemorrhage, and tumor recurrence. Concerns about tumor dissemination have led some centers to perform endoresection only after neoadjuvant radiotherapy. However, rates of local tumor recurrence and metastasis following endoresection alone are comparable to those reported after other forms of therapy.

Enucleation

Enucleation is indicated for advanced UMs (diameter >20 mm, thickness >12 mm), UMs with optic nerve involvement (which are rare), orbital invasion, and/or eyes with secondary glaucoma. An orbital implant replaces the volume of the globe, and some implants can be attached to the extraocular muscles to maintain prosthetic motility[2].

Exenteration

Orbital exenteration, which involves the removal of the globe, adjacent muscles, nerves, and adipose tissue, is indicated for cases with extensive orbital tumor growth. When possible, a technique that spares the eyelids is employed to facilitate rapid rehabilitation[2].

2.11.3 Chemotherapy

Chemotherapy is primarily employed in cases of UM that have developed hepatic or generalized metastases. For hepatic oligometastases, surgical resection or ablation may improve outcomes in selected patients. Given that hepatic metastases are preferentially supplied by branches of the hepatic artery, regional approaches have been investigated. These include intra-arterial chemotherapy, isolated hepatic perfusion, and chemoembolization.

Systemic chemotherapy regimens for UM have largely been adapted from those used for cutaneous melanoma. These include agents such as dacarbazine, temozolomide, cisplatin, bendamustine, treosulfan, fotemustine-based regimens, and others. However, these systemic treatments have generally not yielded significant clinical improvement in UM patients[61].

2.11.4. Tebentafusp

Tebentafusp-tebn (Kimmtrak®) represents a significant advancement in the systemic treatment of metastatic UM (mUM). It is a novel bispecific fusion protein that combines a soluble T-cell receptor (TCR) designed to recognize an HLA-A*02:01-restricted gp100 peptide (a melanocyte differentiation antigen) with an anti-CD3 immune-effector function. This unique mechanism of action enables Tebentafusp to redirect and activate T-cells to target and eliminate gp100-positive tumor cells. Approved by the FDA in January 2022, Tebentafusp is specifically indicated for HLA-A*02:01-positive adult patients with unresectable or metastatic UM. Its approval was based on the results of the pivotal Phase 3 IMCgp100-202 trial, which demonstrated a statistically significant improvement in overall survival (OS) compared to investigator's choice of therapy (which included pembrolizumab, ipilimumab, or dacarbazine). This makes Tebentafusp the first and only therapy to date to show an OS benefit in mUM, marking a critical milestone in the management of this aggressive disease[62].

It was in fact demonstrated that in uveal melanoma (UM), the response to immune checkpoint inhibitors (ICIs) is markedly different from that of cutaneous melanoma (CM)[63]. UM liver metastases retain the genomic and immune characteristics of the primary tumor, showing low expression of ICI markers and a high frequency of *GNA11*, *GNAQ*, *BAP1*, and *SF3B* mutations. Compared to metastatic CM, UM liver metastases have lower infiltration of various immune cells, but a higher proportion of M2 macrophages. A longer median overall survival (OS) has been observed in metastatic UM patients with higher expression of *LAG3*, *HLA class I*, or *HLA class II*, which may represent a small subset of "immune hot" tumors. Furthermore, the expression patterns of G2M checkpoint and E2F targets suggest a possible contribution to immunotherapy response[63].

Analyzing UMs biopsies taken prior to treatment, early on-treatment, and at progression (NCT02570308), using RNA sequencing (RNA-seq) and immunohistochemistry (IHC), it was shown that expression of interferon-related genes in the tumor prior to treatment is associated with improved overall survival and tumor reduction on tebentafusp, that T cell recruitment occurs even in tumors with a low baseline level of T cell infiltration, and that durability of changes induced in the tumor microenvironment is key for survival duration[64].

Further investigation into Tebentafusp's mechanisms involved sequential skin biopsies, which revealed that 81.8% of patients experienced acute cutaneous adverse events, notably associated with improved survival. Detailed analyses identified robust infiltration and activation of both CD4+ and CD8+ T cells, alongside significant changes in melanocyte gene expression[65]. These findings offer crucial pharmacodynamic insights into Tebentafusp's on-target effects, enhancing the understanding of treatment-related toxicity and guiding future strategies for therapeutic optimization[65].

2.11.5 Proton Beam Therapy

Proton Beam Therapy (PBT) is a highly precise external beam radiotherapy modality that utilizes protons to deliver ionizing radiation accurately within the tumor mass[66]. The typical protocol for Uveal Melanoma (UM) involves administering PBT in four consecutive fractions, delivering a total dose of approximately 60 Gy[67,68]. The primary clinical advantage of PBT lies in its ability to precisely target the lesion via maximal energy deposition at the Bragg peak (Figure 1A). This dosimetric feature is characterized by low radiation doses at both the entrance and exit, which significantly minimizes exposure and the risk of damage to surrounding normal tissues and structures proximal to the treated tumor[69,70]. The capacity to modulate energy deposition to a specifically defined, narrow depth allows for the selective targeting of the tumor

volume, thereby mitigating radiotherapy-induced side effects[69,70]. Furthermore, PBT is applicable to UM regardless of its location or thickness within the eye, offering a clear benefit over brachytherapy, which is constrained by proximity to critical structures such as the optic nerve[71–73]. However, energy deposition via the Bragg peak is concurrently associated with an increase in Linear Energy Transfer (LET). This increase occurs as protons slow down and lose energy while traversing the tissue. The elevated LET intensifies the frequency of ionization events along the radiation track, which, in the context of cellular DNA (Figure 1B), translates into greater extent and complexity of damage[69,70]. This Complex DNA Damage (CDD) is considerably more challenging for cells to repair than isolated damage, contributing to a higher rate of cell death and, consequently, a greater Relative Biological Effectiveness (RBE)[74]. For treating larger tumors, combining beams with different initial energies is employed to create a Spread-Out Bragg Peak (SOBP).

3. Experimental models useful for understanding UV: an update

3.1. In vitro models

In 1987, Dorothy C. Bennet and her research group at the Department of Anatomy, St. George's Hospital Medical School, London, successfully established a non-tumorigenic mouse melanocyte cell line, syngeneic with B16 melanoma cells, that exhibited a requirement for a tumor promoter for growth: the Melan-A cell line[75].

The designation "Melan-a" was chosen to denote the a/a (non-agouti or black) genotype. These cells are derived from embryonic melanoblasts of C57BL mice. They faithfully retain all tested characteristics of normal melanocytes, with the exceptions of senescence and a proliferative response to cholera toxin in the presence of TPA (12-o-tetradecanoylphorbol-13-acetate), a tumor promoter also referred to as phorbol myristate acetate. Being immortal diploid cells, syngeneic with B16 melanoma, and non-carcinogenic in syngeneic and nude mice, Melan-a cells represent an excellent model system for both cellular and molecular investigations into melanoma carcinogenesis.

Melan-a cells produce the black pigment melanin, which is macroscopically evident in confluent monolayer cultures and cell pellets. Their elongated, epithelioid-to-dendritic morphology and small size during growth are characteristic of diploid, pre-senescent mouse melanocytes cultured with TPA. While growing B16 melanoma cells also exhibit a somewhat elongated epithelioid shape, they differ from Melan-a cells in several key aspects, including being predominantly

non-pigmented, larger, possessing fewer dendrites, and capable of proliferating independently of TPA[75].

To substantiate their non-tumorigenic nature, Melan-a cells at passage 15 were subcutaneously and intravenously injected into syngeneic mice. No palpable tumors were detected at the subcutaneous inoculation site, and even six months post-injection, necropsy revealed no evidence of tumor formation in the s.c. flank region or in the lungs. Macroscopically, no tumor development was observed in any organ. Critically, no net proliferation of Melan-A cells occurred in SMEM medium in the absence of a tumor promoter[75]. A pronounced difference in cellular morphology was observed in quiescent cells, which became flat and isometric without dendrites, whereas optimal cellular yields were achieved after 6 days at 200-500 nM TPA. Visual observations of the temporal morphological changes in quiescent cells indicated that active proliferation commenced in all TPA-containing cultures and sustained growth progressively longer at higher concentrations, suggesting TPA instability under these conditions. When cultured with teleocidin, another potent and mitogenic tumor promoter, maximal cellular yield was attained at a concentration of 20-200nM, not significantly different from that achieved with 200nM TPA. However, reduced mitogenesis was observed at higher concentrations of both TPA and teleocidin. Their inability to proliferate in serum-supplemented medium yet their proliferative response to tumor promoters distinguish Melan-a cells from all known melanoma lines, resembling non-stabilized melanocytes. The intracellular receptor for TPA is protein kinase-C, which is activated upon binding of TPA, teleocidin, and other tumor promoters. This strongly implies that active protein kinase-C is indispensable for normal melanocyte proliferation. Given their absolute dependence on TPA for proliferation, Melan-A cells serve as an invaluable model system for dissecting the actions of tumor promoters and the role of protein kinase-C in cellular proliferation.

Over the years, Melan-a cells have been employed in a diverse range of studies, primarily focusing on cutaneous melanoma. Examples include investigations into the protective effects of infrared radiation against UVB-induced damage in this cell line[76], studies on melanocytic transformation associated with impaired substrate adhesion[77], research aimed at discovering crucial biomarkers for the metabolic fingerprints of murine melanocytes[78]and melanoma cell lines, and the extraction of gene expression signatures for the detection of premalignant melanocytes and early melanomas with metastatic risk[79]. Their consistent utility underscores their continued relevance in advancing our understanding of melanoma biology.

3.2. In vivo models

To gain a comprehensive understanding of UM tumor growth, development, and to facilitate the screening of novel treatments—particularly considering the eye's immune-privileged status—both *in vitro* and *in vivo* models are indispensable. The advent of xenograft models has significantly enhanced the efficiency of drug screening and offers a platform for personalized tumor targeting. Prior to the widespread use of patient-derived xenograft (PDX) models, the inoculation of murine or human cell lines into immunodeficient or immunosuppressed animals (including rats, rabbits, or zebrafish) was a common practice. However, the complex molecular landscape of UM is challenging to fully recapitulate using diverse cell lines alone. In contrast, individual PDX models, which phenotypically and genotypically mirror the characteristics of primary and metastatic tumors, have been developed and are being increasingly employed to determine the most effective therapy for individual patients. Nevertheless, the requisite immunodeficiency in these animal models presents a substantial hurdle to comprehensive immunological studies.

More recently, transgenic animal models of UM have become available. The pioneering transgenic mouse model was generated by inducing the expression of the oncogene *GNAQ-Q209L* under the control of the Rosa26 promoter[80]. This model exhibits neoplastic proliferation in the choroid, alongside dermal nevi and melanocytic neoplasms, with 94% of mice subsequently developing pulmonary metastases. Transgenesis involving mutant *Tp53* in combination with *GNAQQ209L* or *GNA11Q209L* has led to the development of melanocytic tumors, including UM, with nearly complete penetrance[81]. Additionally, mouse models with melanocyte-specific expression of *GNA11Q209L*, with or without homozygous *BAP1* loss, have been established. These models develop pigmented neoplastic lesions originating from melanocytes in the skin, eye, leptomeninges, lymph nodes, and lungs[81]. While the injection of cell lines derived from confirmed metastatic origins into the liver or spleen can induce multiple hepatic and intra-abdominal metastases, mimicking those observed in human UM hepatic metastases (a pseudometastatic model)[82], the creation of an animal model of UM with spontaneous hepatic metastases remains an ongoing challenge[83].

3.3. The use of Blue Light

Reporting on a recent study demonstrating the effects of LED blue light on mouse-derived 661 W cells, it is now possible to further elaborate on the crucial correlation between UM and blue light as a potential environmental etiological agent for UM[110]. This investigation, examining

LED lights of varying colors and intensities, unequivocally demonstrated that blue light inflicts greater cellular damage compared to white and green LED light at equivalent in vitro lux levels, alongside a significant increase in the generation of reactive oxygen species (ROS) compared to white and green LED lights[110]. Initially, the relationship between photoreceptor-derived cellular damage and LED light color was assessed: at a constant light intensity of 2,500 lux, blue light caused more severe damage to photoreceptor cells than white and green LED light. Subsequently, evaluating ROS generation after 24 hours of exposure to three different colored lights at 2,500 lux, blue LED light induced a markedly higher production of ROS compared to white and green LED lights. Specifically, 6 hours of blue light exposure led to a 1.4-fold increase in ROS, while white light exposure for the same duration resulted in a 1.2-fold increase; green LED light exposure for 6 hours, however, did not induce an increase in ROS. Photoreceptor cell death is known to be promoted by oxidative stress induced by ROS generation, and light exposure-induced damage has been confirmed to reduce mitochondrial membrane potential in models of light-induced retinal degeneration. Consequently, the evaluation of mitochondrial membrane potential revealed that blue LED light progressively increased the number of cells in the pro-apoptotic phase in a time-dependent manner.

At the molecular level, blue LED light exposure significantly altered the levels of activated NF-κB, phosphorylated MAPK-p38, and phosphorylated ERK. The heightened generation of ROS, consequent to blue light exposure, induces MAPK activation, which in turn modulates inflammation, cellular apoptosis, and various other crucial cellular pathways. Western blotting was employed to delineate the mechanism of photoreceptor-derived cellular damage following exposure to 2,500 lux LED light. Protein expression of NF-κB, p38, and ERK was detected post-LED exposure, demonstrating a significant increase in activated NF-κB levels 3 hours after blue light exposure, an effect not observed with white or green LED light (20). More recent molecular evidence indicates that spontaneously immortalized Melan-A cells, when exposed to blue light, exhibit a mutational signature strikingly similar to that observed in human UM, but distinct from CM. This finding provides direct support for blue light as a potential mutagenic and tumor-initiating factor, likely contributing to UM tumorigenesis.

Furthermore, human UM cells in culture exposed to blue light (peak 475 nm) have shown a significant increase in their mitotic division rate compared to blue light-shielded controls, an effect that was effectively blocked by a blue light-filtering lens[76]. While the precise mechanism underlying the relationship between blue light and increased uveal melanoma cell proliferation remains to be fully elucidated, it has been demonstrated that shorter wavelengths of light can induce retinal pigment epithelial cell death via mitochondrial-derived ROS production.

Therefore, although specific studies are required, investigating ROS production subsequent to blue light exposure in uveal melanoma cells represents a critical starting point for clarifying this relationship[84]. Investigations into the effects of GNAQ mutation and blue light exposure on choroidal melanocytes suggest that blue light impacts the oxidative status of melanocytes and UM cells, potentially leading to DNA damage that accelerates mutation accumulation, thereby initiating or facilitating UM development. This implies that blue light may act as an "additional hit" in the transformation process of GNAQ-mutant nevi.

The conceptual foundation highlights that visible light of short wavelengths can induce DNA damage, and the acquired secondary mutations may be propagated to subsequent cell generations, leading to the formation of a malignant clone. The fundamental question being addressed is whether blue light alone can induce the malignant transformation of a normal melanocyte. The primary challenge in obtaining a conclusive answer is the paucity of established normal uveal melanocyte cell lines. Even if such cell lines were adequately developed and available, successive passages and immortalization would likely introduce numerous changes in gene expression profiles, rendering comparisons incomplete[50]. Nonetheless, epidemiological studies in pediatric literature provide clinical evidence that blue light can indeed influence normal cutaneous melanocytes. Neonates subjected to blue light phototherapy for jaundice exhibit a higher incidence of dysplastic cutaneous nevi later in life. Both nevus count and average nevus size tend to be greater in the exposed group compared to controls. Given that dysplastic nevi are the most significant predisposing lesions for cutaneous melanoma, this constitutes strong evidence that blue light can induce the transformation of a normal melanocyte into a pre-malignant lesion. However, as previously noted, the human crystalline lens offers natural protection by filtering UV radiation.

CHAPTER II

AIMS

Despite significant advancements in understanding the molecular landscape of UM, this aggressive intraocular malignancy continues to pose substantial challenges in predicting metastatic progression and in achieving effective systemic control once distant dissemination has occurred. Although high- and low-metastatic-risk classes are genomically defined, the unpredictable disease course in a subset of low-risk patients, combined with the limited efficacy of current therapeutic options, underscores the urgent need for novel biological insights and the identification of new therapeutic targets. Furthermore, the exclusion of UV radiation as a primary etiological factor, alongside emerging evidence[50] suggesting a role for blue light (BL) in UM pathogenesis and the unique mutational signatures, highlights a critical gap in understanding environmental contributions to its genesis.

Another critical point in the pathogenesis of UM is identifying the molecular vulnerabilities that may be responsible for its initiation and metastasis. Under this point of view, it has been reported that approximately 90% of UMs harbor activating mutations in the G proteins GNA11 and GNAQ[23], while the remaining 10% harbor activating mutations in a G protein-coupled receptor (CYSLTR2) or phospholipase Cβ4 (PLCB4)[4]. This indicates the essential role of the Gα11/q pathway and, in particular, the phospholipase Cβ (PLCβ) effector pathway in the initiation phase of UM. However, although most UMs harbor such mutations, prognosis is largely determined by the presence of additional contributing mutations. In this regard, monosomy of chromosome 3 has been shown to be associated with a poor prognosis, representing the single most negative prognostic factor. Indeed, inactivating mutations in BAP1, located in 3q21, are considered critical cooperative lesions in determining a poor prognosis[8] . On top of this, as described in the Background chapter, the gain of the long arm of Chromosome 8 is a recurrent chromosomal aberration observed in UM, strongly correlating with increased metastatic risk and poorer patient prognosis[40].

Therefore, this research has mainly focused on shedding light on the etiology and neoplastic progression of UM and on identifying molecular vulnerabilities that could be targeted by new therapeutic approaches.

To address these critical gaps and contribute new molecular insights, a multi-faceted approach was applied. Specifically, the main objectives pursued during this 3-year PhD program were the following:

1. Elucidating environmental contributions and identifying the mutational signatures of BL exposure in a new syngeneic cellular mouse model (Melan-a). To this end, an *in vitro* BL irradiation system was developed. This system was then applied to Melan-a cells firstly to evaluate the impact of BL on melanocytes and secondly, to select a potentially resistant cell line (72A)

2. Validating the mechanisms driving UM's high metastatic propensity in *in vitro* models that reproduce UM's progression and its known intrinsic resistance to therapy. To this end, using the genetic engineering (CRISPR/Cas9) system, cell lines expressing the key molecular alterations of aggressive UM (such as $GNA11^{Q209L}$ knock-in clones and challenging BAP1 knockout lines) were generated.

3. Identifying and validating novel prognostic biomarkers within the common Chromosome 8q gain region. To this end, two independent cohorts of UM patients were employed. A gene panel was first defined through differential expression analysis in the first cohort and subsequently validated in the second cohort, leading to the development of a robust Multigene Score (MGS).

CHAPTER III

Materials and Methods

1. Cell lines

1.1. Melan-a

The Melan-a cell line was purchased from Dr Bennet (St George's University of London).[30] Melan-a cells are diploid and syngeneic with C57BL/6 mice, spontaneously immortalised after approximately 30 culture passages and do not express p16 or ARF, two proteins encoded by CDKN2A. Cells were maintained in RPMI1640 medium (Sigma-Aldrich, St. Louis, MO, USA), enriched with 10% fetal bovine serum (FBS, Sigma-Aldrich) and 200 nM TPA (tetradecanoyl phorbol acetate, Sigma-Aldrich, Merck, Darmstadt, Germany). The cells were grown in an incubator at 37° C and in a humidified atmosphere with 10% CO_2.

1.2. 72A

This cell line resulted from the proliferation of Melan-a cells that survived 72 hours of consecutive exposure to blue light (BL). The culture conditions were identical to those of the parental cell line.

1.3. C2

This C2 cell line was derived from the Melan-a cell line following an unsuccessful GNA11 gene knock-in attempt via CRISPR/Cas9 technology (refer to the CRISPR/Cas9 paragraph for further details). The resulting C2 cell population was rigorously verified to be completely homogeneous and wild type, mirroring the parental Melan-a line through Sanger sequencing methodology. Throughout these experiments, the culture conditions for the C2 cell line remained identical to those of the parental Melan-a cell line.

2. Treatments

2.1. Blue Light (BL)

Two Elixa lamps (Ldt.) with 120 blue LEDs emitting at a visible length of 470nm were placed in the incubator and used to expose the Melan-a cell line to BL. The cells were irradiated at 66.5W/m2 from above at a 37cm distance between the cell adhesion surface and the lamp.

To determine the optimal cell concentration for facilitating cell growth during 72-hour continuous exposure to BL, several pilot studies were conducted. A seeding density of 200,000 cells/well in 6-multiwell plates (Corning Incorporated, Corning, NY, USA) or 1 × 10^6 cells/T25

flask (Corning) was defined. This seeding density has been proved optimal for sufficient cell survival in the immediate post-exposure period and a subsequent, although slow, regrowth after treatment. Moreover, to exclude possible interference between BL and red phenol, a pH indicator dye, during these experiments, cells were maintained in RPMI medium without phenol red. Once the exposure time was over, the cells were incubated in the dark, and the fresh medium used to re-establish the proper cell growth was enriched with 20% FBS.

3. Functional assay

3.1. Cell viability (MTS)

Cell viability was tested by seeding and treating the cells ($15x10^3$ cells/well) in 96-well plates (Corning At the end of the exposure/treatment, the culture medium was removed, replaced with fresh medium and then, cells were incubated with 20 uL of CellTiter AQueous One Solution Reagent (CellTiter 96® AQueous One Solution cell proliferation assay (Promega, Madison, WI, USA). The plates were incubated in the dark at 37° C, 10% CO_2, for 3h. The conversion of tetrazolium to tetrazane takes place only in living cells, and the amount of intracellular formazan was measured spectrophotometrically by using CLARIOstar plus (BMG LABTECH, Offenburg, Germany) plate reader with Clariostar control software 5.70 R2 and MARS (BMG LABTECH). Data Analysis software 3.42 at 490 nm absorbance.

3.2. Flow Cytometry

Muse system (Cytek® Muse® Micro Cell Analyzer)

The Cytek Muse Micro cell analyzer is a compact flow cytometer capable of detecting forward scatter (FSC), side scatter (SSC), and up to three fluorescent parameters for cellular analysis. This instrument was utilized in the current study for its ability to provide quantitative and objective assessment of single-cell properties, which is essential for applications such as DNA damage, oxidative stress, and apoptosis assays.

3.2.1. DNA damage

Total DNA damage was assessed in Melan-a cells following exposure to light stimulus and in respective control cells using the Muse® Multi-Color DNA Damage kit (Part Number: MCH200107). This kit employs phospho-specific antibodies targeting ATM (Ser1981) and Histone H2A.X (PE-Cy5 conjugated) to simultaneously detect the phosphorylation status of these key DNA damage response proteins via flow cytometry, thereby providing a quantitative measure of DNA double-strand breaks and ATM activation.

3.2.2. Oxidative stress

Oxidative stress was evaluated as Reactive Oxygen Species (ROS) production in Melan-a cells following 24h, 48h, and 72h of blue light (BL) exposure using the Muse® Oxidative Stress kit. This assay quantifies the relative percentage of ROS-negative and ROS-positive cells based on the intracellular detection of superoxide radicals via a dihydroethidium-based reagent.

In addition, ROS production analysis was also performed by labelling cells with dichlorofluorescein-diacetate (DCFH-DA, Sigma-Aldrich).

To obtain a positive control of ROS production, Melan-a and 72A cell lines were exposed to increased concentrations (10uM - 1M) of H_2O_2 and 50uM was considered as the optimal concentration for the aim. Then, both Melan-a and 72A cell lines were exposed to BL or treated in dark (in a second incubator) with 50uM H_2O_2 for 3h, 12h, 24h, 48h and 72h. For each BL-H_2O_2 treatment pair of wells, a third well was kept in the dark, not receiving any treatment and used as a negative control.

After the treatments, cells were incubated with 5uM 2'-7' dichlorofluorescein-diacetate (DCFH-DA; Sigma-Aldrich) at 37° C for 30 min. Afterwards, this solution was removed and the cells were incubated with 90% DMSO in PBS. Finally, the cells in the plates were scraped and stirred at 300-400 rpm for 10 min., before the fluorescence analysis. CLARIOstar plus (BMG LABTECH) plate reader with Clariostar control software 5.70 R2 and MARS Data Analysis software 3.42 was used for the lecture of the DCFH expression, at em 530 +/-30 nm and ex 483 +/-14 nm.

3.2.3. Apoptosis

Apoptosis was quantitatively analyzed in Melan-a cells following 24h, 48h, and 72h of blue light (BL) exposure using the Muse® Annexin V & Dead Cell Kit (Part Number: MCH100105). This kit facilitated the distinction and quantification of live, early apoptotic, late apoptotic, and dead cell populations.

To further investigate the anti-proliferative effect of blue light (BL), the Annexin V-Propidium Iodide apoptosis assay was employed, comparing Melan-a cells exposed and unexposed to blue light for 72h. Annexin V (eBioscienceTM Annexin V Apoptosis Detection Set PE-Cyanine7 - Invitrogen) was chosen as the specific marker for FACS analysis of apoptotic events.

4. Gene expression analyses

Gene expression analysis was performed using the Affymetrix high-density microarray platform, specifically the Applied Biosystems™ Human Genome U133 Plus PM Array Strip, to evaluate the effect of Blue Light on the Melan-a cell line. This technique involves hybridizing labeled nucleic acids from samples to chemically synthesized DNA probes on a quartz surface, with gene expression levels determined by fluorescence detection. The platform employs both perfect match and mismatch probes to ensure high specificity and accurate signal quantification.

4.1. CRISPR/Cas9

CRISPR is a revolutionary gene editing technology used for precise genetic alterations, and the protocol "CRISPR editing of Immortalized Cell Lines with RNPs Using Nucleofection" by SYNTHEGO was customized through multiple trials to suit the specific requirements of the Melan-a cell line and the desired genetic modifications.

4.1.1. Whole Genome Sequencing (WGS)

It is extensively recognised that human genes GNA11, GNAQ, and BAP1 are correctly aligned with the *Mus Musculus* reference sequence. In order to evaluate if this alignment is also comparable between *Mus Musculus* and Melan-a cells, Whole-Genome Sequencing (WGS), a method for analysing entire genomes, was performed, and the results were examined by bioinformatic approach using a published strategy[31]. The sequence alignment, performed with sarek nextflow pipeline (https://nf-co.re/sarek/3.2.3), produced BAM files used for variant calling. This latter analysis was performed applying three methods (varscan2, strelka, mutect2), and those detected by at least two of the three methods and not shared by multiple samples (e.g., to avoid mutation under selection or possible germline variants) were classified as 'variants'. Variant files (vcf) were annotated with VEP (variant effect predictor-Ensembl) to detect and remove germline variants. Mutation signatures of cell lines (Melan-a and *Mus Musculus*) were detected using sigprofiler on filtered vcf file.

4.1.2. DNA and RNA extraction

To extract total DNA/RNA or only total RNA from the cells, the Qiagen's (Duesseldorf, Germany) AllPrep® DNA/RNA Mini Kit or the RNasy® Plus Micro kit were used, respectively.

4.1.3. PCR, Purification, Agarose Gel Electrophoresis, and Quantification

Primers (Forward/Reverse) for classic PCR were designed with the Primer-BLAST (NCBI) tool. PCR was performed with Immolase DNA Polymerase (Meridian Bioscience, Ohio, USA) kit and the product obtained was run on 1.5 % agarose gel at 65V for 35 min. and 70V for 20 min., purified with GeneUP^{TM} PCR Cleanup Kit (BiotechRabbit, Berlin, Germany) and quantified via Nanodrop system. Purification of the PCR product was performed only if the gel showed clean and well-defined bands. Similarly, only if the nanodrop quantification showed good quantity and quality values in the 260/280 and 260/230 ratios (purity indicators), the products were sent to the BMR Genomics (start-up born as a University of Padua spin-off) for Sanger sequencing to investigate the genomic locus of the possible variant of the genes.

4.1.4. RT-PCR

To obtain the coding sequencing (CCDS) relative to the target gene from the RNA extracted from the cell lines, a Reverse Transcriptase PCR with the cDNA synthesis kit (BiotechRabbit) was performed, then the subsequent analyses were the same as described above.

4.1.5. Sanger sequencing and lecture

Sanger sequencing was performed by Italian start-up company BMR Genomics to obtain the genomic sequence or the CCDS sequence of the genes of interest. BMR Genomics offers the standard Sanger sequencing service using Brilliant Dye terminator 1.1 kits, providing them with the Forward/Reverse primers used for PCR/RT-PCR with the corresponding purified product.

Once the Sanger nucleotide sequences were obtained, they were compared with wild-type ones *via* alignment on Sequence Navigator, a multiple sequence alignment software. The alignment allows i) to verify whether the genomic sequence of MelanA wt line is superimposable with that of *mus musculus* for regions taken into analysis; ii) to identify if and which changes are found in specific locus after treatments and/or gene editing *via* CRISPR/Cas9, and what impact they have on translation into proteins.

4.1.6. gRNA and DNA donor design

To obtain a syngeneic cellular mouse model reflecting the mutational landscape of uveal melanoma, Melan-a cell model was submitted to gene editing *via* CRISPR/Cas9: GNA11^{Q209L} KI and BAP1 KO.

For each gene, three different gRNAs and, for the KI, a single-stranded DNA donor were designed. GNA11 gene is edited by CRISPR-Cas9 to insert the Q209L variant. To design the gRNAs, the CRISPRevolution Synthetic sgRNA Kit by SYNTHEGO (California, USA) was

used; instead to design the donor templates were used five online tools as described in https://zlab.bio/guide-design-resources (CRISPR, IDT, CHOPCHOP, CRISPick- Broad Institute, and Synthego), providing a target the genomic sequence of the exons where to find the Cas9 cutting sites. The one from IDT (Integrated DNA Technologies) has been selected.

4.1.7. Nucleofection

Nucleofection of Melan-a was performed using the 4D-Nucleofector® System (Lonza, Gampel, Swiss) after having found the most efficient transfection conditions choosing among several electroporation programs.

In each trial, five different controls were prepared:

- GFP, positive control of transfection efficiency;
- gRNA +, editing control (Rosa26), it creates KO;
- gRNA -, the absence of gRNA prevents the binding between the components of CRISPR/Cas9 in the region of interest;
- Negative control, non-electroporated line;
- Cell line solely electroporated, in which the CRISPR/Cas9 constructs have not been added.

Transfection efficiency was evaluated 48h after nucleofection using both the Olympus 1x51 fluorescence microscope and the CytoFLEX-S (Beckman Coulter, California, USA) instrument with the FlowJo software. This GFP's GFP-based evaluation allowed to identify the optimal Nucleofector program to use: SE DS150.

4.1.8. Single-cell Sorting

Single-cell sorting was performed to achieve a sterile plating of cellular clones on a 96-multiwell plate at a density of 1 cell/well after CRISPR/Cas9 editing. The used BD FACSAria™ IIu instrument enabled not only single cell plating but also, through the ACDU sorting platform, the separation of cells based on physical parameters such as cell size (FSC, forward scatter) and complexity (SSC, side scatter).

4.1.9. Clonal expansion

After sorting, cells (1 cell/well) were plated in five 96-multiwell plates and incubated in the dark with RPMI medium. Upon reaching confluence in the 96-well plate, the cells were transferred to a 24-well plate and expanded. Upon reaching confluence, the cells were detached, half of the pellet was frozen, one quarter had its DNA extracted, and the remaining quarter was further

propagated for expansion. After expansion on 6-multiwell plates, cells were again divided for DNA/RNA/protein extraction and further analysis to validate the proper functionality of the CRISPR/Cas9-mediated editing.

5. Statistical analyses

Data are expressed as means ± SEM of at least three independent experiments in which three different wells were analyzed every time for each experimental condition. Statistical significance of differences was determined by one-way analysis of variances (ANOVA); $p < 0.05$ was considered statistically significant.

To validate the *in vitro* results, a study was conducted on UM tissues obtained from patients.

6. Formalin-Fixed Paraffin-Embedded (FFPE) UM samples

Formalin-fixed paraffin-embedded (FFPE) enucleated eyes from patients diagnosed with primary uveal melanoma were retrospectively collected from two collaborating research laboratories: the laboratory of Prof. Levesque at the University Hospital Zurich (USZ), Switzerland (n = 9), and the laboratory of Prof. Stålhammar at the Karolinska Institute, Stockholm, Sweden (n = 47). The specimens from USZ were obtained from patients enucleated between 2020 and 2024, while those from the Karolinska Institute were collected between 2000 and 2008. All samples consisted of whole eyes embedded in paraffin, allowing analysis of primary tumor tissue. Inclusion criteria required the presence of an adequate amount of tumor tissue suitable for both immunohistochemical (IHC) and whole exome sequencing (WES) analyses; samples not meeting these requirements were excluded from the study. Following this initial assessment, a subset of samples was excluded due to insufficient tumor content, resulting in a final cohort of 45 patients: 3 from USZ and 42 from the Karolinska Institute.

6.1. Slide preparation

To perform these analyses, FFPE samples were cut using the Zeiss Hyrax M25 microtome, with a chosen thickness of 3 µm. The sections were spread on Superfrost Plus Adhesion Microscope Slides (epredia) for classical IHC/FISH, and Superfrost Gold Plus Adhesion Microscope Slides (epredia) for Multiplex (Akoya Bioscience).

6.2. Hematoxylin and Eosin (H&E) staining

The H&E staining technique was employed as the foundational method for morphological assessment. H&E is a routine histological stain where Hematoxylin markss cell nuclei

blue-violet, and Eosin colors the cytoplasm and extracellular matrix pink. This step was crucial for primary quality control: it was performed on all UM samples to both assess the quality of the FFPE samples and verify critical anatomical structures within the specimens.

6.3. Antibodies

The antibodies (Abs) used to analyze in IHC the expression of the target proteins were chosen taking into account the gene expression, the gene mean methylation on the UM dataset, the possibility of being a druggable targets and the role that these target proteins play in different tumors (as will be explained in the Results section).

The Abs used are listed below:

- PUF60 Monoclonal Antibody (GT677) | Invitrogen (thermofisher.com)
- NDRG1 Antibody (NBP1-86636) | (Novus Biologicals)
- Anti-NDUFB9 antibody [EPR15955-78] (ab200198) | (Abcam)
- Anti-LAPTM4B antibody [CL5289] (ab242376) | (Abcam)
- PTK2 Monoclonal Antibody (OTI4G7) (CF506182) | (thermofisher.com)
- Anti-MAF1 antibody (GTX106776) | (GeneTex)
- YWHAZ antibody (67698-1-Ig) | Proteintech (ptglab.com)
- IHC‑plus™ Monoclonal Mouse anti‑Human ASAP1 Antibody (LS‑B14317) | (LSbio)

Prior to application on uveal melanoma samples, antibody concentrations were optimized using separate sections from the same FFPE kidney or colon tissue block, selected as a positive control based on expression data from The Human Protein Atlas.

6.4. Immunohistochemistry (IHC)

All the staining procedures were performed with Leica Bond RX (Biosystem), an automated staining system used for high-throughput immunohistochemistry (IHC), and Multiplexing applications.

IHC protocols

Prior to the immunohistochemical (IHC) staining protocol, all prepared UM-slides underwent a melanin bleaching procedure to remove endogenous pigment from the samples. This protocol involved a standard deparaffinization (dewax) process using xylene and graded alcohols (e.g.,

100% ethanol, 80% ethanol), followed by a 15-minute incubation in a KOH/H_2O_2 solution. Two subsequent 5-minute washes in dH2O were then performed. Following these steps, the slides were either immediately transferred to the Leica Bond RX (Biosystem), or stored in Phosphate-Buffered Saline (PBS) solution at 4°C for a maximum of 12 hours.

For all the Ab was used the Leica Bond RX IHC Protocol Red 15 min.

- PUF60, HIER 20 min with ER2 100C, dil 1:350
- NDRG1, HIER 20 min with ER2 100 C, dil 1:100
- NDUFB9, HIER 30 min with ER2 95 C, dil 1:500
- LAPTM4B, HIER 30 min with ER2 95 C, dil 1:500
- PTK2, HIER 20 min with ER2 100 C, dil 1:250
- MAF1, HIER 20 min with ER2 100 C, dil 1:50
- YWHAZ, HIER 20 min with ER2 100 C, dil 1:1200
- ASAP1, HIER 20 min with ER2 100C, dil 1: 750

After the staining, the slides were automatically mounted using the Leica HistoCore SPECTRA CV system. Then scanned using the Ventana DP200 (Roche) scanner, and the images were analyzed through the Ventana Viewer software (Roche).

7. Fluorescence In Situ Hybridisation (FISH)

To assess the amplification of chromosome 8q, FISH technique was used. In this study, to detect copy number changes at the DNA level and confirming or not the presence of 8q gain, the Histology FISH Accessory Kit (Agilent Dako) and the probe targeting ASAP1 (gene localised on the 8q region), together with the relative reference probe for the Chr8 (Empire Genomics) were used. The slides were analysed by the ZEISS LSM 900 confocal microscope equipped with Airyscan 2 as area detector and observing different zones within the tissue.

8. Whole Exome Sequencing

Moreover, the assessment of chromosome 8q amplification was further evaluated by whole-exome sequencing (WES) performed by NovoGene- a global leader in Next-Generation Sequencing (NGS), Proteomics, and Metabolomics services.

Genomic DNA was extracted from FFPE tissue sections using the QIAamp DNA FFPE Tissue

Kit (Qiagen). The protocol includes optimised lysis conditions and employs QIAamp MinElute spin columns to ensure efficient recovery of high-quality DNA in low elution volumes. To obtain a sufficient DNA yield for downstream WES, three 10 µm-thick paraffin tissue rolls per sample were processed.

8.1. Quantification -Tape Station

To ensure the suitability of the extracted DNA for WES, DNA concentration and integrity were assessed by the Agilent TapeStation system with the High Sensitivity D1000 ScreenTape assay.

8.2. Human Whole Exome Sequencing

DNA libraries were prepared using the Agilent SureSelect Human All Exon V6 enrichment kit. Sequencing was carried out on the Illumina NovaSeq X Plus platform with a paired-end 150 bp (PE150) strategy, generating approximately 12 Gb of raw data per sample.

9. Data Analysis and Computational Tools

9.1. Bioinformatic analysis

- To evaluate the copy number status and expression of chromosome 8q genes, providing a genomic-level assessment of alterations of interest, the RStudio, an integrated development environment (IDE) for the R programming language, was employed for the analysis of publicly available scRNA-seq datasetsGSE139829 (https://www.ncbi.nlm.nih.gov/geo/query/acc.cgi?acc=GSE139829).The analysis incorporated several R packages, including CNVranger and IGC for copy number variation inference, Seurat for single-cell analysis, and DropletUtils to remove empty droplets.
- To detect variants on Whole Genome and consequently comprehend the 8q status of our dataset, WES data have been analysed through nf-core/sarek workflow (https://github.com/nf-core/sarek/tree/3.5.1). The sequence alignment, performed with sarek nextflow pipeline, produced bam files used for variant calling. This analysis was performed applying four methods (freebayes, strelka2, deepvariant, cnvkit), and those detected by at least three of the four methods and not shared by multiple samples (e.g., to avoid mutation under selection or possible germline variants) were classified as “variants”. Variant files (vcf) were annotated with VEP (variant effect predictor-Ensembl) to detect and remove germline variants.

- Pearson's correlation coefficient was utilized to quantify the strength and direction of linear relationships between two continuous variables.
- Kaplan-Meier analysis was employed to estimate and visualize survival probabilities over time, allowing for the comparison of survival distributions between different patient groups.
- Multivariate Cox regression analysis was performed to assess the independent contribution of multiple variables simultaneously on a specific time-to-event outcome, while accounting for potential confounders.

9.2. QuPath

QuPath, an open-source software for digital pathology, was used to analyze immunohistochemistry (IHC) images obtained from FFPE tissue sections of patient samples. It enabled high-throughput quantification and spatial mapping of protein expression for selected 8q targets, facilitating correlation with genomic and transcriptomic findings. QuPath's capabilities in multiplex staining interpretation and spatial phenotyping were particularly suited to this application.

To comprehensively address the interpretation of immunohistochemical stains, image analysis was systematically performed using QuPath. Following the acquisition of the stained slide image, the analysis was strictly focused on the entire tumor area, which was manually delimited to exclude surrounding healthy tissue. The first step involved Cell Detection. Parameters were carefully calibrated to ensure the selective recognition of tumor cells only (eg. cell width was fixed at 7um, allowing for the exclusion of smaller inflammatory or lymphocytic infiltrate cells, thereby concentrating the analysis on the neoplastic population). Once the accuracy of cell recognition was verified, the positivity quantification (Cell Positivity) for the target antibody was implemented. Since the optimal antibody concentration had been previously determined using control tissues (ensuring the absence of false positives or negatives), the positivity thresholds in QuPath were set to achieve a semi-quantitative stratification of protein expression: initially, cells were broadly classified into Positive and Non-Positive groups; subsequently, three positivity thresholds (Semi-quantitative thresholds: Num+1, Num+2, and Num+3) were defined within the positive population. The final analysis output provided the percentage of negative cells and, within the positive cells, a ranking based on the staining intensity: low positive (Num+1), medium positive (Num+2), and highly positive (Num+3). This methodology allowed for the quantification of antibody expression across whole tumor sections and facilitated the correlation

of protein expression intensity with genomic findings.

9.3. TISCH2

The Tumor Immune Single Cell Hub 2 (TISCH2) is an online resource providing curated single-cell RNA-seq (scRNA-seq) datasets from human and murine tumors. In the preliminary phase of this study, TISCH2 was used to explore the expression profiles of potential candidate genes located on chromosome 8q within the tumor microenvironment across multiple cancer types. This allowed us to assess whether our selected targets showed relevant expression patterns in uveal melanoma and other malignancies before proceeding to validation experiments on patient-derived samples. The datasets used were: UVM_GSE139829 (PMID 31980621), UVM_GSE138433 (PMID 33462406), UVM_GSE160883 (PMID 34518527), and UVM_GSE169609 (PMID 33811047).

10. TMA

Tissue microarrays (TMAs) are paraffin blocks in which up to 1000 individual tissue cores can be arranged in an array format, enabling high-throughput histological analysis. Following IHC characterization of individual UM samples (whole eyes), TMA blocks including all study cases were constructed. For each eye, three tissue cores were selected: one from the tumor border, one from the tumor core (preferably including areas with inflammatory infiltrates), and one from adjacent non-tumoral tissue, typically from the ciliary body. Cores were embedded into recipient blocks using the Xenium frame system. This setup allowed TMA sections, containing all samples, to be cut with a microtome and precisely positioned within the capture area of the Xenium slide, enabling direct downstream processing.

CHAPTER IV

RESULTS

1. *Blue Light as an Additional Etiological Factor*

1.1 Experimental setup

To achieve the primary objective of this thesis of identifying the role of the higher-energy portion of visible light (blue light) in the etiology of uveal melanoma, functional studies and gene expression profiling were conducted on the BL-exposed Melan-a cell line.

The initial phase involved establishing the experimental setup, encompassing both the physical integration of the LED lamp into the incubator *(Fig.1 A)* and the subsequent exposure of the Melan-a cell line to the light stimulus *(Fig.1 B,C)*.

A

B

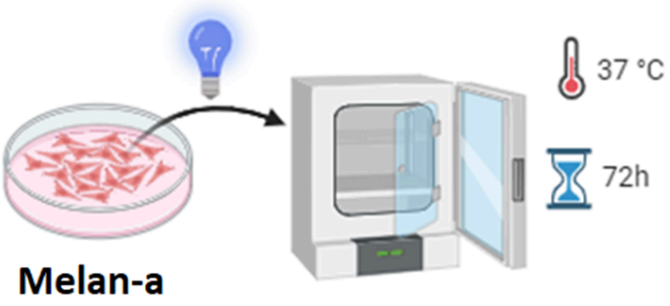

C

Fig. 1 | (A) Incubator setting. (B-C) Workflow for the establishment of blue light (BL) exposure in the Melan-a cell line and selection, after wash-out, of the cell line surviving to 72h of BL exposure (20x magnification). To exclude any indirect effects of the light control cells (BL-unexposed) were maintained in another incubator and grown under the same conditions of BL-exposed cells.

1.2 Functional analyses

Following the establishment of the experimental setup, functional analyses were conducted to evaluate the biological effects of BL. To assess the effects of BL on cell viability, the MTS assay was performed. As reported in *Fig.2*, BL exposure significantly (p=0.0300) reduces the proliferation of Melan-a cells (assessed via cell viability, OD) by approximately 77.3% compared to unexposed cells (Ctr) after 72 hours.

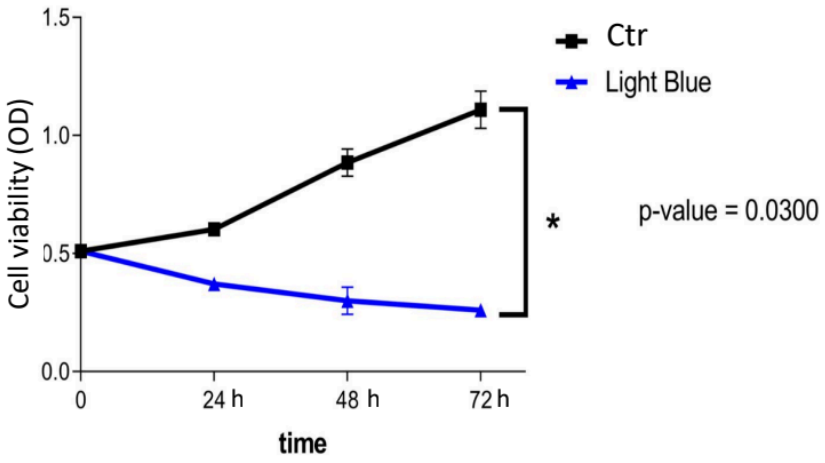

Fig.2 | Anti-proliferative effect of 72 consecutive hours of BL exposure on Melan-a cells. The Light Blue treatment causes a constant and significant reduction in cell viability compared to the Ctr across all measured time points.

To shed light on the mechanisms underlying the anti-proliferative effect of BLexposure, functional assays such as assessment of apoptosis, cell cycle, DNA damage and oxidative stress were conducted.

Analyzing the pro-apoptotic effect of BL, it was demonstrated that BL exposure exerts a potent pro-apoptotic effect on Melan-a cells, peaking at 48 hours, where the rate of apoptotic cells increases from approximately 10% (Control) to 60% (Treated). Although the rate of apoptosis stabilizes at 72 hours, the observed statistical significance at this interval confirms that BL

maintains an extremely significant impact on the overall cell population, drastically reducing viable cells (*Fig. 3 and 4*).

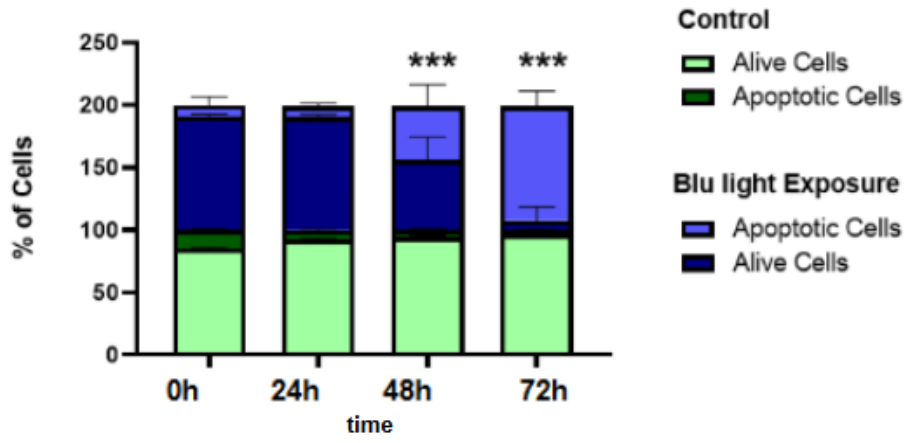

Fig.3 | Pro-apoptotic effect of BL exposure on Melan-a cell line at different time points.

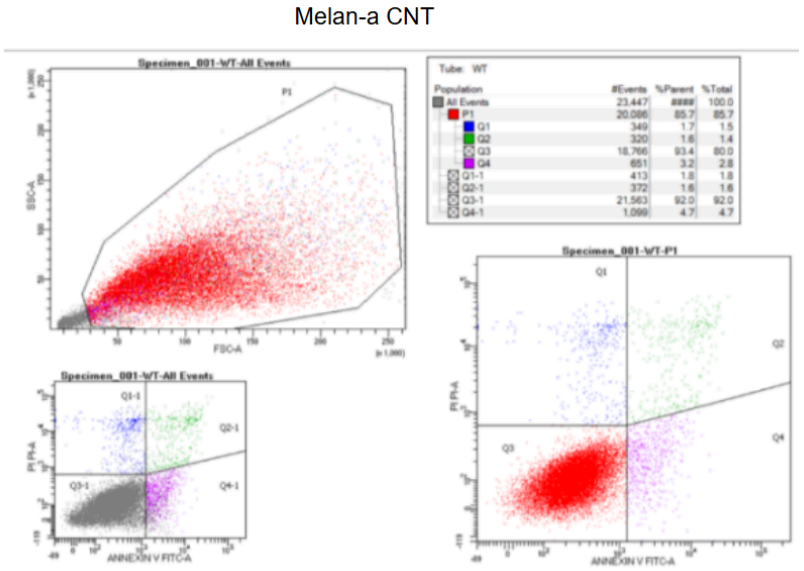

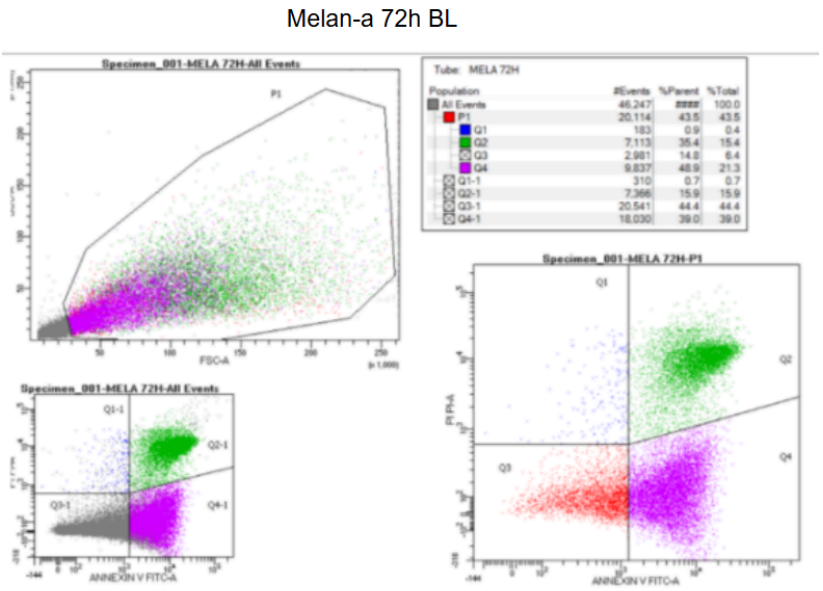

Fig.4 | Pro-apoptotic effect of 72 consecutive hours of BL exposure on the Melan-a cell line compared to control.

Cell cycle analysis (*Fig.5*) showed that 72 h of BL exposure significantly reduced the percentage of cells in the G0/G1 phase (27.64% in control vs. 18.90%in exposed cells). Concomitantly, a significant increase in the proportion of cells in the S phase was observed (55.62% in control vs. 64.01% in exposed ones), while the percentage of cells in G2/M phase remained relatively stable (16.74% in control vs. 17.09% in exposed cells).

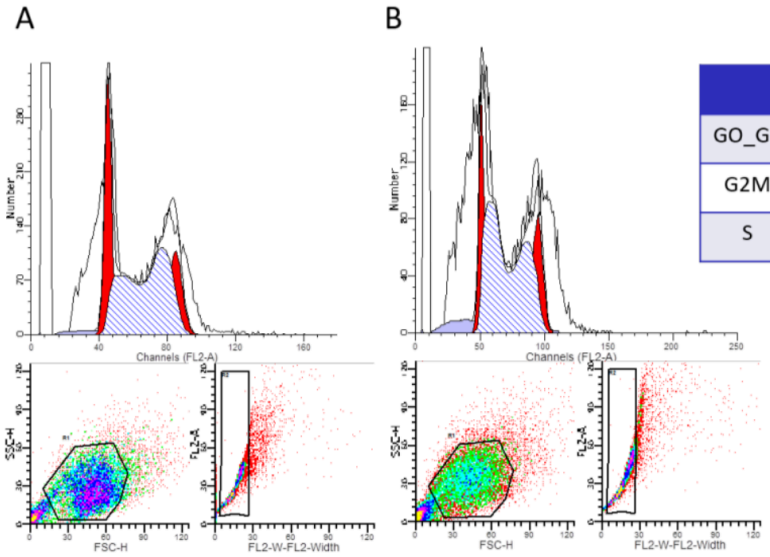

	Melan-a	Melan-a BL 72h
GO_G1	27.64%	18.90
G2M	16.74%	17.09
S	55.62%	64.01

Fig.5 | Effect on cell cycle of 72 consecutive hours of blue light exposure on the (B) Melan-a cell

line compared to (A) control.

Evaluation of total DNA damage demonstrated that BL is not genotoxic (*Fig. 6*). Although in Melan-a cells exposed to BL, there was a slight decrease in the number of cells classified as "Negative" (~87%) compared to control cells (~96%) and a parallel increase in cells with "Total DNA Damage" (~18%) compared to control group (~2%), these changes were not statistically significant (ns).

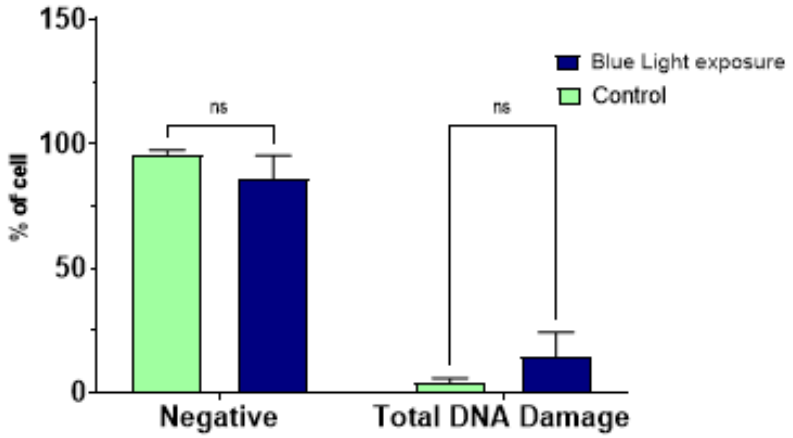

Fig.6 | Assessment of total DNA damage in Melan-a cells exposed to BL.

Furthermore, BL exposure induced a progressive increase in ROS production, reaching a statistically significant change at 72 h (*** $p < 0.001$ vs. control), while this effect was not observed in unexposed cells (*Fig. 7*).

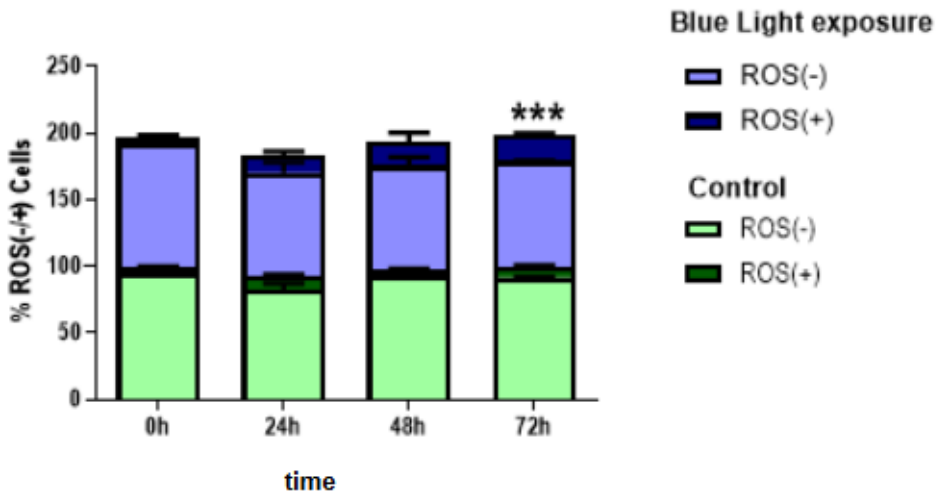

Fig.7 | Time-dependent effect of BL exposure on ROS production in Melan-a cells.

Since BL has been shown to induce oxidative stress in irradiated skin[85] and its pro-oxidant action underlies retinal damage[86], the reversibility of BL-induced effects and the potential cellular adaptation to this exposure were assessed in our model. Therefore, cells that survived to 72-hour of BL exposure were re-cultured for one month under the same experimental conditions as the dark control. This approach led to the selection of the 72A cell line which represents an adapted and potentially resistant phenotype.

In this experimental phase, and considering the varying cytotoxicity of H_2O_2 across cell types, both parental Melan-a cells and the derived 72A cell line were subsequently re-challenged with BL or treated with hydrogen peroxide (H_2O_2). The H_2O_2 challenge was specifically introduced to determine if the 72A cell line, potentially adapted to BL-induced oxidative stress, exhibited a greater resistance to general oxidative damage compared to the parental Melan-a cells.
Assessments of proliferation ratio, ROS production, and viability were conducted across different time points up to 72 hours.

Analysis of the proliferation curves revealed that the parental Melan-a line, undergoing its first BL exposure cycle, exhibited a proportionally greater proliferative decrease compared to the 72A line exposed for a second cycle *(Fig.8)*. This indicated that the 72A cell line demonstrated a significant recovery from the initial proliferative inhibitory effect and an increased resistance to blue light upon re-exposure to the stimulus.

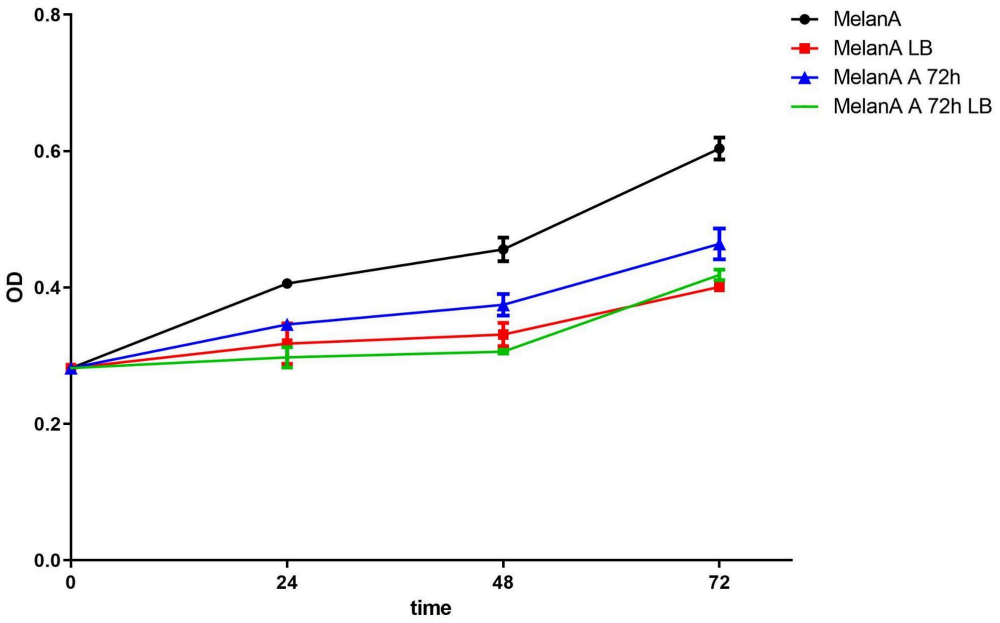

Fig.8 | Anti-proliferative effect of 72 consecutive hours of BL exposure on Melan-a and Melan-a 72A cell lines compared to their respective controls, as determined by MTS assay. The chosen time points were 24, 48, and 72 hours.

To determine if the 72A cell line, potentially adapted to high stress, exhibited a greater resistance to general oxidative damage compared to the parental Melan-a cells, Melan-a and 72A cell lines were exposed to increased concentrations (10µM - 1M) of H_2O_2 *(data not shown)*, and 50µM was considered the optimal concentration for the subsequent analyses serving as positive control for ROS production. Therefore, both cell lines were exposed to BL or treated in dark (in a second incubator) with 50µM H_2O_2 for 3h, 12h, 24h, 48h and 72h. For each BL or H_2O_2 treatment pair of wells, a third well was kept in the dark not receiving any treatment and used as a negative control. Analyzing the cell viability of both cell lines it was observed that the exposure to BL or H_2O_2 induces a marked cytotoxic effect in 72A cells only after 72h (with viability dropping to ≈50% for LB [**] and ≈75% for H2O2 [*]). Conversely, Melan-a cells show no significant changes in viability at 72h or at any other time point *(Fig.9)*.

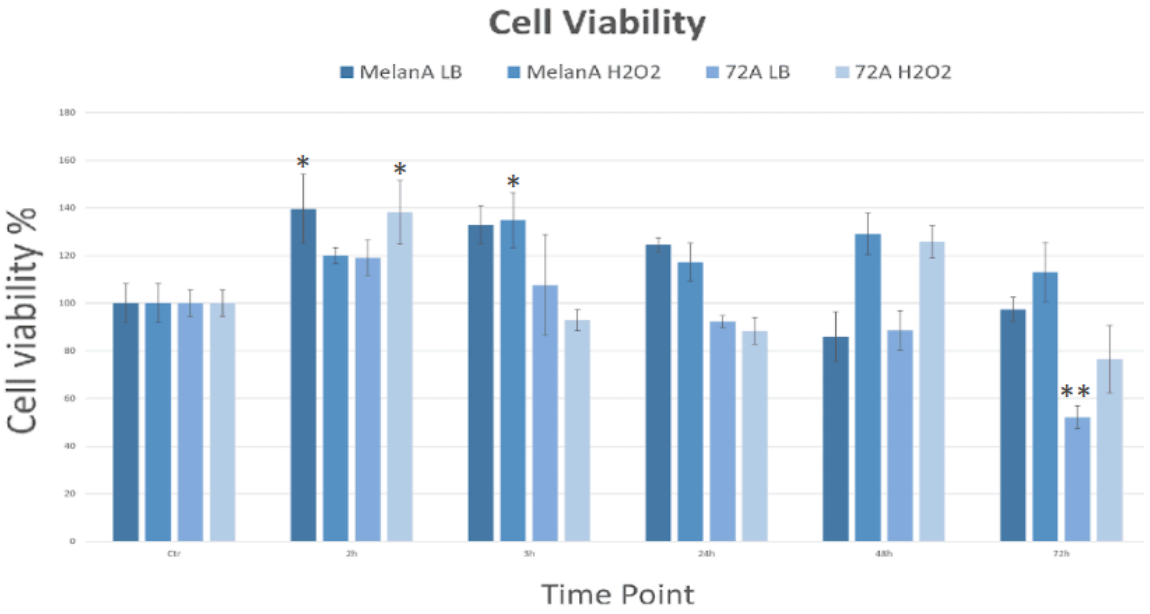

*Fig.9 | Cell viability % in parental Melan-a and derived 72A cell lines following BL (LB≡BL) or H_2O_2 exposure for different Time Points (3h, 12h, 24h, 48h and 72h). * p<0,05, ** p<0,01, *** p<0,001, **** p<0,0001.*

Since it has been demonstrated that BL induces oxidative stress in irradiated skin[85] and that BL-induced pro-oxidant action underlies retina damages[86], and considering that H_2O_2 is found to be more cytotoxic for 72A cells compared to Melan-a, intracellular H_2O_2 levels were monitored. It was indeed observed that both parental Melan-a and the derived 72A cells displayed similar high H_2O_2 baseline levels, ranging from approximately 12,000 to 13,000 DCFH/µg protein *(Fig.10)*. In contrast to expectations, starting from 3h BL re-exposure, a significant decrease (approximately 50% at later time points) in intracellular H_2O_2 production was found in both cell populations compared to untreated cells. Conversely, treatment with H_2O_2 50uM (Melan-a H_2O_2 and 72A H_2O_2) consistently induced a robust and highly significant increase in ROS production across all subsequent time points (e.g., **** $p < 0.0001$ vs. control at 3h onwards) (*Fig.10*).

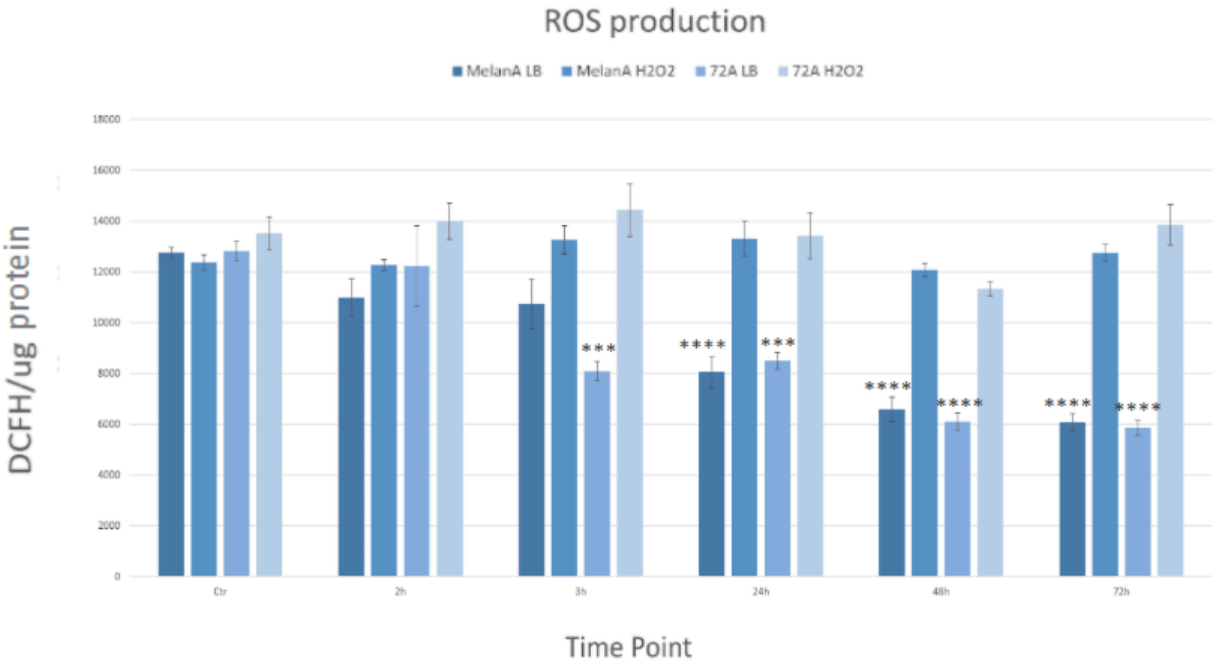

*Fig.10 | Reactive Oxygen Species (ROS) production in parental Melan-a and derived 72A cell lines following BL (LB≡BL) or H_2O_2 exposure. * p<0,05, ** p<0,01, *** p<0,001, **** p<0,0001. Bar graph showing intracellular ROS levels (DCFH/µg protein) over a 72-hour time course. **** p < 0.0001 vs. control *** p < 0.001 at 3h. Data are expressed as mean ± SEM. of three experiments.*

1.3 Differential gene expression profiling

To assess whether, as hypothesized, BL may play a crucial role in the pathogenesis of UM, differential gene expression analysis was performed *via* microarray on both unexposed Melan-a cells, Melan-a exposed to BL for 72 hours, as well as on 72A cells. As shown in *Fig.11A*, Principal Component Analysis (PCA) identifies three clearly distinct sample groups. This spatial distribution is consistent with the identification of 862, 2580, and 3625 genes statistically differentially expressed in unexposed Melan-a cells and those exposed to BL for 72h, in Melan-a exposed to BL for 72h and in 72A cells, and between unexposed Melan-a and 72A cells (*Fig. 11B)*, respectively.

A

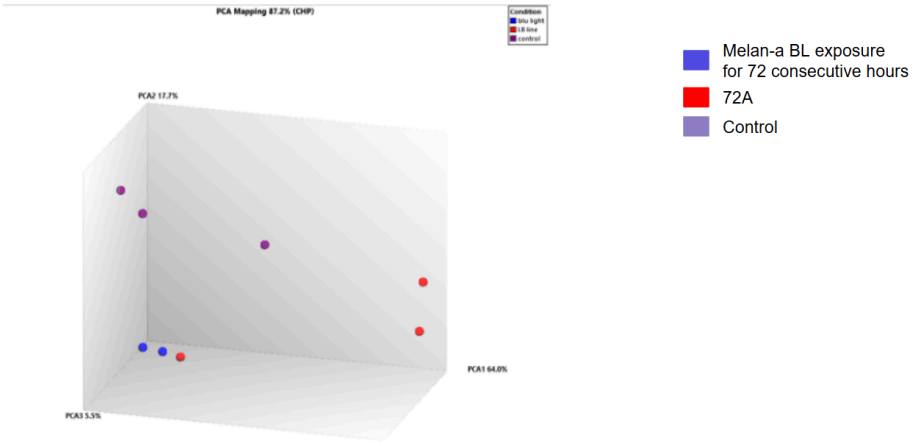

B

Comparison	Group 1	Group 2	Count 1	Count 2	Up	Down
blu light vs control	blu light	control	2	3	399	463
blu light vs LB line	blu light	LB line	2	3	1955	625
control vs LB line	control	LB line	3	3	2737	888

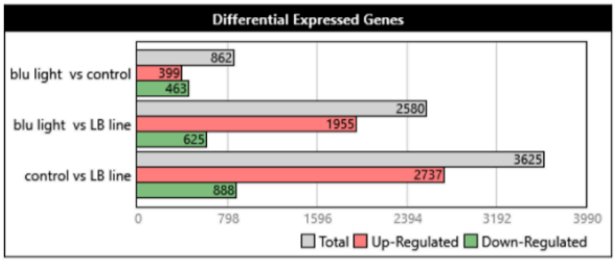

Fig.11 | A) PCA plot of samples highlighted with color code: red = 72A, blue = Melan-a blue light exposure for 72 consecutive hours, and purple = control Melan-a. B) Summary table of comparisons with gene counts for each comparison, and a graph of differentially expressed genes with color code: grey = Total, salmon = UP-regulated, and green = DOWN-regulated.

Then, the differentially expressed genes from the comparisons among the three cell lines were grouped by hierarchical clustering and depicted via heatmap *(Fig.12)*.

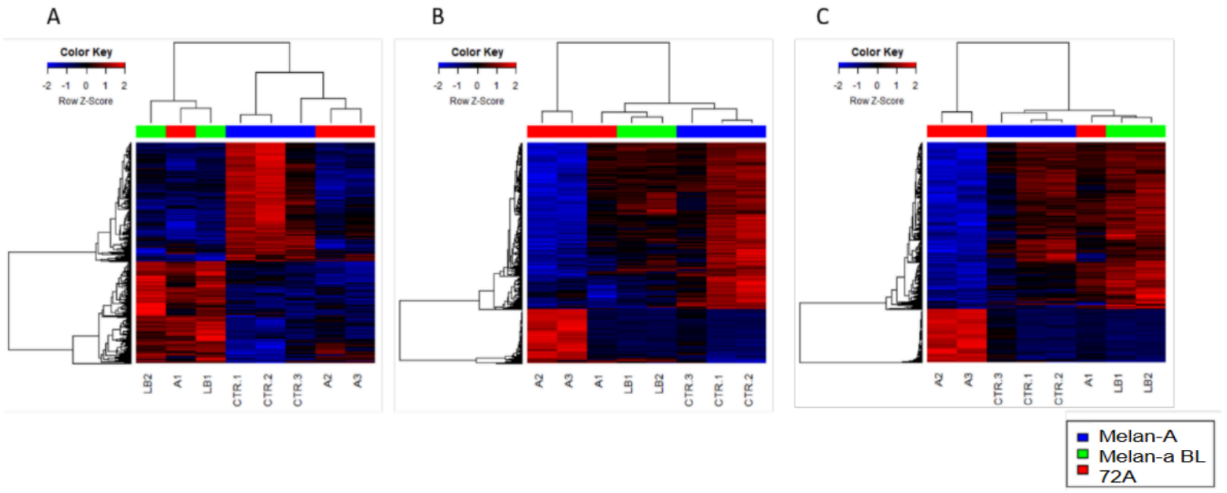

Fig.12 | Gene expression profiles of Melan-a, Melan-a exposed to BL for 72h, and 72A cell lines were evaluated using Significance Analysis of Microarrays (SAM), and the expression values of significant genes were grouped by hierarchical clustering. Expression values are reported on a color scale (blue = below average expression, red = above average expression, black = average expression; intensity correlates with distance from the mean). Bars above the dendrogram show the analyzed cell lines with color code: Melan-a = blue, Melan-a exposed to blue light for 72h = green, 72A = red.

Gene enrichment analysis of the differentially expressed genes across the three distinct comparisons, revealed that these genes are significantly enriched in key pathways regulating DNA-damage responses, cell cycle and DNA replication *(Fig.13 A,B)* .

The hierarchical clustering of the gene expression of DNA repair genes across the three gene lists *(Fig.14)* revealed a significant overlap among the differentially expressed genes across the three comparisons. The significantly enriched terms were subsequently grouped using hierarchical clustering, and the term with the best p-value within each cluster was selected as the representative term to be visualized in a heatmap, where the color code is dictated by the p-value.

A

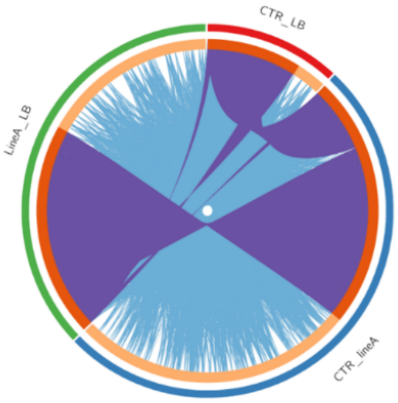

B

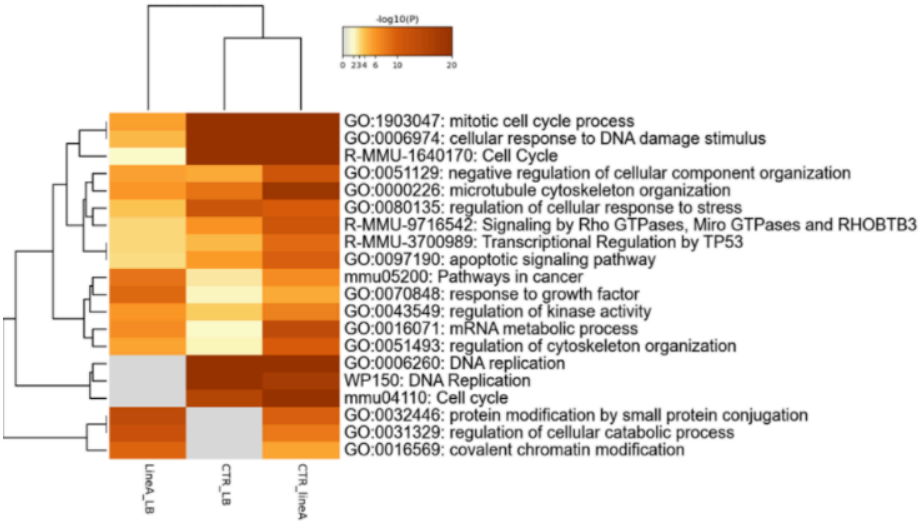

Fig.13 | A) The Circos plot illustrates the overlap among the differentially expressed gene lists from the three compared groups. On the outer layer, each arc represents the identity of each gene list, using the following color code: blue = differentially expressed genes between the control line and the wash-out line obtained immediately after 72h blue light exposure; red = differentially expressed genes between the control line and the line exposed to 72h blue light; and green = differentially expressed genes between the line exposed to 72h blue light and the wash-out line after 72h blue light exposure. On the inner layer, each arc represents a gene list, where each gene has a point on the arc. Dark orange indicates genes appearing in multiple lists, and light orange indicates genes unique to that gene list. Purple lines connect the same gene shared by multiple gene lists. Blue lines connect different genes that fall into the same ontological term (the term must be statistically significantly enriched). A greater number of purple connections and longer dark orange arcs imply higher overlap among gene lists. Blue connections indicate the amount of functional overlap between gene lists. B) Significant p-values of enriched terms were grouped by hierarchical clustering according to a color scale from yellow to red (increasing significance,

with grey indicating a lack of enrichment for that term in the corresponding gene list).

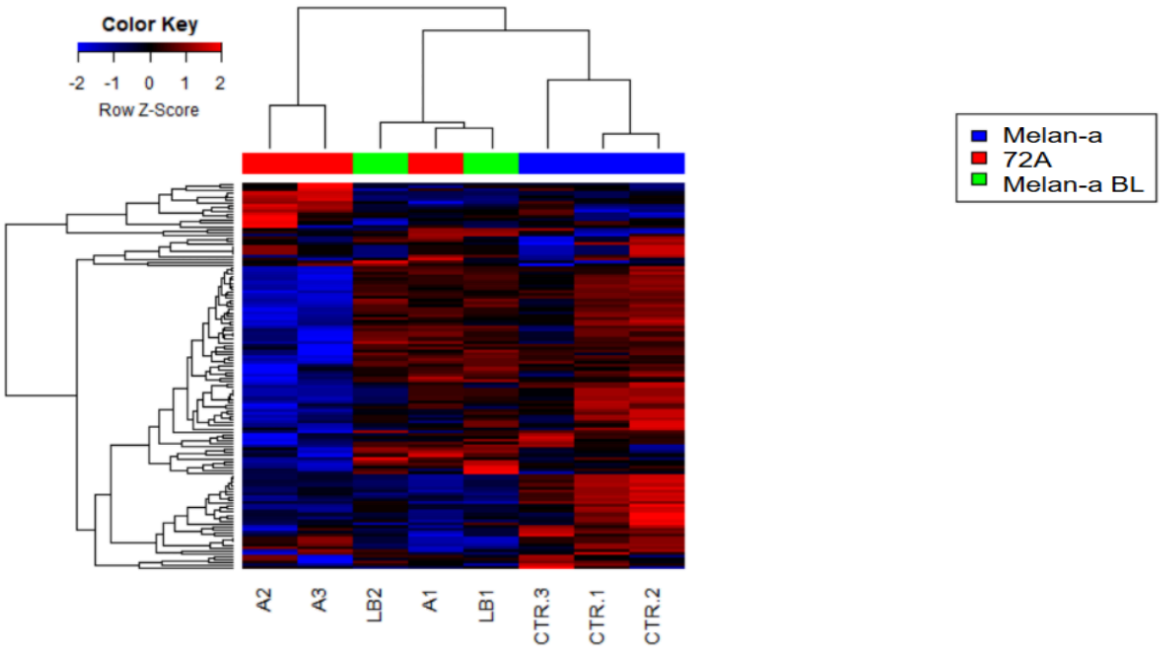

Fig.14 | Hierarchical clustering of DNA repair-related genes expression in the three gene lists.

The above result demonstrates that BL exposure has anti-proliferative, pro-apoptotic, and pro-oxidant effects. In order to clarify whether these effects were dependent on the specific experimental conditions in which the assays were carried out, the impact of BL exposure was evaluated on the C2 cells. This cell line derived from Melan-a (see Material and Methods section for detail).

As shown in *Fig.15A*, exposure to BL did not induce statistically significant differences ("ns") in proliferation between unexposed C2 cells (C2WT) and those exposed for 72 hours to BL (C2 WT Blue light). Similarly, both C2-WT cells and Blue Light-exposed C2 cells show a high percentage of alive cells (approximately 98%) and a low percentage of apoptotic cells (approximately 2%), suggesting that BL exposure does not induce apoptosis under these experimental conditions *(Fig.15 B)*.

A

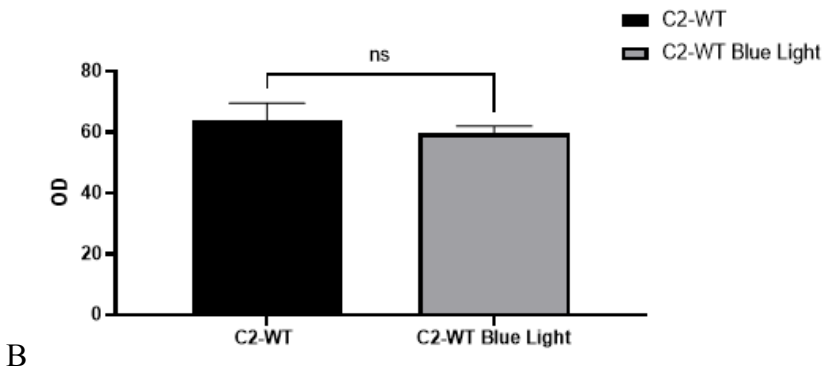

B

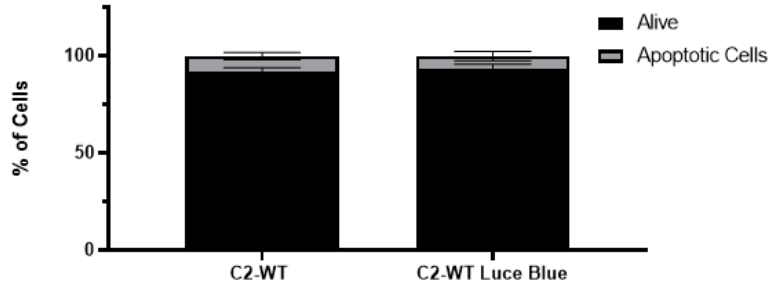

Fig.15 | Effects of Blue Light exposure on C2-WT cell proliferation (A) and apoptosis (B). (A) Bar graph illustrating Optical Density (OD) as a measure of proliferation for control C2-WT cells and C2-WT cells exposed to Blue Light. "ns" indicates no statistically significant difference. (B) Stacked bar graph displaying the percentage of alive and apoptotic cells in control C2-WT and Blue Light-exposed C2-WT cells. Data represent mean ± SEM.

1.4 BL mutational signature identification

In addition, to determine whether BL exposure of Melan-a cells could reproduce the mutational signature characteristic of UM, and thereby ascertain its potential role as an environmental etiological agent in UM tumorigenesis, a comprehensive analysis of mutational signatures was conducted.

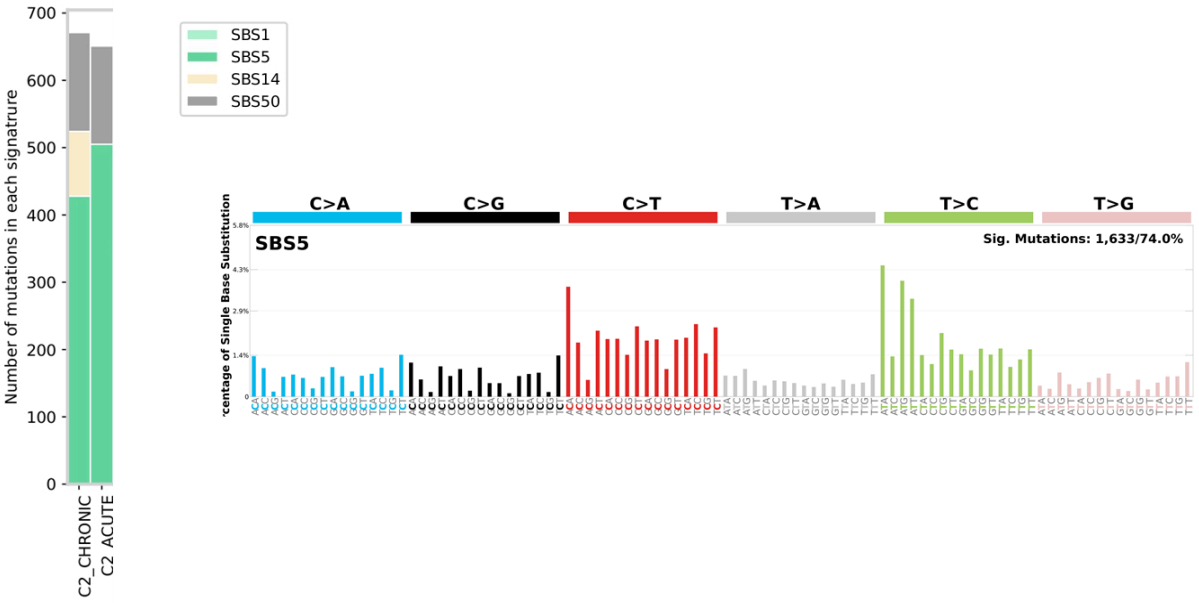

Fig.16 | Mutational signature in Melan-a cells following blue light exposure: highlights the predominance of single base substitution (SBS) SBS1 and SBS5, and a detailed SBS5 profile. C2_chronic=C2 cell line that survived 72 hours of consecutive exposure to BL, stable in culture; C2_acute= C2 cells utilized right after 72 hours of consecutive exposure to BL.

A comparative analysis of mutational signatures was conducted, considering the composition of single base substitution (SBS) signatures extracted from published studies on UM[87], and the mutational signature obtained by exposing Melan-a cells to BL considering only variants that were predicted by at least two different detection methods (Strelka, Varscan2, Mutect2) and not shared between samples (*Fig.16*).

The left section presents a stacked bar graph quantifying the "Number of mutations in each signature" for "C2_CHRONIC" and "C2_ACUTE" samples. This analysis highlights the predominance of SBS1 and SBS5 signatures, with minor contributions from SBS14 and SBS50. Concurrently, the right section provides a detailed profile of single base substitutions for the SBS5 signature, representing a specific pattern of induced mutations and contributing 1,633 significant mutations, which constitute 74.0% of the total. So, the exposure of Melan-a cells to blue light generated a distinct mutational signature, primarily characterized by SBS1 and SBS5, signatures known to be present in uveal melanoma (UM) and visible in the upper reference panel. It is crucial to note the absence of the predominant cutaneous melanoma (CM) signatures, namely SBS7a and SBS7b, which are typical of UV radiation exposure but are not present in the UM profile nor in the blue light-induced signature.

2. ***Development and Characterization of Complex Carcinogenesis Models***

A further aim of the PhD program was the development of new cellular models of UM carcinogenesis. Since metastatic progression is promoted by functional inactivation of the tumor suppressor gene BAP1[37], BAP1 KO cells are considered the best *in vitro* model for studying metastatic progression in UM. However, although several research groups have failed to create isogenic BAP1-knockout uveal melanoma lines, in collaboration with Michael Zeschnigk (University Hospital Essen, Institute of Human Genetics), a BAP1-KO cell line was successfully generated in the human UM line 92.1. This cell line is characterized by a near tetraploid profile, which may have contributed to the success of the editing process (unpublished data). Consequently, BAP1 editing *via* CRISPR/Cas9 could only be performed on the cell line already edited for the $GNA11^{Q209L}$ gene. Therefore, through this approach, a $GNA11^{Q209L}$ knock-in (KI) and $GNA11^{Q209L}$-BAP1 knockout ($GNA11^{Q209L}$-BAP1 -/-) cell model of UM was developed.

3. ***Identification and Functional Validation of Novel 8q Biomarkers***

The third aim of this thesis was to identify and validate novel prognostic biomarkers within Chromosome 8q. The ultimate goal was to pinpoint genes critical for metastasis formation and identifying potential targets for more effective therapeutic strategies.

Considering that MYC did not exhibit differential expression with 8q gain, its amplification is generally not the primary driver or a highly recurrent event within this gain in UM[41], and ASAP1, though a well-established marker, did not fully explain the increased metastatic risk, the definition of the 8q gene panel was initiated. For this purpose, ASAP1 was subsequently utilized as a reference gene from literature[88].

3.1. Identification

To investigate the association between chromosome 8q amplification and poor prognosis, four cohorts of UM patients (n = 341)[89] were utilized, considering metastatic disease as the survival outcome. From these, information on the presence of 8q gain and follow-up data was available for 285 cases. In this dataset, the presence of the 8q amplification (n = 181) was associated with a significantly decreased survival: 32 months versus 70 months (Kaplan-Meier analysis, *Fig.17*). This analysis further demonstrated that 8q amplification is associated with a higher risk of metastasis development (OR = 6.74 [3.74–12.13], p = 1.4516E-11) and is capable of increasing

the relative risk of metastasis, even when considering other factors such as monosomy 3 and BAP1 mutations. The detrimental effect of 8q gain on prognosis was also observed in independent datasets, which confirmed its specific association with BAP1-mutated tumors and its lack of prognostic impact in SF3B1-mutated tumors[90].

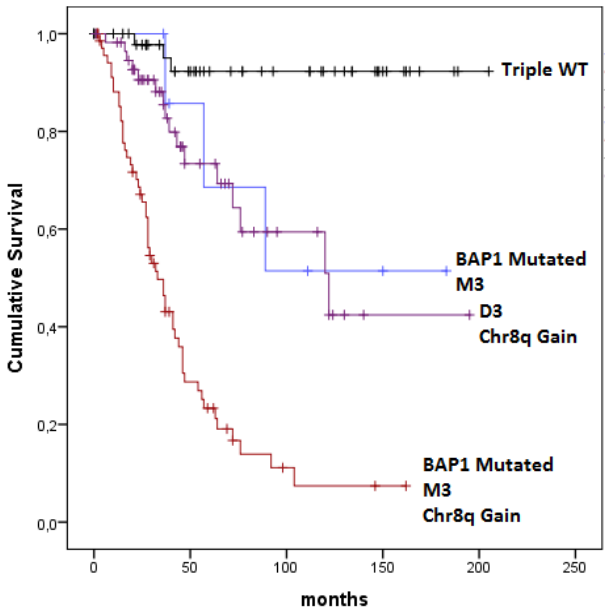

Fig.17 | Kaplan-Meier survival curves on Cox-type multiple regression models for known prognostic factors on primary UM. Triple WT= Disomy Chr3, 8 and BAP1 WT; M3= Chromosome 3 monosomy; D3= Chromosome 3 disomy. Chromosome 8q amplification (Chr8q Gain) contributes to rapid progression to death from metastatic disease. (Rossi et al., 2021).

Furthermore, SAM analysis performed comparing the gene expression profiles of 8q amplified and disomic samples (n = 255) allowed to identify differentially expressed genes. Specifically, 143 genes were found to be differentially expressed in a statistically significant manner among patients disomic for chromosome 3, with or without 8q region amplification *(Fig. 18A),* thus excluding the confounding effect of monosomy 3. Patients with 8q gain were found to show poorer overall survival (*Fig. 18B).*

A

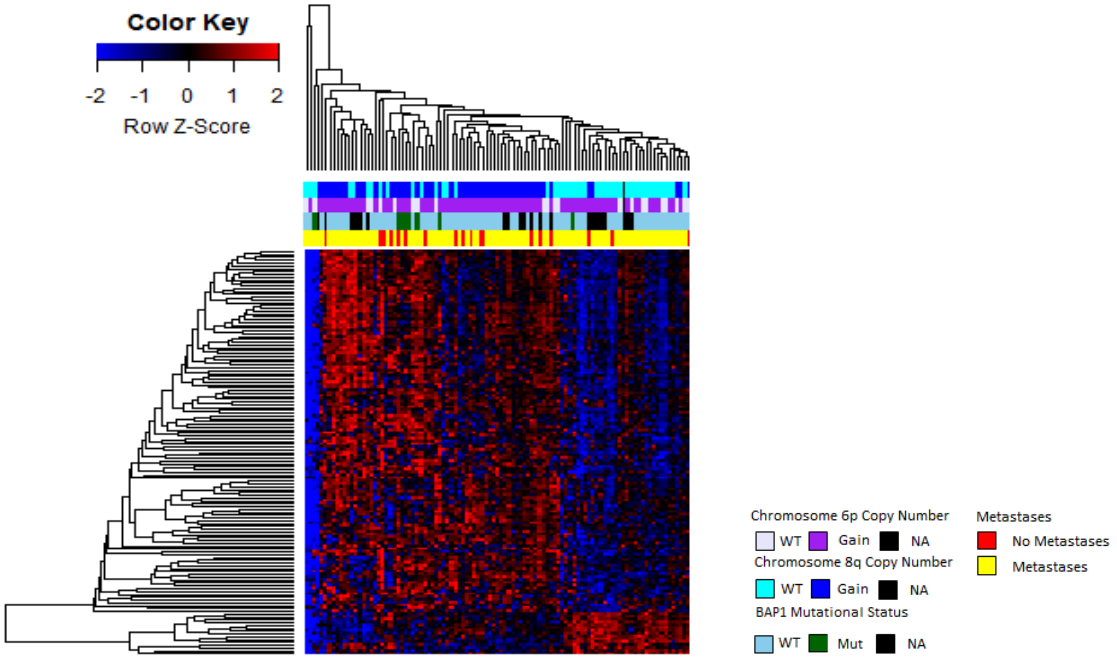

B

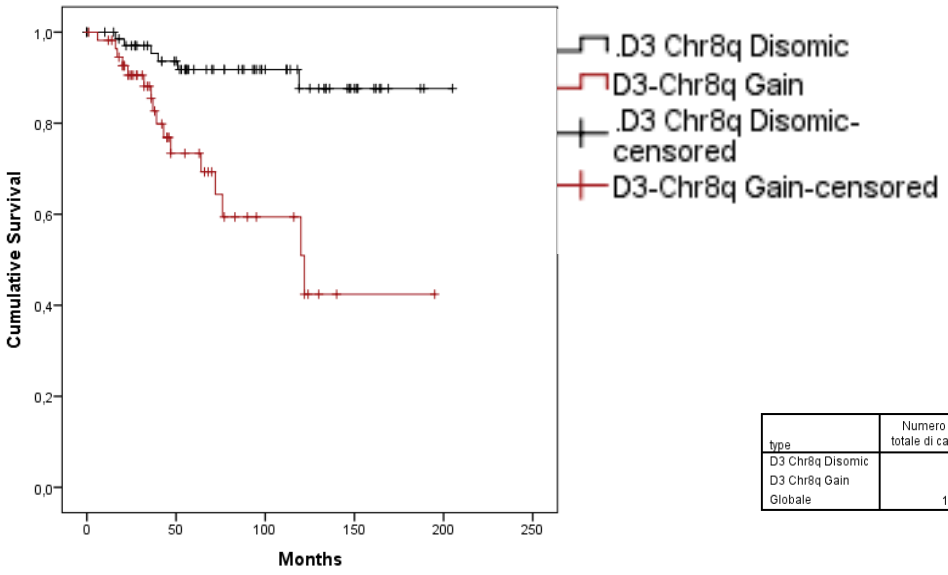

type	Numero totale di casi	N di eventi	Con censura	
			N	Percentuale
D3 Chr8q Disomic	73	6	67	91,8%
D3 Chr8q Gain	57	16	41	71,9%
Globale	130	22	108	83,1%

Fig.18 | (A) Heatmap of gene expression levels based on mutational status and 8q in the UM. Expression profiles of patients dysomic for chromosome 3, with or without amplification of 8q were compared by SAM (Significance Analysis Microarrays) and clustered by hierarchical clustering. Two clusters can be seen, one of which is enriched in patients with 8q gain (first colour bar above, in blue, right). The expression values are represented with a color scale: red (above the mean), blue (below the mean), black (at the level of the mean). The bars above the

heatmap represent the status of chromosome 8q, 6p, presence of mutations on BAP1 and development of metastases, respectively. No-information (NA) cases are shown in black. (B) Kaplan-Meier survival curves on a Cox linear regression model based on the status of chromosome 8q (Chr8q) in primary UM tumours with two copies of chromosome 3 (Disomy 3 or D3). Cases with chromosome 8q amplification (Chr8q gain) show a more rapid progression to disease death. (contribution of Amaro A. and Reggiani F.)

The expression of these 143 genes was also studied in UM cell lines to exclude genes expressed solely by non-tumor infiltrating cells. High gene expression levels were observed in this context as well, confirming a predominant role of melanoma cells over the infiltrate in the expression of these genes *(Fig 19)*.

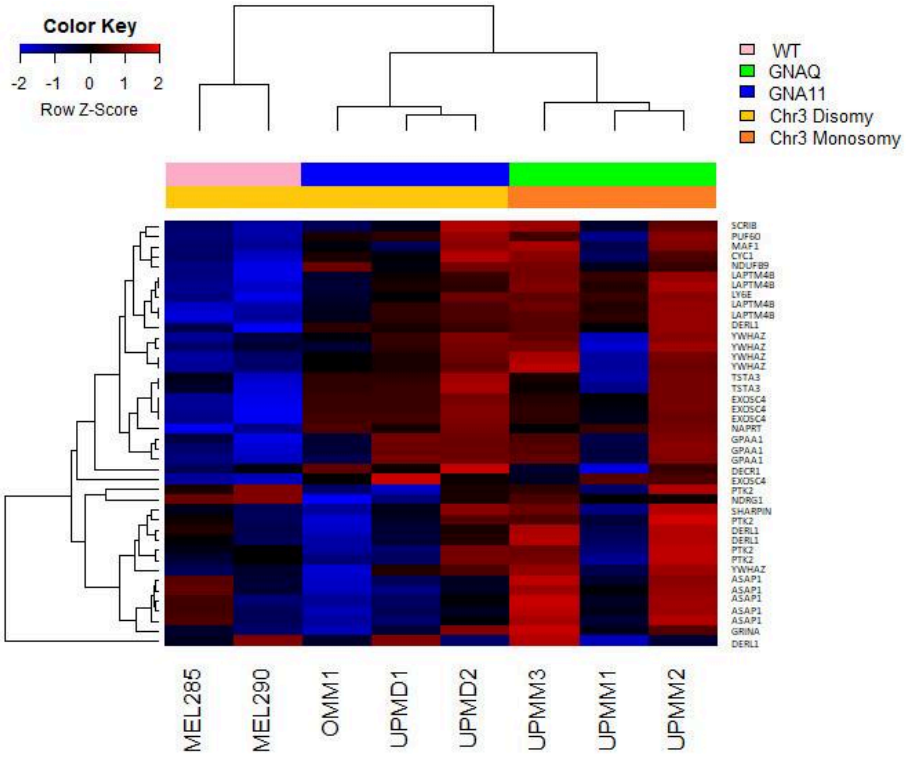

Fig.19 | Gene expression analysis on 19 markers on expression arrays of UM cell lines. The samples were classified by hierarchical clustering, the colour of the cells corresponding to values above (red), below (blue) or equal to the mean (black). The bars below the dendrogram represent the mutational status of GNAQ, GNA11 and the status of chromosome 3, respectively.

Then, to validate the association between the expression of these genes and an increased copy number of regions on chromosome 8, Pearson's correlation was calculated using samples from the TCGA UM dataset. Additionally, genes with a significant association between copy number

alterations (CNA) and gene expression have been identified using two R packages, CNVranger[91] and iGC[92]. *(Fig. 20)*

In total, 19 genes (EXOSC4, PUF60, NAPRT1, LAPTM4B, DERL1, DECR1, ASAP1, NDUFB9, PTK2, YWHAZ, CYC1, GPAA1, GRINA, TSTA3, SHARPIN, LY6E, MAF1, SCRIB, NDRG1) on chromosome 8q were selected based on Pearson's correlation and the association between CNA and gene expression calculated by CNVranger and iGC *(Fig. 20B)*.

A

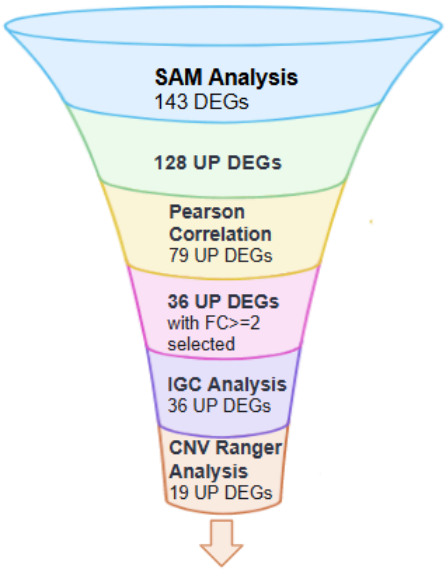

19 upregulated and differentially expressed genes (FC>=2) on chromosome 8q; a subset of **8 genes** is considered for further analysis.

B

Fig.20 | (A) Summary of the process of analysis that led to the selection of a set of genes on Chr8 whose higher expression correlated with an amplification of 8q,(B) Location of the 19 candidate genes on chromosome 8q (reference hg19), selected by bioinformatic analysis, as described in the

preliminary data. Shown in red are the CNAs present in the dataset of TCGA patients with uveal melanoma[16].

This final number was narrowed down to 8 target genes considering the antibodies availability and other factors such as gene expression, 8q gain/metastasis AUC, survival, gene mean methylation on the UM dataset, being a druggable target (PTK2[93]) and publications related to their roles in different tumors (*Fig. 21*).

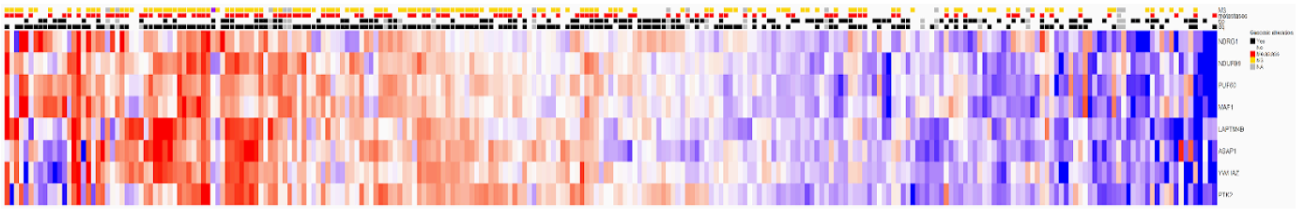

Fig.21 | Expression of the 8 gene targets on the UM dataset: Patients are annotated with four color bars on the top of the plot, the first represents M3 presence (in yellow), the second metastasis development during follow-up (in red), followed by 6p and 8q gain (in black). Heatmap colors are based on gene expression (red over the mean, blue under the mean, white near zero).

Following the selection of target genes for chromosome 8q, an initial scRNA-seq analysis was conducted utilizing public datasets *(Fig.22) via* an Rstudio script and exploration of the Tumor Immune Single-cell Hub2 (TISCH2) database. The expression of these target genes, both individually and as an entire gene signature, was assessed across and through comparison of the four datasets. An initial spatial overview of the distribution of cells of interest within the datasets was obtained through a UMAP (Uniform Manifold Approximation and Projection) plot, which provides a two-dimensional representation of high-dimensional gene expression data. Notably, target genes associated with 8q gain were predominantly represented within the same cluster of malignant cells. This suggests that these cells likely share gene expression profiles characteristic of malignant cells, thereby supporting the hypothesis of a direct correlation between cells with Chr8q gain and tumor progression leading to metastasis development *(Fig.23)*.

	ID	Dataset Name	Species	Treatment	Patients	Cells	Platform	Pri / Meta	PMID
☑	T010081	UVM_GSE139829	Human	None	11	103,703	10x Genomics	Primary, Metastatic	31980621
☑	T020187	UVM_GSE138433	Human	None	6	12,682	10x Genomics	Primary	33462406
☑	T020188	UVM_GSE160883	Human	None	6	12,977	inDrop	Primary	34518527
☑	T020189	UVM_GSE169609	Human	None	2	17,524	10x Genomics	Primary	33811047

Fig.22 | Public dataset used.

Fig.23 | UMAP plot derived from the Harbour dataset. Panels 1-3 illustrate ASAP1 as a representative target gene, which was utilized for FISH analysis. Panel 4 displays the entire gene signature.

3.2. Functional Validation

Subsequent experimental validation was then undertaken to elucidate the interactions of the target genes with the tumor microenvironment (TME) and their contribution to metastasis development, thereby aiming to confirm the observations derived from the bioinformatic approach.

Primary UM samples utilized were accompanied by comprehensive patient clinical data, which is fundamental for verifying whether the presence of Chr8q amplification in the primary tumor correlates with metastatic progression.

To avoid the presence of false positive signals when analysing UM samples, the optimization of antibody concentrations was a crucial step. It was performed on kidney (NDRG1, LAPTM4B, NDUFB9, YWHAZ, MAF1, PTK2), and colon (PUF60, ASAP1) tissue *(Fig.24)*. The tissue

selection was performed considering the documented positive protein expression of the relative chosen genes in the public database The Human Protein Atlas.

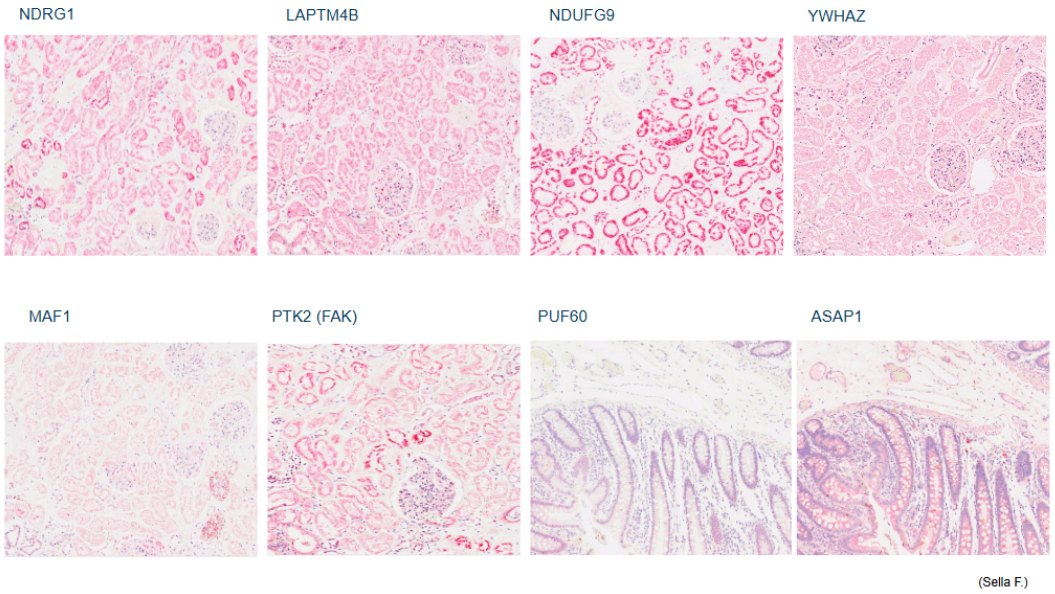

Fig.24 | Optimized Abs concentrations on relative control tissue.

Once concentrations were optimized, the IHC analysis was initiated on a cohort of 45 primary UM (3 from USZ and 42 from the Karolinska Institute) for the 8 target genes.

To ensure the quality and suitability of all UM samples, routine Hematoxylin and Eosin (H&E) staining was performed. This preliminary assessment proved particularly instrumental in confirming the quality of older samples, which in turn informed decisions regarding sample inclusion or exclusion *(Fig.25)*.

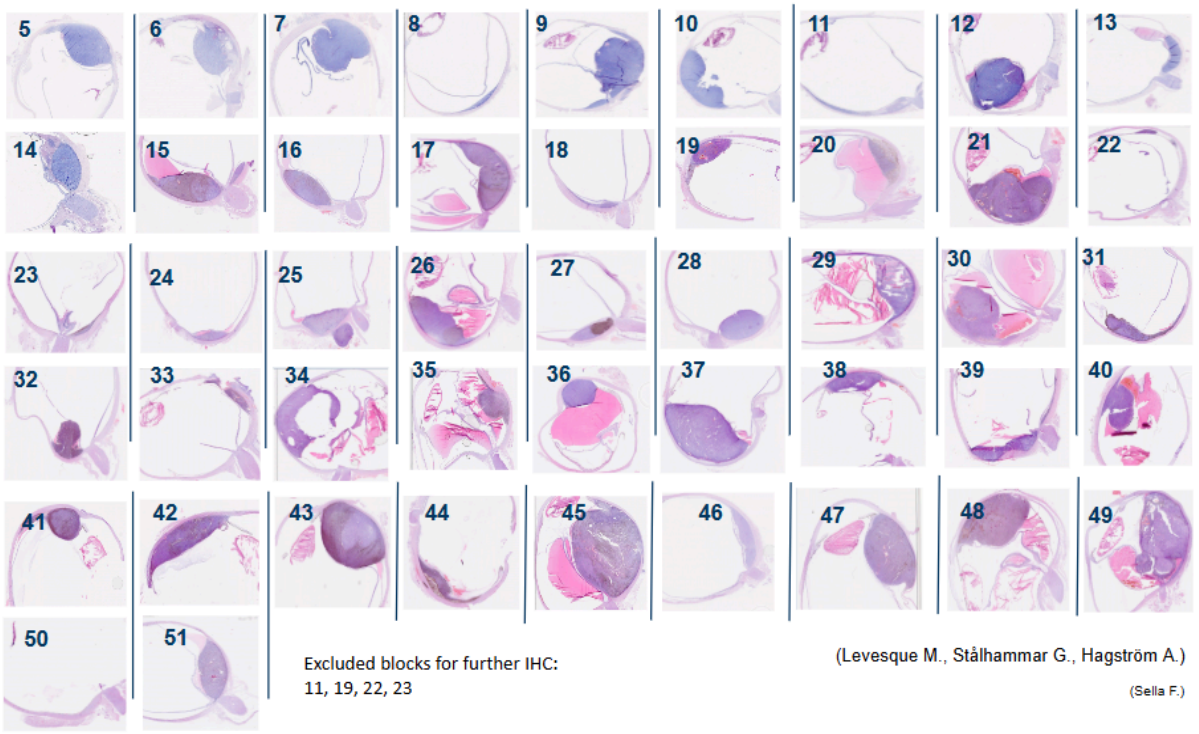

Fig.25 | Quality assessment of UM samples via preliminary Hematoxylin and Eosin (H&E) staining. Representative images from a subset of the cohort (specifically, samples from the Karolinska Institute) are displayed following H&E staining. This preliminary evaluation facilitated the identification and exclusion of 4 suboptimal tissue blocks from this specific cohort, resulting in a final set of 42 samples deemed suitable for further analysis. The same quality control procedure was subsequently applied to the USZ cohort, leading to the selection of 3 out of 9 originally chosen samples (Eye1, Eye 2, and Eye 4).

Additionally, the H&E staining facilitated a more accurate verification of critical anatomical structures within the specimens. Such features included detached retina (caused by 10% formalin shrinkage or the presence of transudate typically appearing pink), and the characteristic mushroom-shaped tumor morphology *(Fig.26)*.

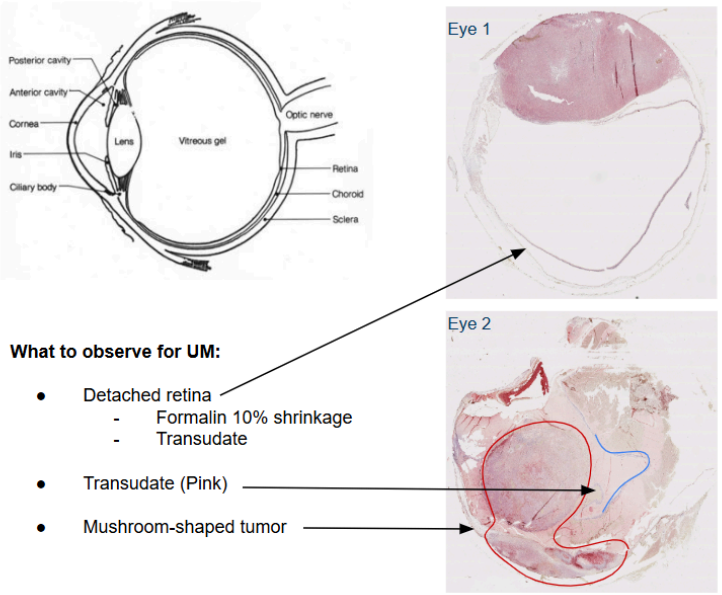

Fig.26 | Anatomical and histological structures of UM. Representative examples from 'Eye 1' and 'Eye 2' are depicted. It should be noted that the presence of all features varies across individual samples.

When developing the most appropriate staining conditions, determining the amount of antibody required to achieve satisfactory staining of UM samples posed a significant challenge due to the high intrinsic melanin content of the samples *(Fig.27A)*. Indeed, although qualitative differences in staining were evident, confirming the proper Abs concentration optimization, the high amount of melanin systematically interfered with signal detection and quantification by QuPath software. Indeed, because this software relies on a red scale for intensity, the natural brown color of melanin was invariably interpreted as a dark red signal, thereby leading to erroneous detection as positive staining and precluding accurate measurement of true antibody binding. Therefore, to overcome this technical limitation, the slides, before being labeled with antibodies, were subjected to a bleaching procedure[94–96] using a 1%KOH + 3% H_2O_2 solution *(Fig.27B)*. This procedure proved effective in significantly attenuating the interference caused by melanin, thus allowing for accurate quantitative analysis of antibody staining *via* QuPath. *(Fig.27C)*

A

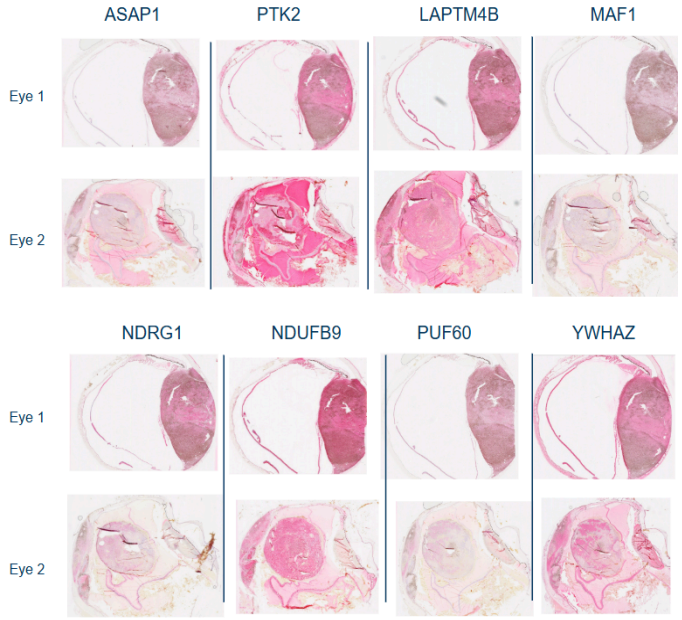
ASAP1
PTK2
LAPTM4B
MAF1
Eye 1
Eye 2
NDRG1
NDUFB9
PUF60
YWHAZ
Eye 1
Eye 2

B

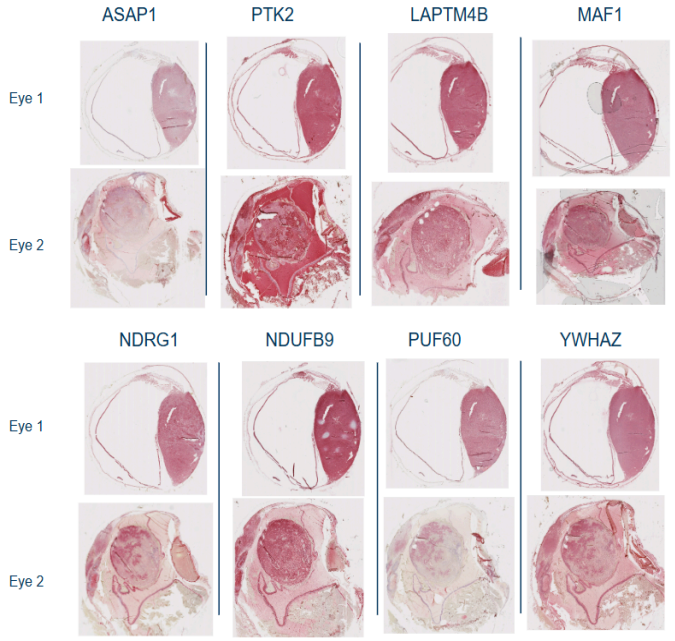
ASAP1
PTK2
LAPTM4B
MAF1
Eye 1
Eye 2
NDRG1
NDUFB9
PUF60
YWHAZ
Eye 1
Eye 2

C

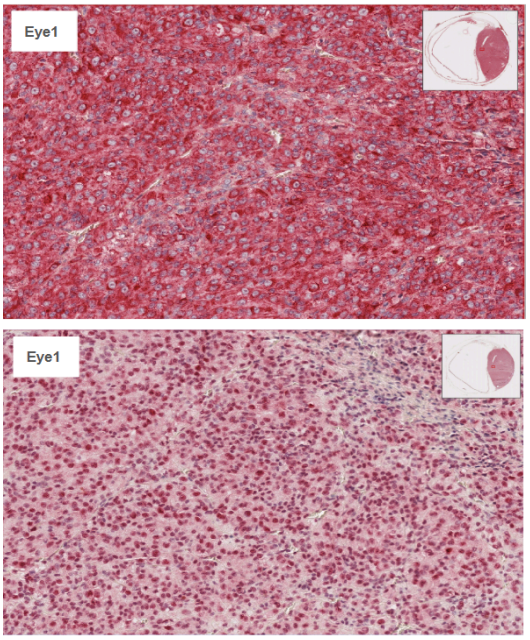

Fig.27 | Impact of bleaching on UM tissue pigmentation. (A) Untreated UM samples (pre-bleaching). (B) The same samples after bleaching treatment, showing melanin removal. (C) Staining specificity, with the absence of melanin allowing for visible subcellular antibody localization (cytoplasm -up, and nucleus- down).

Following the standardization of the staining protocol, slides were prepared utilizing all available samples. To optimize both processing time and material consumption, three patient samples were meticulously arranged per slide. This arrangement involved the precise microdissection of the tumor from the original 3µm section using a surgical blade. Subsequently, stainings *(Appendix images)*, and QuPath analysis were performed.

The graphs reported in *Figure 28* illustrate the total positivity percentages of target antibody staining (y-axis) for each eye (x-axis).

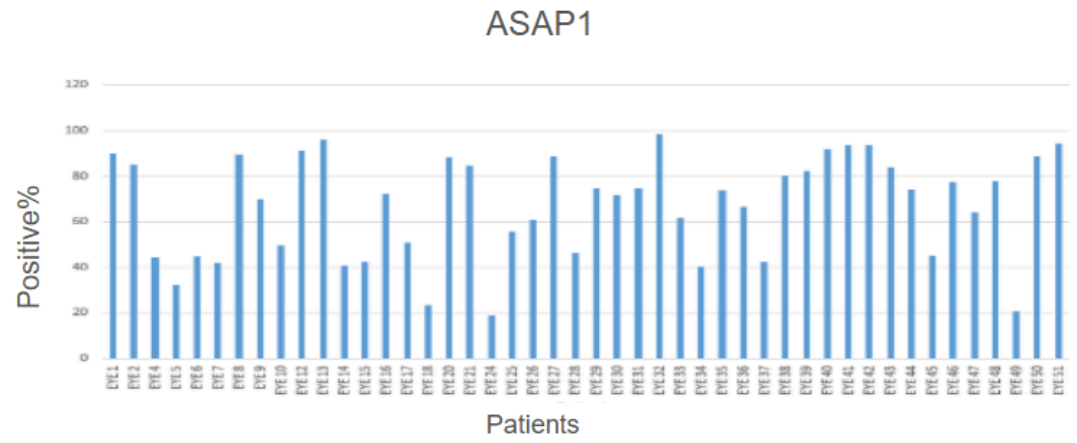
ASAP1
Positive%
120
100
80
60
40
20
0
Patients

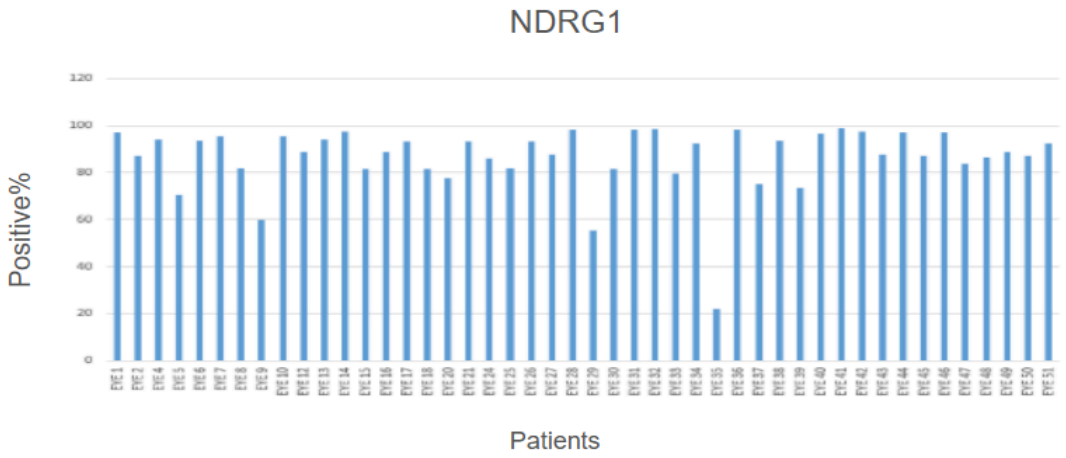
NDRG1
Positive%
120
100
80
60
40
20
0
Patients

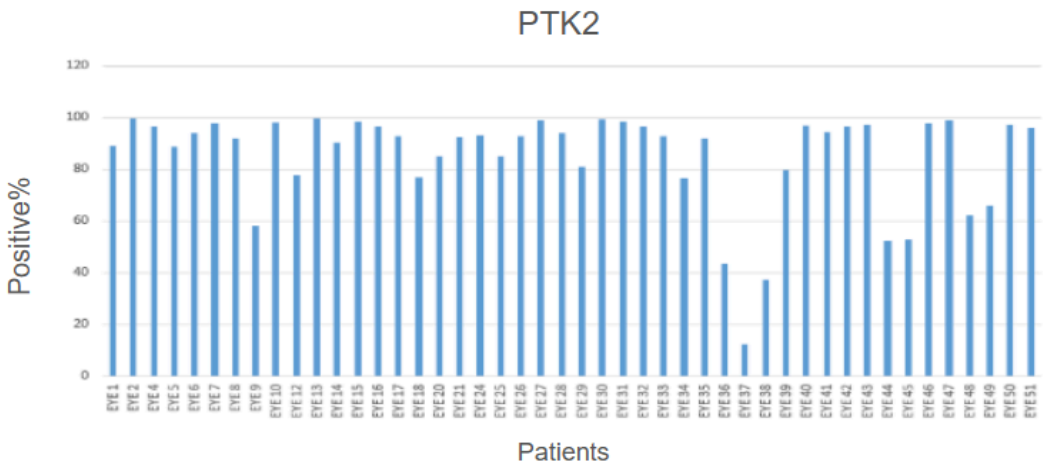
PTK2
Positive%
120
100
80
60
40
20
0
Patients

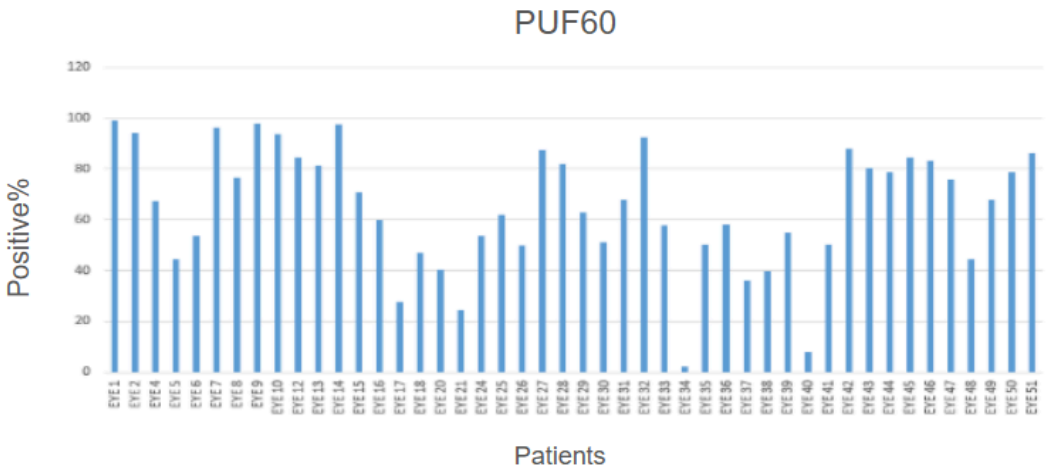
PUF60
Positive%
120
100
80
60
40
20
0
Patients

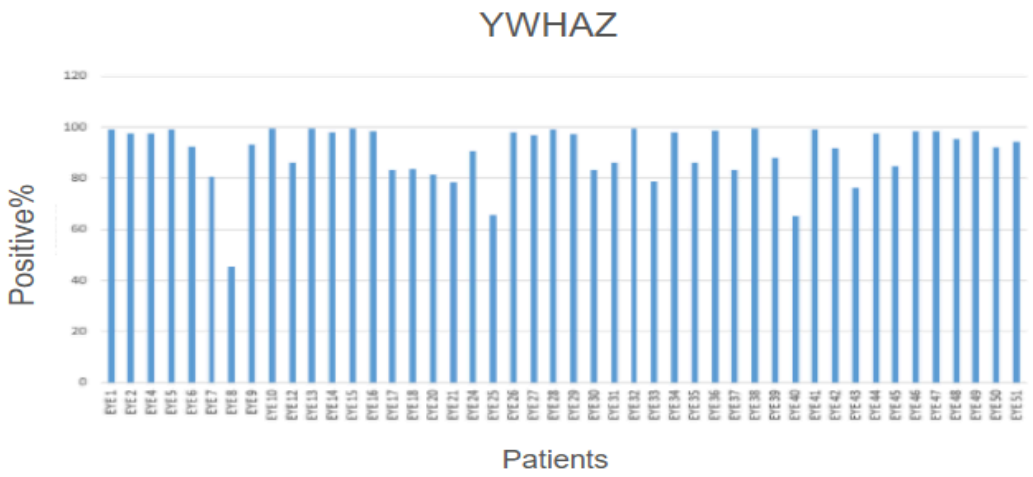
YWHAZ
Positive%
120
100
80
60
40
20
0
Patients

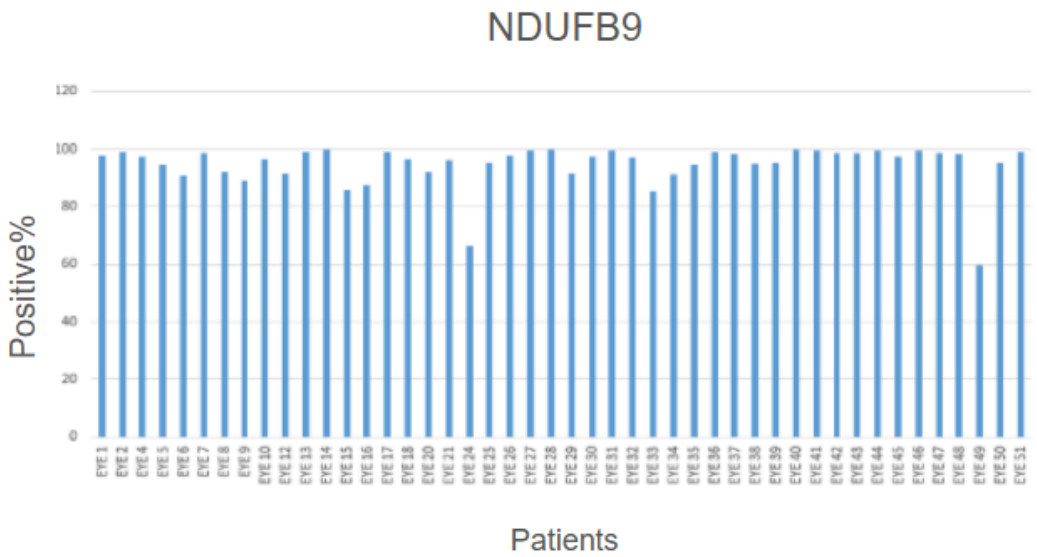
NDUFB9
Positive%
120
100
80
60
40
20
0
Patients

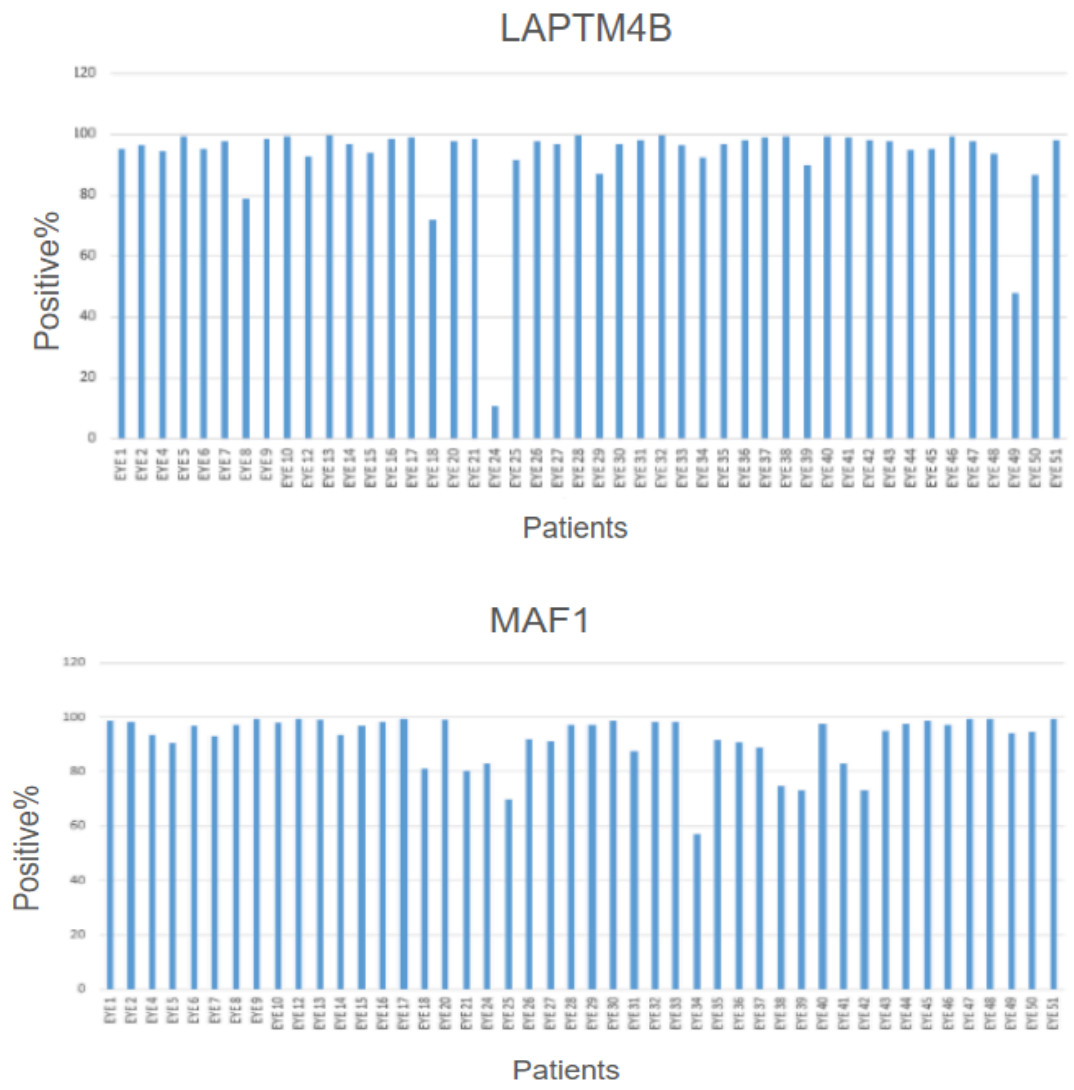

Fig.28 | Total Positivity Percentages of Target Antibody Staining in UM samples. Individual bar graphs display the total percentage of positivity (y-axis) for each investigated target antibody (x-axis) across specific patient samples (Eye 1-Eye 51), as determined by QuPath analysis.

Using detected ASAP1 positivity levels as a reference for other targets, in an initial analysis it was observed that the positivity levels for PTK2 and PUF60 is strictly comparable to those of ASAP1, while the expression patterns of the other targets exhibited higher overall positivity.

Notably, strong positive correlations were observed between ASAP1 and both LAPTM4B and NDUFB9, based on Pearson's coefficient analysis *(Fig.29)*. Since ASAP1 is already established as a surrogate marker of Chr8q amplification, these correlations suggest that LAPTM4B and NDUFB9 may not only be co-amplified with ASAP1, but also co-expressed in an amplification-driven manner. Indeed, higher expression levels than ASAP1 itself were observed

for these two genes in some patients, implying that they might not merely be passenger genes in the 8q region, but functionally relevant contributors to the metastatic phenotype. Consequently, their potential is highlighted as additional biomarkers of 8q gain and possibly more effective indicators of poor prognosis than ASAP1 alone. Observing the correlation scores between each target and ASAP1, this analysis suggests that each marker contributes distinct information, thereby enriching the overall dataset.

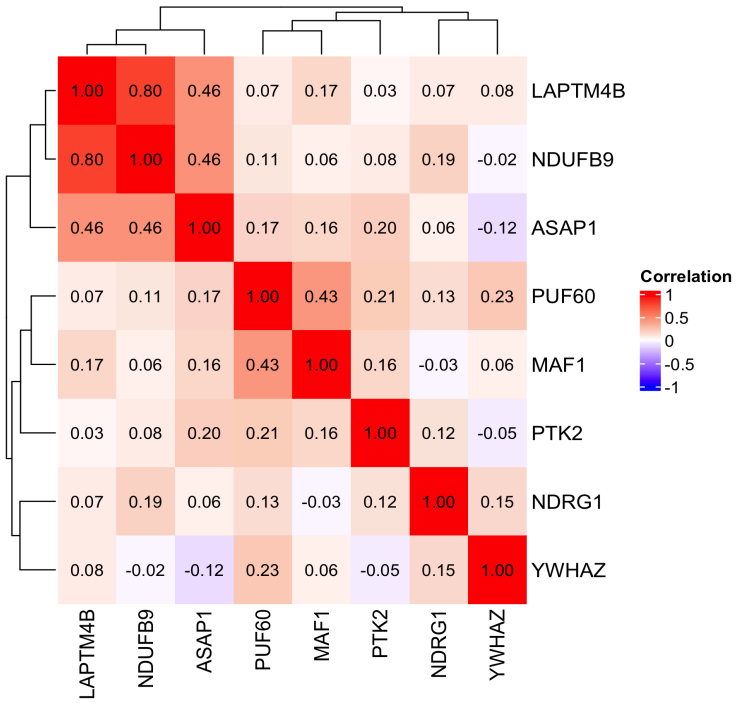

Fig.29 | Pearson correlation measures the strength of the linear relationship between two variables. It has a value between -1 to 1, with a value of -1 meaning a total negative linear correlation, 0 being no correlation, and + 1 meaning a total positive correlation. Positive correlations are observed between ASAP1 and both LAPTM4B (correlation coefficient: 0.46) and NDUFB9 (correlation coefficient: 0.46). These values, being positive and relatively high, support the described strong positive correlations.

Building on these findings, the expression intensity of all investigated markers was further explored through the analysis of IHC positivity thresholds (Num+1= low positivity, Num+2= medium positivity, Num+3= high positivity) *(Fig.30)*. For LAPTM4B and NDUFB9 specifically, it was consistently observed that the +3 positivity category represented the largest proportion of positive cells across individual patients. This proportion not only surpassed that of the +1 and +2

categories, but also consistently exceeded the intensity observed for ASAP1. This pattern suggests that these targets are not only strongly expressed, but may also exhibit greater amplification-sensitivity compared to ASAP1.

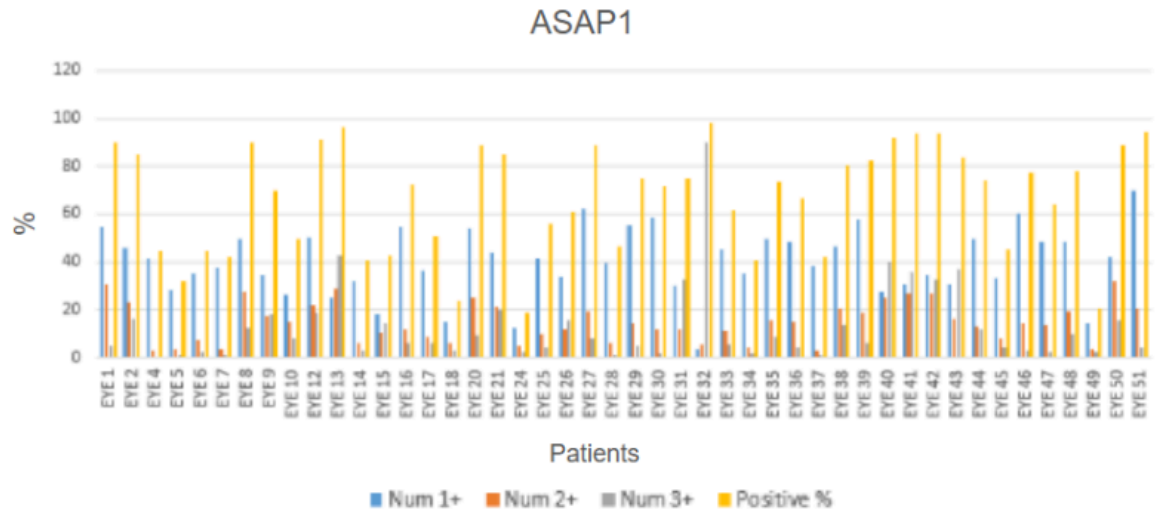

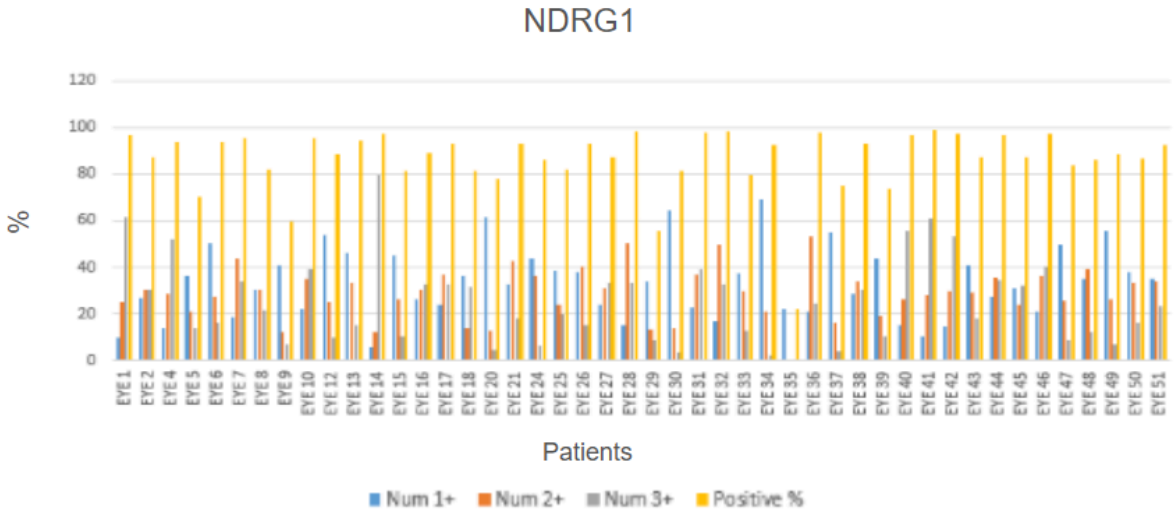

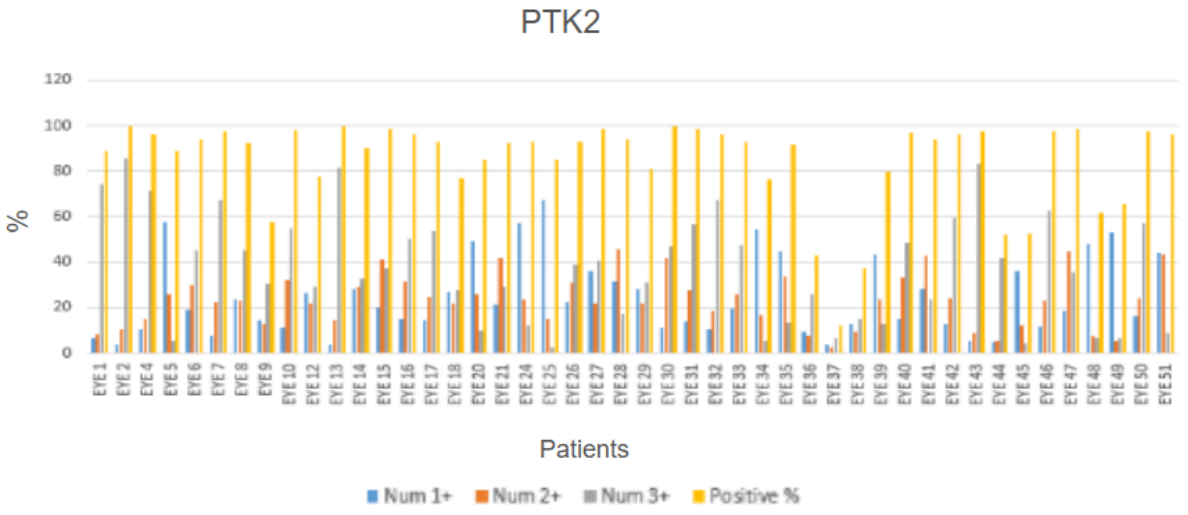
PTK2
120
100
80
60
40
20
0
%
EYE 1 EYE 2 EYE 4 EYE 5 EYE 6 EYE 7 EYE 8 EYE 9 EYE 10 EYE 12 EYE 13 EYE 14 EYE 15 EYE 16 EYE 17 EYE 18 EYE 20 EYE 21 EYE 24 EYE 25 EYE 26 EYE 27 EYE 28 EYE 29 EYE 30 EYE 31 EYE 32 EYE 33 EYE 34 EYE 35 EYE 36 EYE 37 EYE 38 EYE 39 EYE 40 EYE 41 EYE 42 EYE 43 EYE 44 EYE 45 EYE 46 EYE 47 EYE 48 EYE 49 EYE 50 EYE 51
Patients
Num 1+
Num 2+
Num 3+
Positive %

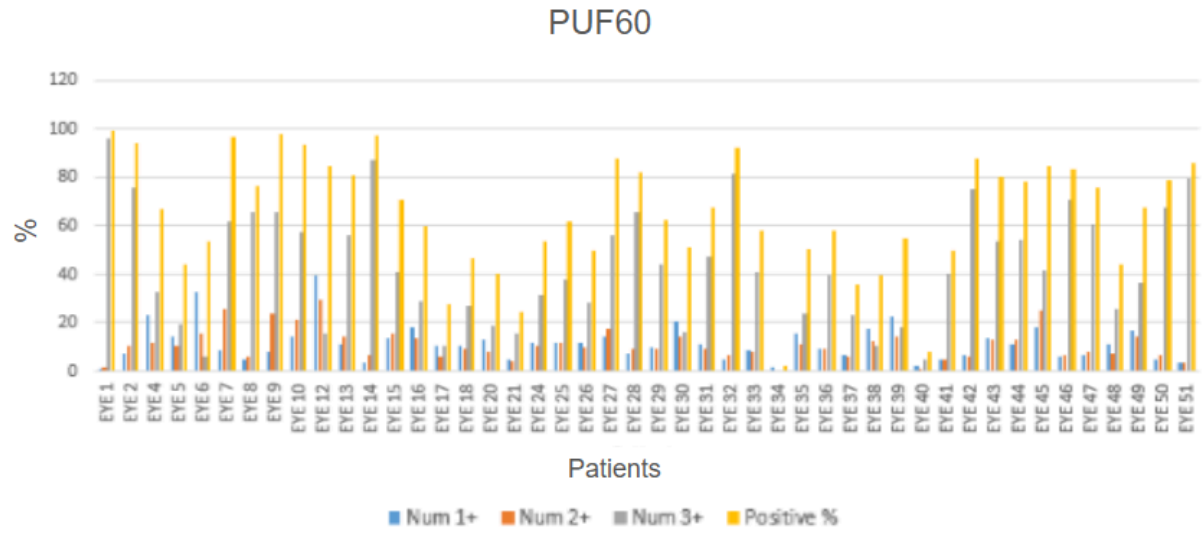
PUF60
120
100
80
60
40
20
0
%
EYE 1 EYE 2 EYE 4 EYE 5 EYE 6 EYE 7 EYE 8 EYE 9 EYE 10 EYE 12 EYE 13 EYE 14 EYE 15 EYE 16 EYE 17 EYE 18 EYE 20 EYE 21 EYE 24 EYE 25 EYE 26 EYE 27 EYE 28 EYE 29 EYE 30 EYE 31 EYE 32 EYE 33 EYE 34 EYE 35 EYE 36 EYE 37 EYE 38 EYE 39 EYE 40 EYE 41 EYE 42 EYE 43 EYE 44 EYE 45 EYE 46 EYE 47 EYE 48 EYE 49 EYE 50 EYE 51
Patients
Num 1+
Num 2+
Num 3+
Positive %

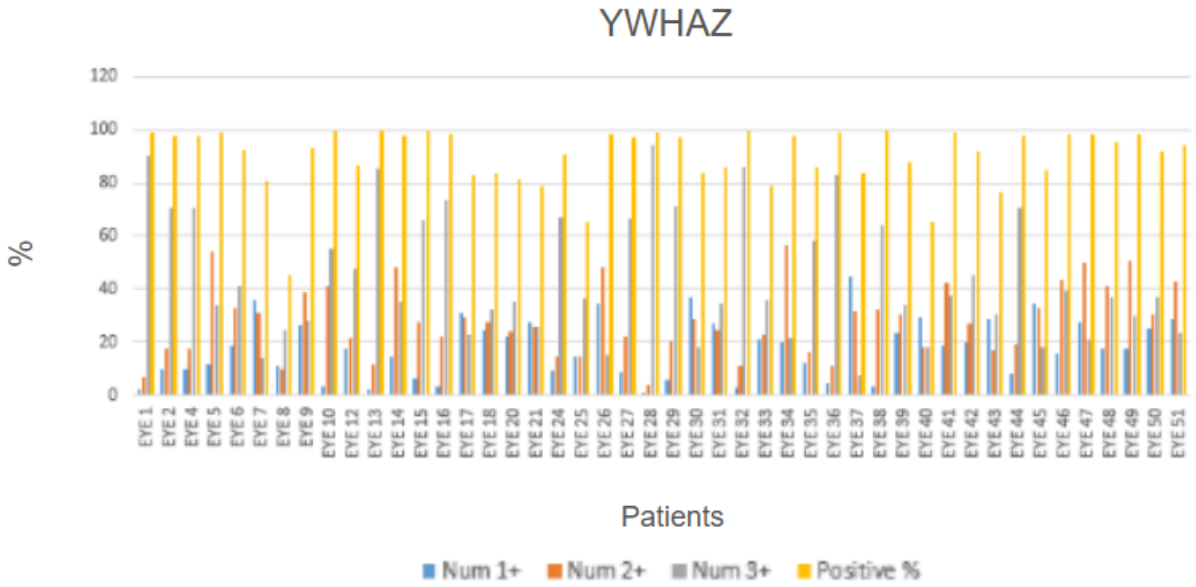
YWHAZ
120
100
80
60
40
20
0
%
EYE 1 EYE 2 EYE 4 EYE 5 EYE 6 EYE 7 EYE 8 EYE 9 EYE 10 EYE 12 EYE 13 EYE 14 EYE 15 EYE 16 EYE 17 EYE 18 EYE 20 EYE 21 EYE 24 EYE 25 EYE 26 EYE 27 EYE 28 EYE 29 EYE 30 EYE 31 EYE 32 EYE 33 EYE 34 EYE 35 EYE 36 EYE 37 EYE 38 EYE 39 EYE 40 EYE 41 EYE 42 EYE 43 EYE 44 EYE 45 EYE 46 EYE 47 EYE 48 EYE 49 EYE 50 EYE 51
Patients
Num 1+
Num 2+
Num 3+
Positive %

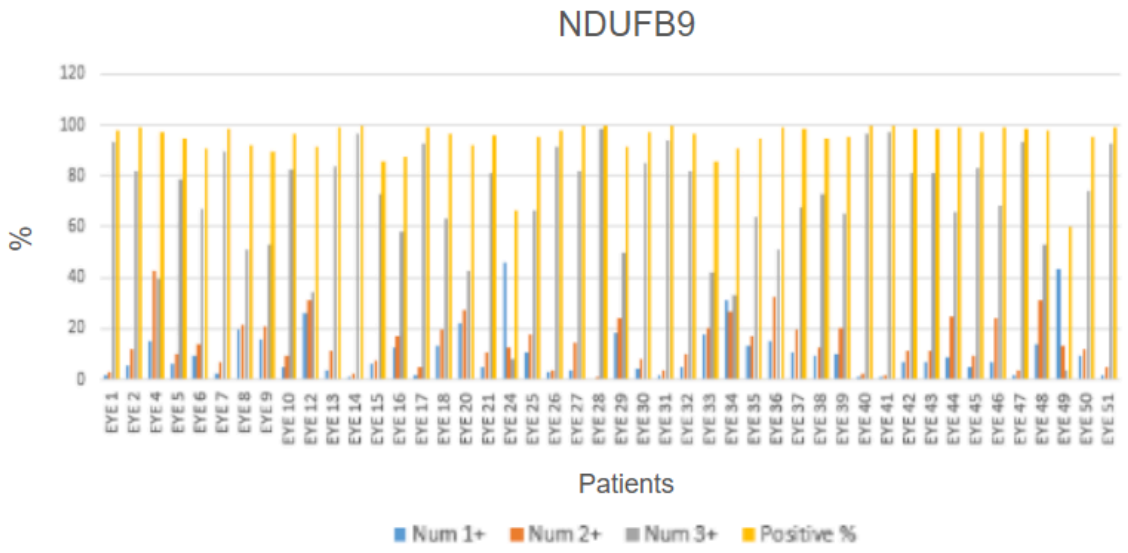
NDUFB9
120
100
80
60
40
20
0
%
EYE 1 EYE 2 EYE 4 EYE 5 EYE 6 EYE 7 EYE 8 EYE 9 EYE 10 EYE 12 EYE 13 EYE 14 EYE 15 EYE 16 EYE 17 EYE 18 EYE 20 EYE 21 EYE 24 EYE 25 EYE 26 EYE 27 EYE 28 EYE 29 EYE 30 EYE 31 EYE 32 EYE 33 EYE 34 EYE 35 EYE 36 EYE 37 EYE 38 EYE 39 EYE 40 EYE 41 EYE 42 EYE 43 EYE 44 EYE 45 EYE 46 EYE 47 EYE 48 EYE 49 EYE 50 EYE 51
Patients
Num 1+ Num 2+ Num 3+ Positive %

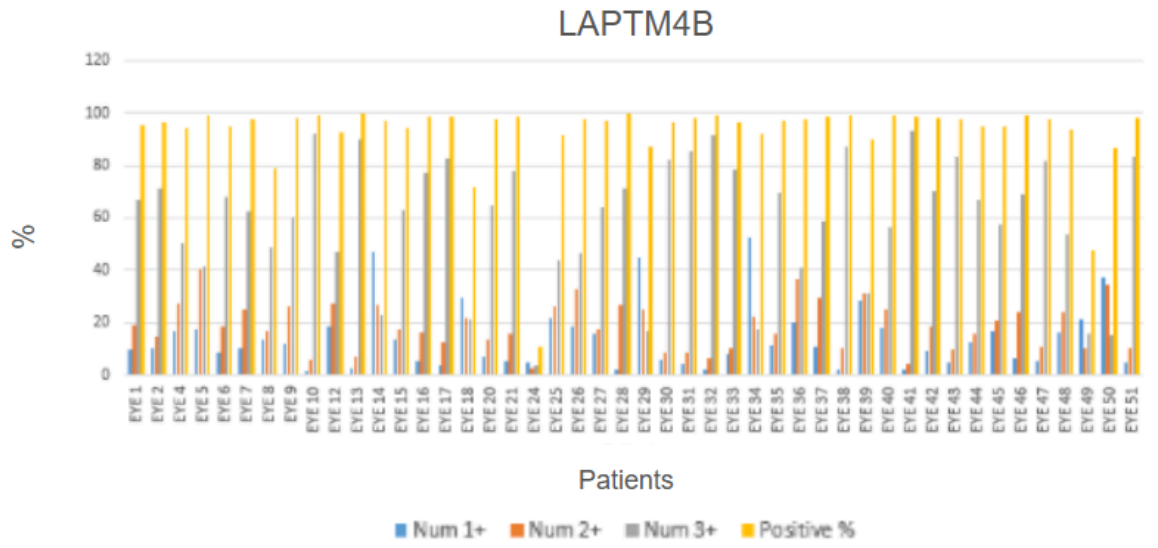
LAPTM4B
120
100
80
60
40
20
0
%
EYE 1 EYE 2 EYE 4 EYE 5 EYE 6 EYE 7 EYE 8 EYE 9 EYE 10 EYE 12 EYE 13 EYE 14 EYE 15 EYE 16 EYE 17 EYE 18 EYE 20 EYE 21 EYE 24 EYE 25 EYE 26 EYE 27 EYE 28 EYE 29 EYE 30 EYE 31 EYE 32 EYE 33 EYE 34 EYE 35 EYE 36 EYE 37 EYE 38 EYE 39 EYE 40 EYE 41 EYE 42 EYE 43 EYE 44 EYE 45 EYE 46 EYE 47 EYE 48 EYE 49 EYE 50 EYE 51
Patients
Num 1+ Num 2+ Num 3+ Positive %

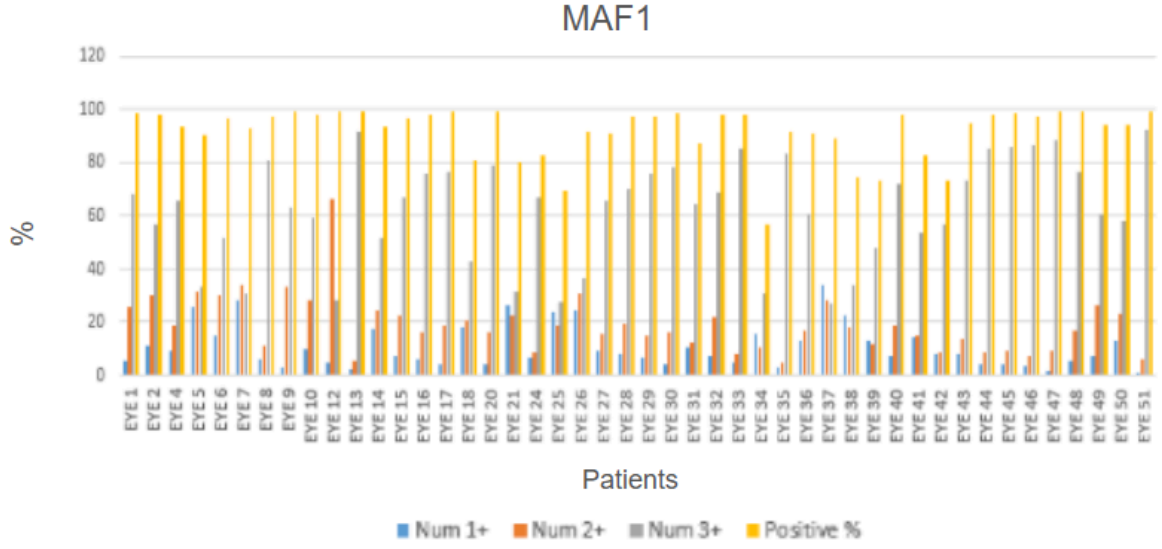
MAF1
120
100
80
60
40
20
0
%
EYE 1 EYE 2 EYE 4 EYE 5 EYE 6 EYE 7 EYE 8 EYE 9 EYE 10 EYE 12 EYE 13 EYE 14 EYE 15 EYE 16 EYE 17 EYE 18 EYE 20 EYE 21 EYE 24 EYE 25 EYE 26 EYE 27 EYE 28 EYE 29 EYE 30 EYE 31 EYE 32 EYE 33 EYE 34 EYE 35 EYE 36 EYE 37 EYE 38 EYE 39 EYE 40 EYE 41 EYE 42 EYE 43 EYE 44 EYE 45 EYE 46 EYE 47 EYE 48 EYE 49 EYE 50 EYE 51
Patients
Num 1+ Num 2+ Num 3+ Positive %

Fig.30 | Antibody Staining Positivity in UM samples: Total Percentage and Thresholds. For each patient sample (Eye 1-Eye 51) shown on the x-axis, the bar graphs illustrate the total positivity percentage (y-axis) alongside three distinct thresholds (Num+1, Num+2, Num+3), reflecting the intensity of target antibody staining as quantified by QuPath.

Overall survival was then observed and stratified by Multigene Score. This analysis integrated IHC data (including total positivity percentages and Num+1, Num+2, and Num+3 thresholds for each patient and each marker) with comprehensive patient clinical data (Karolinska Institute) available for patients 5 to 51, enabling meaningful stratification. These data included Vasculogenic mimicry (yes/no), Age at diagnosis, Diagnosis Date, Birth year, Gender (Man/Woman), Deceased (True/False), Cell type (Epiteloid/Mixed/Spindle), Deceased date, Dead from uveal melanoma (yes/no), Cause of death (Alive/UM death/Other death), Eye (Right/Left), Days from Diagnosis to death, Years from Diagnosis to death or last known to be alive, Diagnosis (Choroidal, Iris, Ciliochoroidal), Tumor diameter (mm), Tumor height (mm), Ciliary body involvement (yes/no), T Category, Extrascleral growth (yes/no), T category 1 to 4, N, M, Stage I-IV, Stagecoded, Primary treatment (Brachytherapy/Enucleation), TTT (At least one/ No), Metastasis (metastasis date known), Metastasis diagnosis date, Enucleation (either primary or secondary treatment).

A critical aspect of this cohort is that all patients were deceased at the time of analysis. Specifically, out of 47 patients, 15 did not die from UM, highlighting the importance of cause-specific mortality analysis in this context.

The Kaplan-Meier survival curve *(Fig.31)* illustrates the cumulative survival probability based on a calculated Multigene Score (MGS). To generate the Kaplan-Meier survival curves, the SPSS software was used. For each target gene, the 30th highest percentile of expression was calculated and used as a threshold to stratify the samples into high and low expression groups for each marker. Subsequently, a multivariate Cox proportional hazards regression was performed to identify genes significantly associated with survival. For this analysis, patient status was defined based on the cause of death, distinguishing between “Dead from uveal melanoma (yes/no)” and “Cause of death (Alive/UM death/Other death).” A Multigene Score (MGS) was then calculated as a weighted sum of the expression levels of the selected genes, using the corresponding beta coefficients from the Cox regression as weights. This MGS was used to stratify patients into “high” and “low” score groups, and Kaplan-Meier survival curves were generated by applying the Log-Rank (Mantel-Cox) method. A higher MGS corresponds to a worse prognosis, whereas a lower MGS indicates a better prognosis.

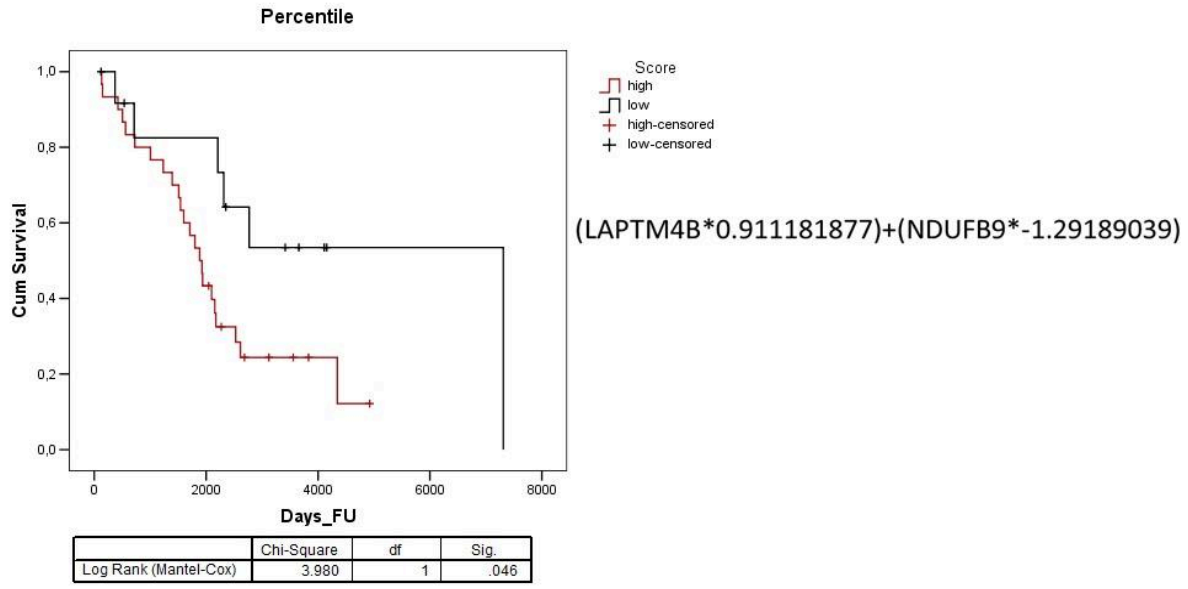

Fig.31 | Overall Survival Stratified by Multigene Score (MGS). Kaplan-Meier curves illustrate cumulative survival based on an MGS derived from LAPTM4B and NDUFB9 expressions. The cumulative survival (y-axis) is plotted against follow-up time in days (x-axis). Patients with a high MGS show significantly poorer overall survival compared to those with a low MGS (Log Rank p = .046). .

An in-depth evaluation of the Kaplan-Meier curve suggests that patients with a "high" MGS (red curve) exhibited significantly worse overall survival compared to those with a "low" MGS (black curve). The statistical significance of this difference was assessed using the Log Rank (Mantel-Cox) test, yielding a Chi-Square value of 3.980 with 1 degree of freedom and a p-value of .046. This robust association underscores the MGS, derived from LAPTM4B and NDUFB9 expression, as a relevant prognostic indicator for disease-specific mortality in this cohort.

Overall, these results demonstrated a strong positive correlation between ASAP1 and both LAPTM4B and NDUFB9 and suggest that these three markers are co-expressed in an amplification-driven manner and that the analyzed cohort exhibits widespread Chr8q amplification.

A key step in obtaining a complete picture of the correlation between these targets and Chr8q status was the direct assessment of its status in these samples. Therefore, to detect copy number changes at the DNA level and confirming or not the presence of 8q gain, Fluorescence In Situ Hybridization (FISH) was employed with probe targeting ASAP1 (gene localised on the 8q

region), together with the relative reference probe for the Chr8 (Empire Genomics) *(Fig.32)*. Initial setup and validation of the FISH protocol relied on reference samples for which the 8q amplification status had been previously established via MelArray: Eye1 and Eye2, amplified, and not amplified respectively *(Fig.33)*. These reference samples should have facilitated the classification of the remainder of the cohort into two primary groups: amplified and non-amplified. It has to be noted that Eye2, even if categorised as not-amplified after MelArray analysis, presents a signal in correspondence of the long arm of chromosome 8 *(Fig.33B)*. However, this signal is not as strong as for the Eye1*(Fig.33A)*.

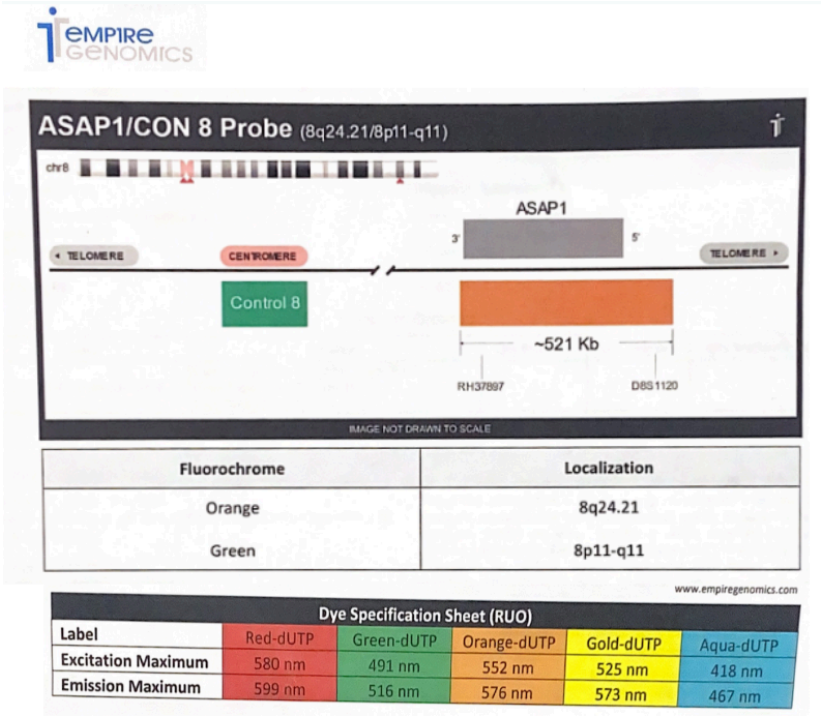

Fig.32 | Design and Genomic Localization of the ASAP1/CON 8 FISH Probe. This diagram illustrates the design of the fluorescence in situ hybridization (FISH) probe set (Empire Genomics) for detecting specific genomic regions on chromosome 8. The orange fluorochrome targets the 8q24.21 locus, corresponding to the ASAP1 gene, and spans approximately 521 Kb. The green fluorochrome represents the Control 8 probe, localized to the 8p11-q11 region, serving as an internal reference.

A

Resultate:

1. Nachweis pathogener oder potentiell pathogener Mutationen:

Gen	Chromosomale Lokalisation	Nukleotid-änderung	Aminosäuren-änderung	Mutations-frequenz %	Total Coverage
BAP1	Chr3: 52437246	c.1798G>T	p.Glu600Ter / p.E600*	83%	322
GNA11	Chr19: 3118942	c.626A>T	p.Gln209Leu / p.Q209L	40.70%	316

2. Genomweite Copy Number Analyse (angepasst an den geschätzten Tumorzellanteil).

Amplifikation des q-Arms von Chromosom 8.

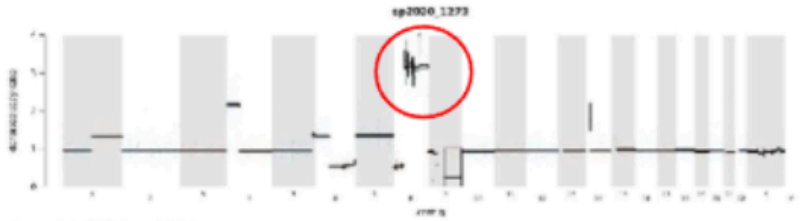

Anzahl CNVs: 1594

B

Resultate:

1. Nachweis pathogener oder potentiell pathogener Mutationen:

Gen	Chromosomale Lokalisation	Nukleotid-änderung	Aminosäuren-änderung	Mutations-frequenz %	Total Coverage
GNAQ	chr9:80409488	c.626A>C	p.Gln209Pro / p.Q209P	36	2936

2. Genomweite Copy Number Analyse (angepasst an den geschätzten Tumorzellanteil)

Anzahl CNVs: 4322

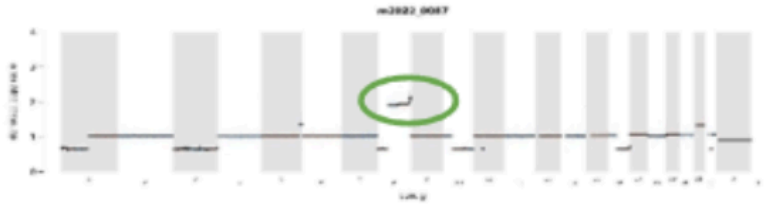

Fig.33 | MelArray Results for Chromosome 8q Amplification Status. (A) Representative MelArray profile for Eye1, indicating chromosome 8q amplification. (B) Representative MelArray profile for Eye2, demonstrating less detectable chromosome 8q amplification.

During the initial FISH attempt, the bleaching procedure was deliberately omitted to preserve tissue integrity. However, despite the successful detection of the green control probe signal (Control 8 probe), pronounced autofluorescence was observed, potentially obscuring other signals *(Fig.34)*.

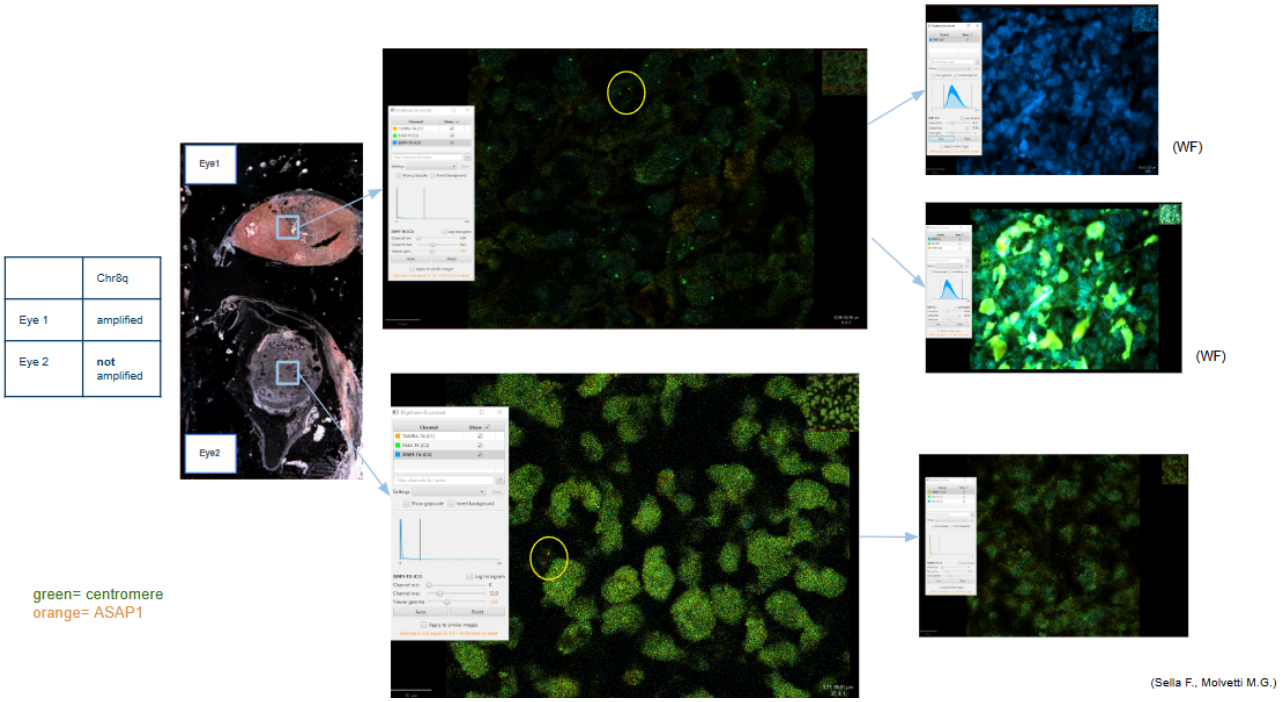

Fig.34 | First FISHAttempt. Representative images from the initial FISH protocol attempt on UM reference samples. The left panel shows low-magnification views (4x) of Eye 1 (amplified for 8q) and Eye 2 (not amplified for 8q), with blue boxes indicating regions of interest for high-magnification imaging (63x oil). The right panels display magnified views, showing green signals (centromere probe for Chr8) and blue nuclear counterstain (DAPI). Despite visible probe signals, significant tissue autofluorescence is evident across the fields, interfering with specific signal detection, as highlighted by the overall green background and accompanying histogram profiles. WF= Wide Field, other images are Confocal ones.

In the second FISH attempt, several parameters were optimized, including the bleaching process. Still, even when seeking probe signals with z-stack, autofluorescence persisted and interfered with confocal signal detection *(Fig.35)*.

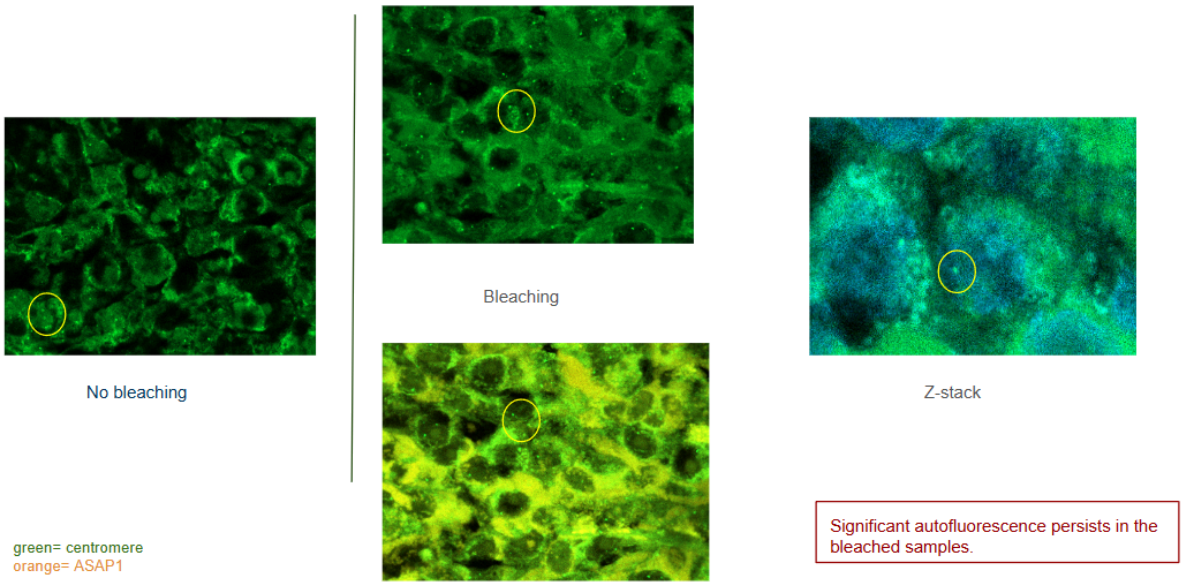

Fig.35 | Second FISH Attempt. Images compare samples with "No bleaching" (top left) versus "Bleaching" (top center), demonstrating the impact on autofluorescence. A Z-stack acquisition (right) was also employed to mitigate signal interference. Despite these optimizations, including attempts to reduce background autofluorescence (green, representing the centromere probe for Chr8; orange for ASAP1), significant autofluorescence persisted, interfering with specific probe signal detection and confocal imaging.

Following a third and final FISH attempt *(Fig.36A-B)*, where several other parameters were optimized and laser bleaching at 100% intensity was also unsuccessful, it was concluded that FISH was too time-consuming and unreliable for UM samples.

A

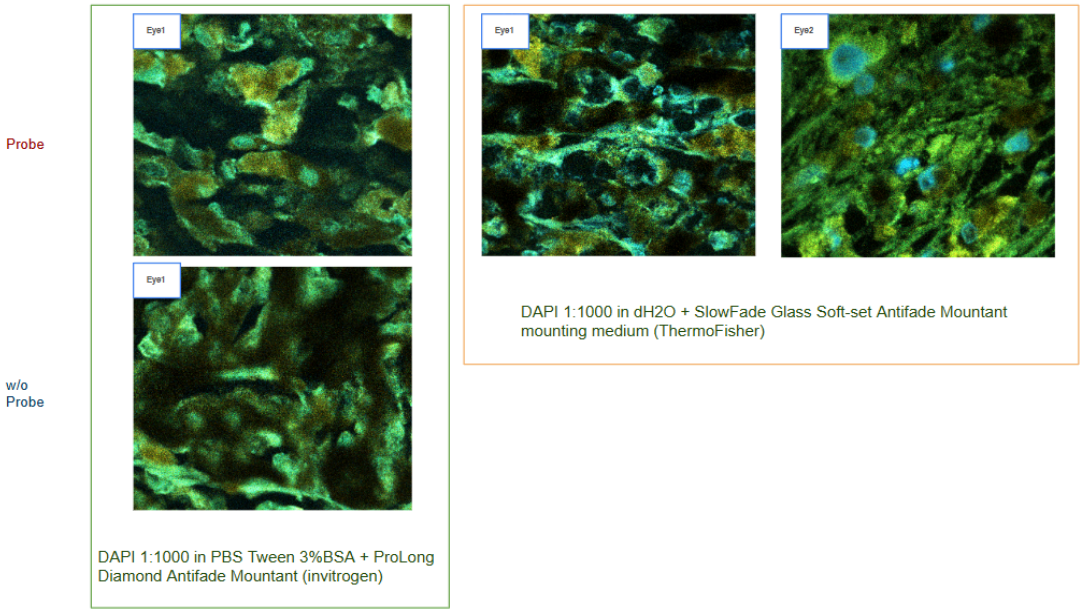

B

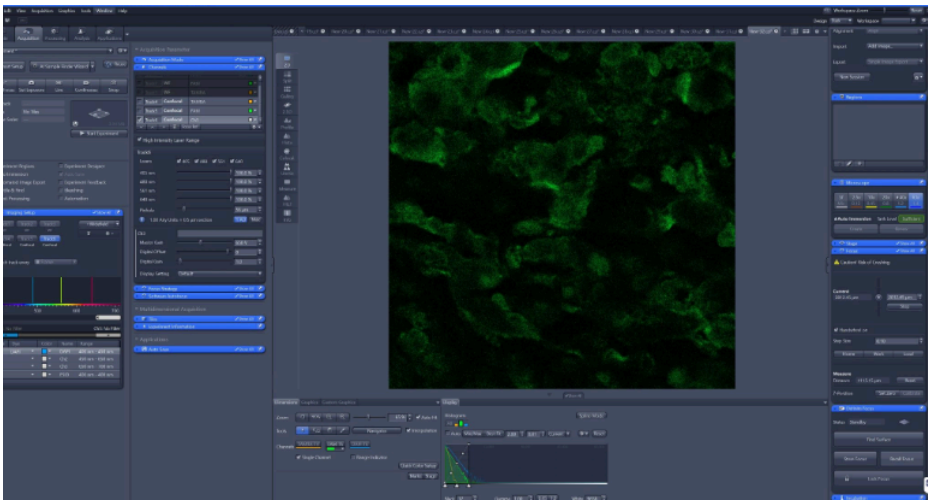

Fig.36 | Third FISH attempt. (A) Appearance of samples with the FISH probe ("Probe") compared to controls without the probe ("w/o Probe"), demonstrating the continued presence of background autofluorescence under varied mounting conditions (DAPI 1:1000 in PBS Tween 2%BSA + ProLong Diamond Antifade Mountant, and DAPI 1:1000 in dh2O + SlowFade Glass Soft-set Antifade Mountant). (B) Persistence of autofluorescence, as observed in a microscopy software interface, confirming that even after extensive parameter optimization and aggressive laser bleaching (as described in the text), FISH remained unsuitable for reliable signal detection in these samples.

The multiple attempts to optimize the FISH technique highlighted a significant and unresolved issue related to the strong autofluorescence of the FFPE UM samples, which proved resistant even to laser bleaching. Despite the failure to obtain a reliable FISH signal, this work concluded that the technique is not sufficiently robust for the analysis of archived UM samples and motivated the need to adopt a more reliable approach for DNA copy number analysis. To proceed with the assessment of Chr8q status, the subsequent strategy was therefore to extract DNA from the remaining FFPE samples to perform Whole-Exome Sequencing (WES), an approach that was deemed more suitable for samples of this nature.

Therefore, an initial selection of FFPE samples was performed, with a subset excluded due to insufficient tumor content. Subsequently, DNA was extracted from the remaining samples for Whole-Exome Sequencing (outsourced to Novogene). This resulted in a final cohort of 45 patients: 3 from USZ and 42 from the Karolinska Institute.

Despite the relatively old age of the samples (dating from 2000 to 2008) and FFPE preservation, the quality of the extracted DNA proved sufficient to yield adequate whole-exome sequencing coverage. Raw FASTQ files were trimmed and aligned to the hg38 human reference genome (hg38-GATK version). Subsequent processing for variant calling was performed using the GATK pipeline within Sarek. Minimal gains were observed on chromosome 8p, while more substantial alterations were evident on 8q. *(Fig.37)*

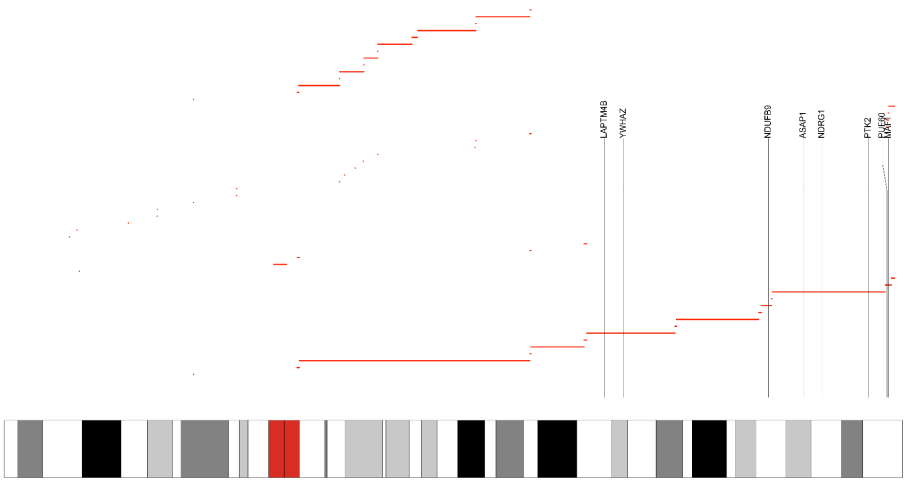

Fig.37 | Copy Number Variation Profile of Chromosome 8 in UM samples. This ideogram illustrates regions of genomic gain (indicated by red horizontal segments) along chromosome 8, as identified from Whole-Exome Sequencing data. Key genes relevant to the study are mapped to their respective chromosomal loci. The visual representation highlights minimal gains on the 8p arm, contrasting with more substantial copy number alterations observed predominantly on the 8q arm.

Copy number variations (CNVs) were then estimated using CNVkit (integrated within Sarek). A t-test was performed to assess differences in AUC levels between samples with and without copy number alterations for each gene. Of the genes analyzed, only LAPTM4B approached statistical significance ($p \approx 0.07$). The corresponding AUC plot *(Fig.38)* illustrates the performance based on copy number data, where amplified samples were assigned class 1 and non-amplified samples class 0. AUC values, ranging from 0 to 1, reflect the ability to distinguish between two classes, with 0.5 indicating poor predictive power. However, the generated ROC curves were not deemed satisfactory, necessitating the exploration of alternative tools for future variant and CNV calling.

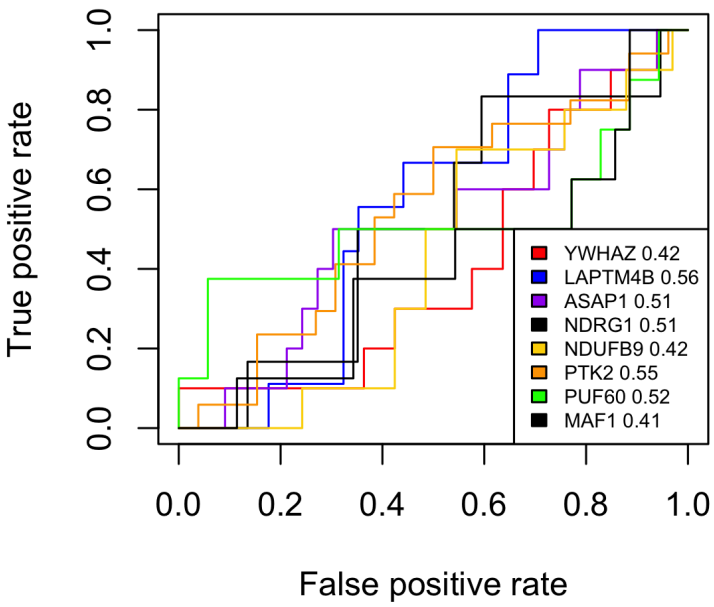

Fig.38 | Receiver Operating Characteristic (ROC) Curves for Gene Copy Number Variation Discrimination. ROC curves illustrate the ability of individual genes to differentiate between amplified and non-amplified samples based on copy number data. Overall, the displayed curves and their associated AUC values (e.g., LAPTM4B AUC = 0.56) indicate limited discriminatory power.

Attempts were also made utilizing cn.mops (a data processing pipeline for copy number variations and aberrations) *(Fig.39)*; however, this tool proved problematic, as its reliance on a window-based comparison across multiple samples led to the introduction of artifacts and unreliable calls due to poor coverage in certain exomes.

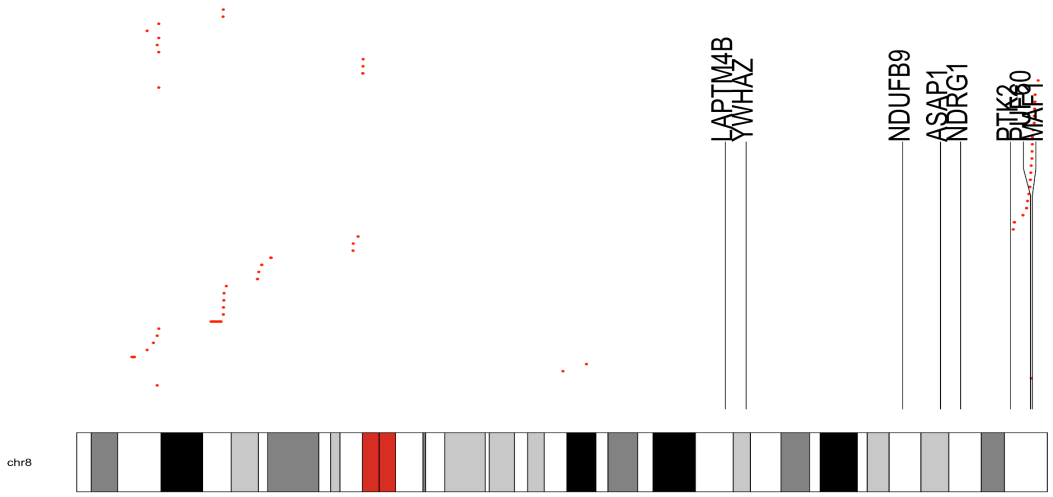

Fig.39 | Copy Number Variations on Chromosome 8 as called by cn.mops. This ideogram displays genomic gains (red segments) on chromosome 8, highlighting the artifacts and unreliable calls generated by the cn.mops tool due to suboptimal exome coverage.

To better investigate the results, a more SNP-based approach was used. To do that, two copy number detection methods were applied: cnvkit[97], as available in the Sarek pipeline, and ASCAT[98]. While the first method is more focused on a read depth calculation based approach (e.g. the number of sequencing reads mapping on a part of the genome), ASCAT was initially designed to infer copy number from SNP arrays[98], in this case the CNA detection is based on the comparison between allele frequencies in tumor and related control samples[99]: LH17.364, LH17.3554. A notable gain (+1) is observed on chromosome 8q, contrasting with the control "LH17_364.tumour," which did not exhibit 8q amplification by array-CGH *(Fig.40)*. These curves demonstrate the predictive power of protein expression in distinguishing samples with high 8q amplification from non-metastatic patients. There were found 20 positive patients, ensuring a more balanced representation *(Fig.41)*.

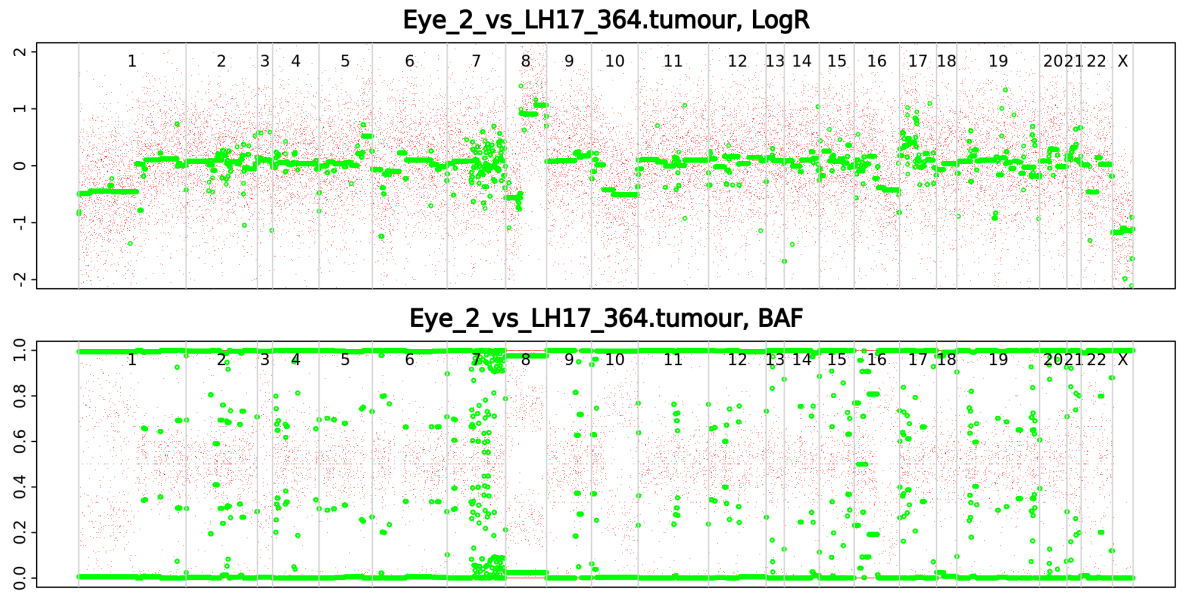

Fig.40 | Copy Number Variation (CNV) Analysis of Sample Eye2 vs. Control.
This ASPCF (Allele-Specific Purity and Ploidy Estimation for Cancer) graph displays the LogR (logarithm of the ratio of SNP allele counts in tumor versus control) and B-Allele Frequency (BAF) profiles for sample "Eye2_vs_LH17_364.tumour." The top panel (LogR) illustrates copy number changes across the genome, while the bottom panel (BAF) indicates allelic imbalance.

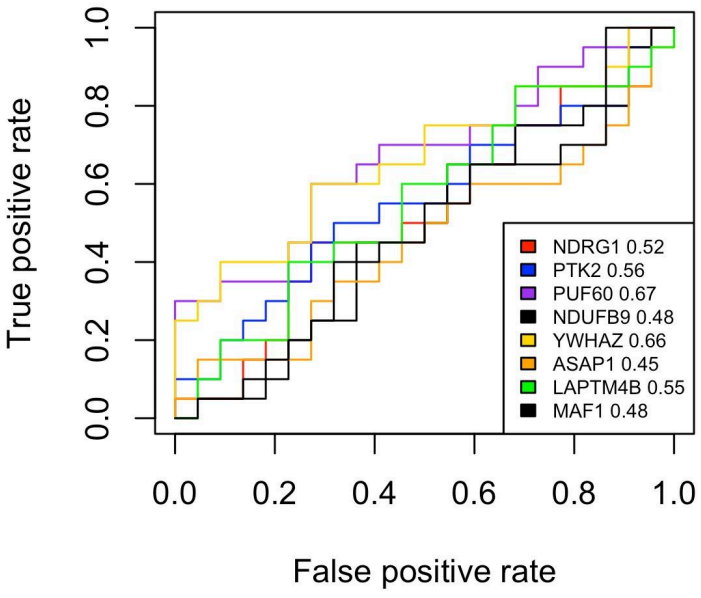

Fig.41 | ROC curves illustrate the diagnostic performance of individual gene expression levels (indicated by different colored lines) against ASCAT-derived copy number status. Gain on chromosome 8q was defined by an ASCAT value greater than 0.5, with 0 representing no gain.

Whole-Exome Sequencing (WES) proved to be a more suitable approach for DNA analysis of FFPE samples, providing raw data of sufficient quality despite the age of the samples. However, the initial analysis of Copy Number Variations (CNVs) with CNVkit only showed a trend towards statistical significance for LAPTM4B, and the use of tools like cn.mops introduced artifacts due to poor coverage in certain exomes, highlighting the challenges of analyzing WES-derived CNV data from archived material. Despite these limitations, the exploration of an SNP-based approach, specifically utilizing ASCAT, allowed us to overcome the initial qualitative challenges. This enabled a more reliable, albeit qualitative, assessment of the presence or absence of Chr8q gain, establishing a balanced cohort for subsequent analyses. For future studies, the limited initial predictive power and the issues encountered with cn.mops indicate the necessity of exploring alternative pipelines for variant and CNV calling or integrating data from deeper or targeted sequencing, where possible.

Following the trimming of samples for DNA extraction and subsequent Whole-Exome Sequencing, authorization was obtained from Prof. Stålhammar and Levesque for the construction of Tissue Microarrays (TMAs), which involve the coring of FFPE blocks. TMAs were constructed to enable high-throughput histological analysis of the UM cohort. For each patient's eye, three distinct tissue cores were strategically selected: one from the tumor border, one from the tumor core (prioritizing areas exhibiting inflammatory infiltrates where present), and one from adjacent non-tumoral tissue, typically derived from the ciliary body. To ensure accurate selection and annotation of these specific regions for TMA punching, preliminary staining with H&E, CD3 (T cells target), and S100/MelanA (melanoma marker) was performed. Punches were then embedded into recipient blocks utilizing the Xenium frame system. This setup allowed for precise microtome sectioning of TMA blocks, ensuring all samples were accurately positioned within the capture area of the Xenium slide for direct downstream processing, including Xenium-specific protocols, other immunohistochemical analyses, or spatial transcriptomics. This project is still being developed.

CHAPTER V

DISCUSSION AND CONCLUSION

The clinical management of UM remains a significant challenge in oncology. Despite substantial genomic strides enabling the stratification of patients into high- and low-risk classes[12,16], UM is characterized by an inherently aggressive course[100,101], often leading to liver metastasis[102] with limited systemic therapeutic options[103]. This disparity between robust prognostic classification[12] and lack of effective treatment[104] underscores a profound and urgent need for deeper biological understanding, on both the disease's etiology and the mechanisms that drive metastatic competency and resistance.

To address this critical gap, this study, in a first instance, investigated the diverse cellular and molecular impacts of BL exposure on melanocyte models, aiming to elucidate its potential role in UM tumorigenesis. The findings collectively provide comprehensive insights into BL-induced effects, revealing complex cellular responses that vary depending on the experimental context and specific cellular processes examined. Alterations in cell cycle distribution were observed, suggesting that prolonged BL exposure impacts the progression of Melan-a cells through the cell cycle, leading to a reduced proportion of quiescent/G1 phase cells and an accumulation within the S phase. Furthermore, prolonged blue light exposure was found to induce a significant increase in intracellular reactive oxygen species (ROS) levels in Melan-a cells, indicative of oxidative stress.

The literature has previously suggested that BL, a short-wavelength visible light, can induce DNA damage in melanocytes by impacting the cellular oxidative state[105]; but its role in UM was never observed . The presented data suggest, in agreement with these pre-existent observations, that this mechanism is active in the investigated cellular models. The results, however, revealed an unexpected finding: the increase in ROS was not mediated by an increase in hydrogen peroxide (H_2O_2) production, which was, on the contrary, reduced. This indicates that alternative mechanisms, independent of direct H_2O_2 induction, are involved in the cellular response to BL. The BL-adapted 72A cell line also maintained this adaptive response to subsequent exposures, suggesting that cells can develop a resistance or a modified response to BL-induced oxidative stress over time.

Analyses of mutational signatures provided the most significant evidence, directly linking the results to the molecular mechanisms of UM. The literature recognizes that mutations induced by

UV radiation in CM produce distinct mutational signatures (e.g. SBS7a and SBS7b)[87]. In contrast, BL exposure generated a mutational signature characterized predominantly by SBS1 and SBS5, signatures that are known to be present in UM[87]. The absence of the typical CM (UV-induced) signatures in the BL exposure model is of crucial importance. This finding supports the literature suggesting that BL can act as an "additional hit" in the malignant transformation of nevi that already harbor driver mutations such as those in the GNAQ gene[54]. This study provides direct evidence that BL-induced damage exhibits a mutational profile that, unlike UV damage, aligns with that of UM.

Further studies on the effects of BL should focus on elucidating the precise molecular pathways responsible for the observed H_2O_2 reduction and the ROS-independent apoptotic response. Additionally, investigating the long-term effects of chronic BL exposure and validating these findings in patient-derived primary melanocyte cultures would be beneficial. In this regard, studies in vivo are already in development.

Concurrently with the etiological study, a distinct research effort focused on establishing genetically defined cellular models to reproduce the key alterations driving aggressive UM. To this end, the $GNA11^{Q209L}$ clone was successfully generated in the laboratory of Dr. Pfeffer (PhD co-Tutor). Currently, characterization of this cell line is underway to allow the subsequent *in vivo* studies. In this regard, it is important to emphasize that, although promising results have already been obtained, considering that they have not yet been published, and that I was not directly involved in this part of the work, they have not been reported here.

Amplification of the long arm of chromosome 8 (8q) is a genetic aberration known to independently contribute to a metastatic phenotype in UM[40]. The ASAP1 gene has been previously identified as a well-established 8q gain marker, but does not fully explain the increased metastatic risk[21] since it is overexpressed in only a part of chr8q-amplified cases. Building on these premises, the made bioinformatic analyses on four cohorts[89] of UM patients identified 8 target genes on chromosome 8q that are associated with chromosome 8q amplification and poor prognosis: NDUFB9, LAPTM4B, MAF1, NDRG1, YWHAZ, PTK2, PUF60, ASAP1. In particular, subsequent IHC analysis and Pearson's correlation showed that LAPTM4B and NDUFB9, in comparison to ASAP1, are potentially relevant. The findings on the relevance of LAPTM4B and NDUFB9 appear to be confirmed by the literature. For instance, LAPTM4B overexpression is documented in a variety of cancers where it plays a crucial role in regulating tumor suppression, proliferation, invasion, metastasis, apoptosis resistance, autophagy

initiation, and drug resistance[106]. Furthermore, genetic polymorphisms of this gene have been linked to tumor susceptibility[107]. Additionally, LAPTM4B is known to regulate the autophagy process and the release of exosomes, which in turn affect tumor cell survival and drug resistance[107]. Its expression has also been shown to contribute to de novo chemoresistance to anthracyclines and to be permissive for metastatic recurrence in women with primary breast cancer[108]. Analogously, the relevance of NDUFB9 as a potential functional gene in the metastatic phenotype is also supported by its biological function and by the literature. NDUFB9 is a subunit of the mitochondrial electron transport chain Complex I, which is crucial for NADH oxidation and cellular energy production via oxidative phosphorylation[109]. Given the importance of metabolic reprogramming in tumor cells, the high expression of NDUFB9 has been identified as a potent biomarker and prognostic factor in various cancers, including uveal melanoma, where its overexpression correlates with unfavorable prognosis[109]. These results collectively suggest that NDUFB9 is a functional driver that, through its impact on metabolism, plays a significant role in UM prognosis. Taken together, these findings support the conclusion that the high expression of these genes suggests they are not merely "passenger genes" but rather functional contributors to the metastatic phenotype. This study also delved into the resistance of high-risk uveal melanomas (those with monosomy 3 and 8q gain) to conventional therapies and immunotherapies, a phenomenon that has been documented in the literature[2,3]. The superior expression levels of LAPTM4B and NDUFB9 in some patients led to the development of a novel Multigene Score (MGS); proved to be a powerful prognostic tool, capable of significantly stratifying patients into high- and low-risk groups with a notable difference in overall survival. This underscores the MGS's potential as a more refined and effective indicator for disease-specific prognosis than a single marker alone. In conclusion, this study identifies a novel prognostic score based on the expression of LAPTM4B and NDUFB9 as a potent indicator of disease-specific mortality in UM.

The ASCAT method demonstrated considerable potential, especially when considering the non-optimal quality of the paraffin-embedded material and the limited sequencing coverage, which made deletions more challenging to detect. It was not possible to obtain a precise estimation of the copy number size, but rather a qualitative assessment of copy number presence or absence. This was achieved by comparison with samples LH17.364 and LH17.3554[99], for which allele frequencies were known from array analysis.

A better integration of the functional component (IHC) and the genomic data on copy number will be accomplished by comparing metastatic and non-metastatic samples with a matched 8q amplification. To this end, a dataset will be prepared with samples from non-metastatic patients.

The findings highlight the need for further functional investigations into the specific roles of these genes and suggest that they could be promising therapeutic targets, especially in the context of challenges posed by therapy resistance. Validation in larger, independent cohorts will be a crucial step for the translation of these findings into practical clinical tools.

1. Future Studies and Perspectives

The findings of this research lay a robust foundation for several lines of translational and biological investigation, highlighting the next critical steps required to advance the clinical understanding and management of Uveal Melanoma.

Regarding the etiological role of BL (Aim 1), while the alignment of BL-induced mutational signatures (SBS1 and SBS5) with those found in UM provides compelling evidence, further functional work is necessary. Future studies must focus on dissecting the precise molecular pathways responsible for the observed decrease in H_2O_2 production and the concurrent increase in ROS-independent apoptotic responses following BL exposure. It will also be crucial to investigate the long-term effects of chronic BL exposure and to validate the mutational findings in patient-derived primary melanocyte cultures to strengthen the clinical relevance, noting that in vivo studies are already underway.

The successful generation of genetically defined cell line models is a critical step towards understanding aggressive UM (Aim 2). Future efforts will focus on leveraging these tools for *in vivo* studies. Specifically, efforts must be finalized to complete the creation of cellular models that fully recapitulate the full UM etiopathogenesis, including the $GNA11^{Q209L}$ clone already established. The crucial next step is to generate an *in vivo* mouse model utilizing the aggressive double-mutant cell line $GNA11^{Q209L}$-$BAP1^{-/-}$, which will serve as an essential tool for evaluating metastatic progression and testing novel therapeutic interventions under physiological conditions.

The development of the robust Multigene Score (MGS) based on LAPTM4B and NDUFB9 (Aim 3) necessitates a strong translational approach. Validation of the MGS in larger, more heterogenic and independent patient cohorts remains the paramount next step to ensure its

robustness and facilitate its translation into a routine clinical prognostic tool. Furthermore, functional investigations are required to fully elucidate the specific roles of LAPTM4B and NDUFB9 in driving the metastatic phenotype, suggesting them as promising therapeutic targets against therapy resistance. Finally, a better integration of the functional component (IHC) and genomic data on copy number will be achieved by preparing a comparative dataset of metastatic and non-metastatic samples with matched 8q amplification, to move beyond qualitative copy number assessments.

Finally, to address the challenge of therapy resistance in the metastatic setting, the project will pivot towards high-resolution spatial biology. The recently executed Xenium in situ assay, part of a larger clinical trial led by Dr. Ramelyte E. (USZ), in collaboration with FGCZ, Zurich on pre- and post-Tebentafusp treated metastatic samples will be analyzed. This effort will leverage spatial transcriptomics to achieve spatially resolved cell-type annotation, differential gene expression analysis, and assessment of key cell-cell communication within the immune-modulatory tumor microenvironment. This spatial analysis will be complemented by multiplex imaging (Akoya) on the same slides to confirm the expression patterns of genes of interest, particularly those identified in the 8q gain region, ultimately shedding light on the potential immune-modulatory interactions of novel therapies within the metastatic niche.

Acknowledgements

The experimental work presented in this thesis was made possible through the collaboration and essential contributions of several individuals. Specific responsibilities were as follows:

Supervisors

- *Prof. Barbara Marengo* (Supervisor- Department of Experimental Medicine- University of Genoa): Provided comprehensive supervision for the entire PhD project, guiding its design, execution, and interpretation. Her primary and defining contribution involved the conceptualization, development, and supervision of Aim 1.
- *Prof. Cinzia Domenicotti* (General Pathology Section Leader- Department of Experimental Medicine- University of Genoa): Provided the institutional and organizational framework for the research, ensuring necessary resources and infrastructure. Her role included final supervision of the scientific direction of the project over the three years, validating its coherence within the Department's research lines.
- *Dr. Ulrich Pfeffer* (Co-Supervisor, Host Lab Director - Gene Expression Regulation- IRCCS San Martino, Genoa): Provided institutional support and scientific mentorship by hosting the research activities in his laboratory, facilitating access to resources, and contributing to the strategic direction of all Aims.
- *Dr. Mitch Levesque* (External Supervisor, Host Lab Director - Translational Dermato - Oncology - University Hospital Zürich, CH): Provided the international research environment by hosting my research activities for one year, and contributed to the supervision of the molecular biology techniques during the execution of Aim 3.

Dr. Pfeffer U. Research Team

- Dr. Amaro A.: Performed crucial bioinformatic analyses supporting the development of all three Aims and contributed to the supervision of the molecular biology techniques.
- Dr. Reggiani F.: Performed crucial bioinformatic analyses supporting the development of all three Aims.
- Dr. El Rashed Z.: Contributed to specific in vitro tests for Aim 1 and Aim 2.

Dr. Levesque M. Research Team

- *Dr. Tastanova A.*, *Ms. Sella F.* and *Ms. Hermes V.*: Provided scientific mentorship, technical supervision, training, and hands-on support for experiments related to Aim 3.

External Collaborators

- *Dr. Stålhammar G.* (Ocular Oncology and Pathology Group Leader- Karolinska Institutet) and *Dr. Hagström A.*: Provided biological material (primary UM samples) and facilitated the acquisition necessary for the development of Aim 3.

APPENDIX

IHC stainings for each target gene on the UM cohort: each slide contains three distinct tumor samples (one per patient).

ASAP1

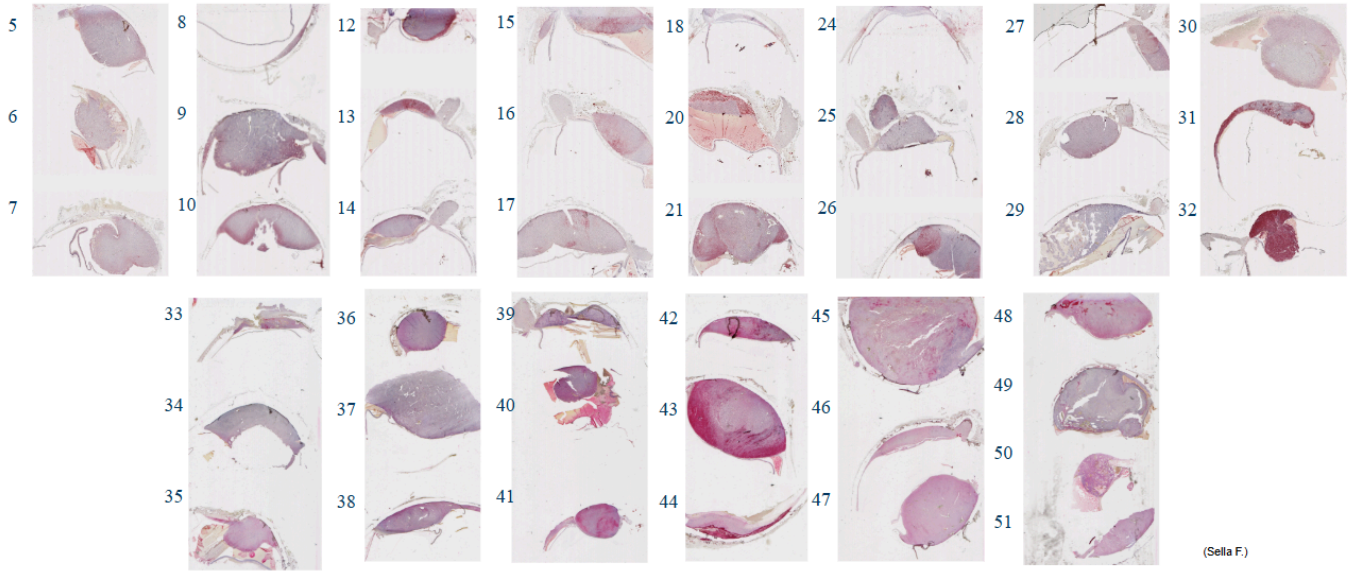

MAF1

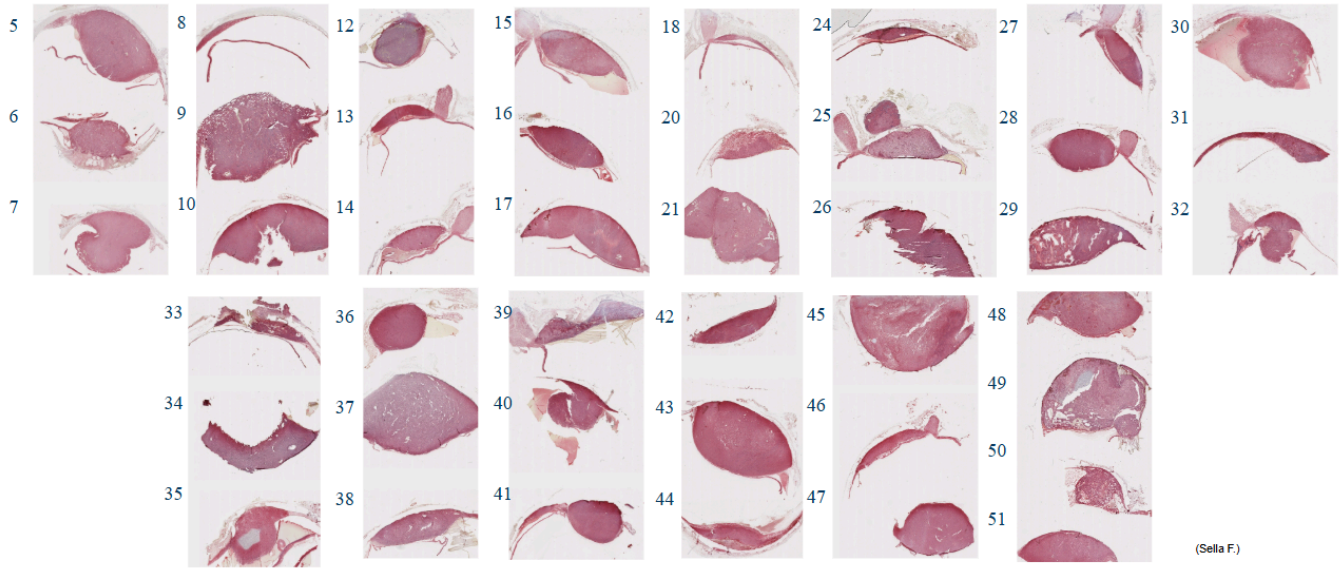

PUF60

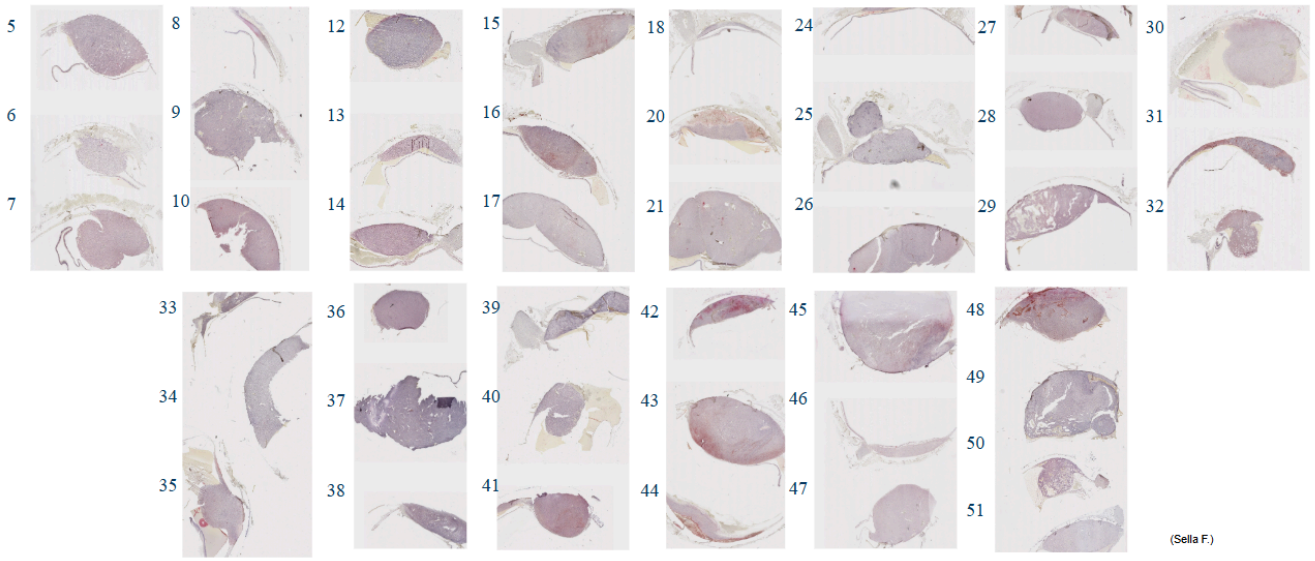

LAPTM4B

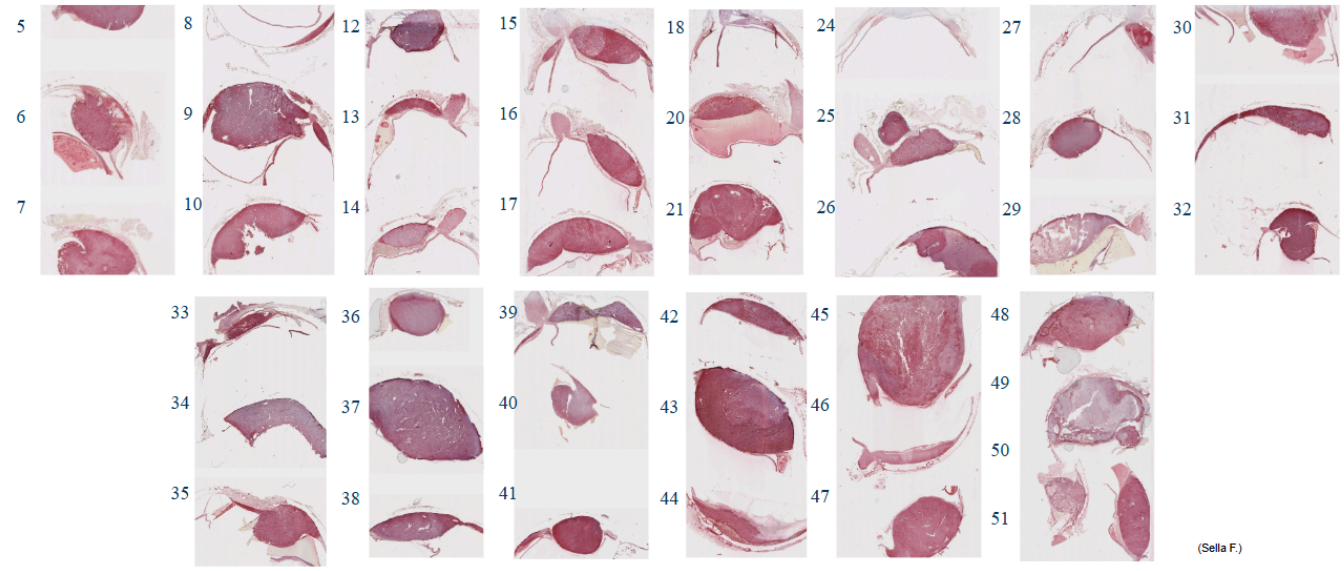

NDRG1

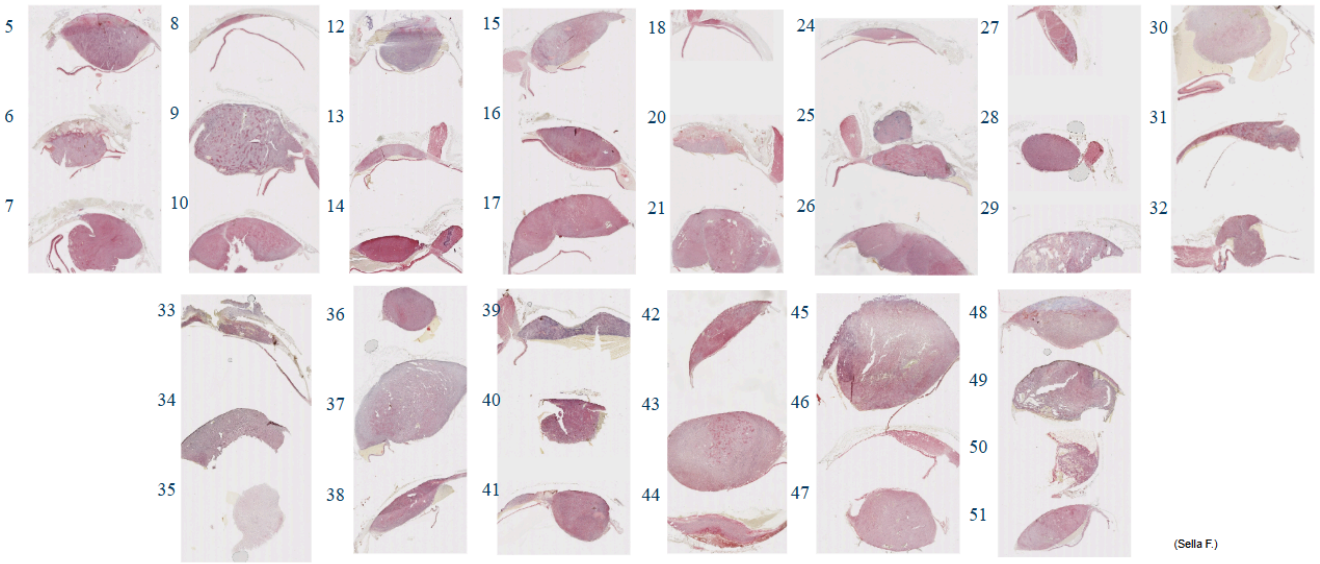
5
6
7
8
9
10
12
13
14
15
16
17
18
20
21
24
25
26
27
28
29
30
31
32
33
34
35
36
37
38
39
40
41
42
43
44
45
46
47
48
49
50
51
(Sella F.)

PTK2

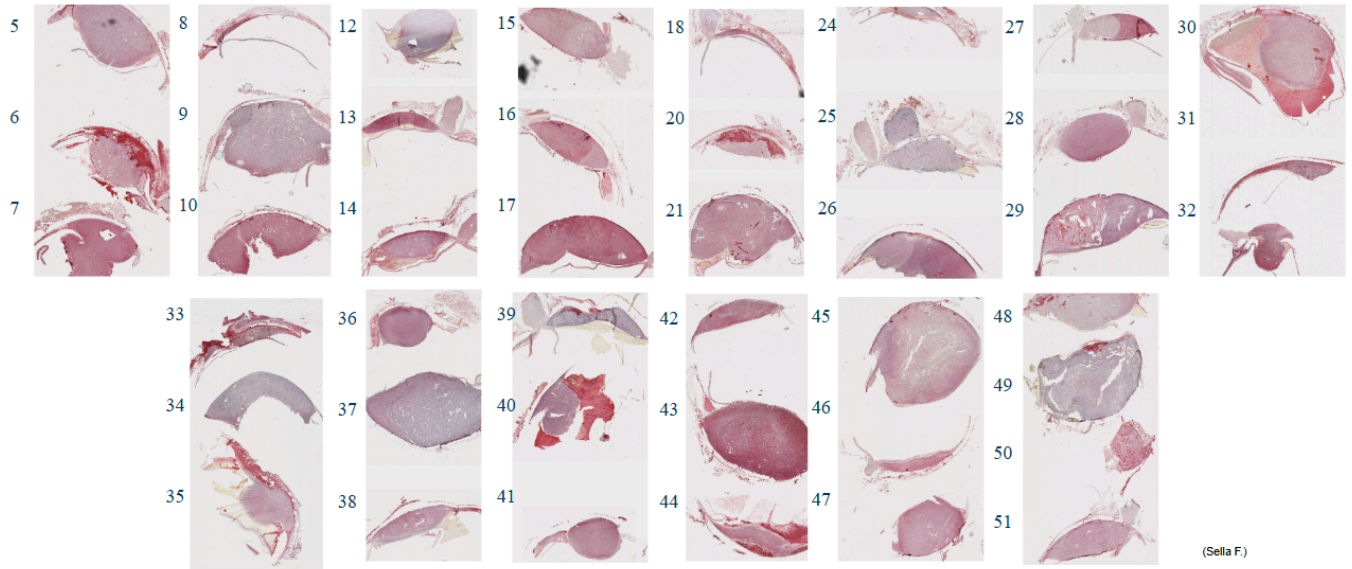
5
6
7
8
9
10
12
13
14
15
16
17
18
20
21
24
25
26
27
28
29
30
31
32
33
34
35
36
37
38
39
40
41
42
43
44
45
46
47
48
49
50
51
(Sella F.)

YWHAZ

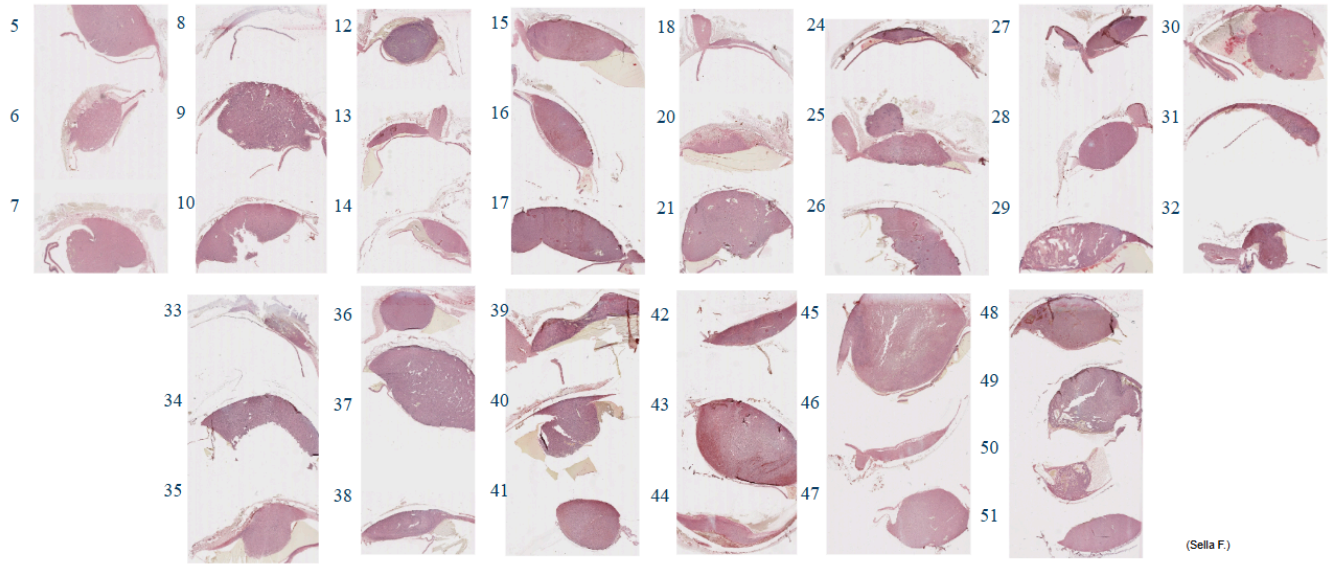

NDUFB9

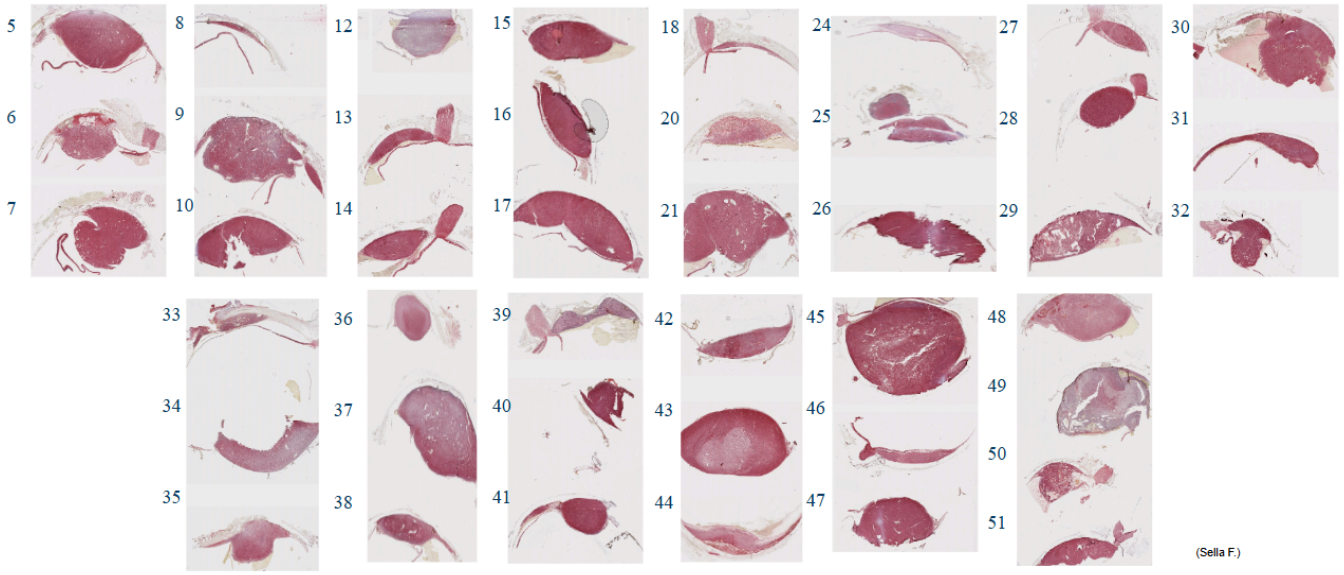

BIBLIOGRAPHY

1. Kels, B. D., Grzybowski, A. & Grant-Kels, J. M. Human ocular anatomy. *Clin. Dermatol.* **33**, 140–146 (2015).
2. Jager, M. J. *et al.* Uveal melanoma. *Nat. Rev. Dis. Primer* **6**, 24 (2020).
3. Nathan, P. *et al.* Overall Survival Benefit with Tebentafusp in Metastatic Uveal Melanoma. *N. Engl. J. Med.* **385**, 1196–1206 (2021).
4. Doherty, R. E., Alfawaz, M., Francis, J., Lijka-Jones, B. & Sisley, K. Genetics of Uveal Melanoma. in *Noncutaneous Melanoma* (eds. Scott, J. F. & Gerstenblith, M. R.) (Codon Publications, Brisbane (AU), 2018).
5. Amaro, A. *et al.* The biology of uveal melanoma. *Cancer Metastasis Rev.* **36**, 109–140 (2017).
6. Prescher, G. *et al.* Prognostic implications of monosomy 3 in uveal melanoma. *Lancet Lond. Engl.* **347**, 1222–1225 (1996).
7. Onken, M. D. *et al.* Functional gene expression analysis uncovers phenotypic switch in aggressive uveal melanomas. *Cancer Res.* **66**, 4602–4609 (2006).
8. Harbour, J. W. *et al.* Frequent mutation of BAP1 in metastasizing uveal melanomas. *Science* **330**, 1410–1413 (2010).
9. Chang, S.-H., Worley, L. A., Onken, M. D. & Harbour, J. W. Prognostic biomarkers in uveal melanoma: evidence for a stem cell-like phenotype associated with metastasis. *Melanoma Res.* **18**, 191–200 (2008).
10. Damato, B. & Coupland, S. E. Translating uveal melanoma cytogenetics into clinical care. *Arch. Ophthalmol. Chic. Ill 1960* **127**, 423–429 (2009).
11. Tschentscher, F. *et al.* Tumor classification based on gene expression profiling shows that uveal melanomas with and without monosomy 3 represent two distinct entities. *Cancer Res.* **63**, 2578–2584 (2003).

12. Onken, M. D., Worley, L. A., Ehlers, J. P. & Harbour, J. W. Gene expression profiling in uveal melanoma reveals two molecular classes and predicts metastatic death. *Cancer Res.* **64**, 7205–7209 (2004).

13. Onken, M. D., Worley, L. A., Tuscan, M. D. & Harbour, J. W. An accurate, clinically feasible multi-gene expression assay for predicting metastasis in uveal melanoma. *J. Mol. Diagn. JMD* **12**, 461–468 (2010).

14. Scholes, A. G. M. *et al.* Monosomy 3 in uveal melanoma: correlation with clinical and histologic predictors of survival. *Invest. Ophthalmol. Vis. Sci.* **44**, 1008–1011 (2003).

15. Bakhoum, M. F. & Esmaeli, B. Molecular Characteristics of Uveal Melanoma: Insights from the Cancer Genome Atlas (TCGA) Project. *Cancers* **11**, 1061 (2019).

16. Robertson, A. G. *et al.* Integrative Analysis Identifies Four Molecular and Clinical Subsets in Uveal Melanoma. *Cancer Cell* **32**, 204-220.e15 (2017).

17. Knudson, A. G. Mutation and cancer: statistical study of retinoblastoma. *Proc. Natl. Acad. Sci. U. S. A.* **68**, 820–823 (1971).

18. Hanahan, D. & Weinberg, R. A. Hallmarks of cancer: the next generation. *Cell* **144**, 646–674 (2011).

19. Piaggio, F. *et al.* Secondary Somatic Mutations in G-Protein-Related Pathways and Mutation Signatures in Uveal Melanoma. *Cancers* **11**, 1688 (2019).

20. Rodrigues, M. J. & Stern, M.-H. Genetic landscape of uveal melanoma. *J. Fr. Ophtalmol.* **38**, 522–525 (2015).

21. Yoo, J. H. *et al.* ARF6 Is an Actionable Node that Orchestrates Oncogenic GNAQ Signaling in Uveal Melanoma. *Cancer Cell* **29**, 889–904 (2016).

22. Mastronikolis, S. *et al.* Mutational landscape in Uveal Melanoma. *J. BUON Off. J. Balk. Union Oncol.* **26**, 1194–1197 (2021).

23. Harbour, J. W. The genetics of uveal melanoma: an emerging framework for targeted therapy. *Pigment Cell Melanoma Res.* **25**, 171–181 (2012).

24. Feng, X. *et al.* Hippo-independent activation of YAP by the GNAQ uveal melanoma oncogene through a trio-regulated rho GTPase signaling circuitry. *Cancer Cell* **25**, 831–845 (2014).

25. Yu, F.-X. *et al.* Mutant Gq/11 promote uveal melanoma tumorigenesis by activating YAP. *Cancer Cell* **25**, 822–830 (2014).

26. Feng, X. *et al.* A Platform of Synthetic Lethal Gene Interaction Networks Reveals that the GNAQ Uveal Melanoma Oncogene Controls the Hippo Pathway through FAK. *Cancer Cell* **35**, 457-472.e5 (2019).

27. Van Raamsdonk, C. D. *et al.* Frequent somatic mutations of GNAQ in uveal melanoma and blue naevi. *Nature* **457**, 599–602 (2009).

28. Van Raamsdonk, C. D. *et al.* Mutations in GNA11 in uveal melanoma. *N. Engl. J. Med.* **363**, 2191–2199 (2010).

29. Yasui, F., Miyazu, M., Yoshida, A., Naruse, K. & Takai, A. Examination of signalling pathways involved in muscarinic responses in bovine ciliary muscle using YM-254890, an inhibitor of the Gq/11 protein. *Br. J. Pharmacol.* **154**, 890–900 (2008).

30. Lapadula, D. *et al.* Effects of Oncogenic Gαq and Gα11 Inhibition by FR900359 in Uveal Melanoma. *Mol. Cancer Res. MCR* **17**, 963–973 (2019).

31. Livingstone, E. *et al.* GNAQ and GNA11 mutant nonuveal melanoma: a subtype distinct from both cutaneous and uveal melanoma. *Br. J. Dermatol.* **183**, 928–939 (2020).

32. Kennedy, S. *et al.* Prognostic Value of BAP1 Protein Expression in Uveal Melanoma. *Am. J. Surg. Pathol.* **48**, 329–336 (2024).

33. Karunamurthy, A. *et al.* Prevalence and phenotypic correlations of EIF1AX mutations in thyroid nodules. *Endocr. Relat. Cancer* **23**, 295–301 (2016).

34. Griewank, K. G. *et al.* TERT promoter mutations in ocular melanoma distinguish between conjunctival and uveal tumours. *Br. J. Cancer* **109**, 497–501 (2013).

35. Smit, K. N., Jager, M. J., de Klein, A. & Kiliç, E. Uveal melanoma: Towards a molecular

understanding. *Prog. Retin. Eye Res.* **75**, 100800 (2020).

36. Wespiser, M., Neidhardt, E. & Negrier, S. Uveal melanoma: In the era of new treatments. *Cancer Treat. Rev.* **119**, 102599 (2023).

37. Rossi, E. *et al.* Uveal Melanoma Metastasis. *Cancers* **13**, 5684 (2021).

38. Grossniklaus, H. E. *et al.* Metastatic ocular melanoma to the liver exhibits infiltrative and nodular growth patterns. *Hum. Pathol.* **57**, 165–175 (2016).

39. Lattier, J. M., Yang, H., Crawford, S. & Grossniklaus, H. E. Host pigment epithelium-derived factor (PEDF) prevents progression of liver metastasis in a mouse model of uveal melanoma. *Clin. Exp. Metastasis* **30**, 969–976 (2013).

40. Gallenga, C. E. *et al.* Genetic Basis and Molecular Mechanisms of Uveal Melanoma Metastasis: A Focus on Prognosis. *Front. Oncol.* **12**, 828112 (2022).

41. Piaggio, F., Tozzo, V., Bernardi, C. & Amaro, A. How many mutations does it take to make a uveal melanoma? *How many mutations does it take to make a uveal melanoma?*

42. Lamas, N. J. *et al.* Prognostic Biomarkers in Uveal Melanoma: The Status Quo, Recent Advances and Future Directions. *Cancers* **14**, 96 (2021).

43. Reggiani, F. *et al.* Interdependence of Molecular Lesions That Drive Uveal Melanoma Metastasis. *Int. J. Mol. Sci.* **24**, 15602 (2023).

44. Lalonde, E. *et al.* Improved Uveal Melanoma Copy Number Subtypes Including an Ultra-High-Risk Group. *Ophthalmol. Sci.* **2**, 100121 (2022).

45. Alexandrov, L. B., Nik-Zainal, S., Wedge, D. C., Campbell, P. J. & Stratton, M. R. Deciphering signatures of mutational processes operative in human cancer. *Cell Rep.* **3**, 246–259 (2013).

46. Alexandrov, L. B. *et al.* Signatures of mutational processes in human cancer. *Nature* **500**, 415–421 (2013).

47. de Lange, M. J. *et al.* Distribution of GNAQ and GNA11 Mutation Signatures in Uveal Melanoma Points to a Light Dependent Mutation Mechanism. *PloS One* **10**, e0138002 (2015).

48. Balazs, E. A. Studies on the structure of the vitreous body. I. The absorption of ultraviolet light. *Am. J. Ophthalmol.* **38**, 21–28 (1954).

49. Shah, C. P., Weis, E., Lajous, M., Shields, J. A. & Shields, C. L. Intermittent and chronic ultraviolet light exposure and uveal melanoma: a meta-analysis. *Ophthalmology* **112**, 1599–1607 (2005).

50. Di Cesare, S. *et al.* The effect of blue light exposure in an ocular melanoma animal model. *J. Exp. Clin. Cancer Res. CR* **28**, 48 (2009).

51. Jager, M. J., Magner, J. A. B., Ksander, B. R. & Dubovy, S. R. Uveal Melanoma Cell Lines: Where do they come from? (An American Ophthalmological Society Thesis). *Trans. Am. Ophthalmol. Soc.* **114**, T5 (2016).

52. Ransohoff, K. J. *et al.* Two-stage genome-wide association study identifies a novel susceptibility locus associated with melanoma. *Oncotarget* **8**, 17586–17592 (2017).

53. Kulbay, M. *et al.* Uveal Melanoma: Comprehensive Review of Its Pathophysiology, Diagnosis, Treatment, and Future Perspectives. *Biomedicines* **12**, 1758 (2024).

54. Nayman, T., Bostan, C., Logan, P. & Burnier, M. N. Uveal Melanoma Risk Factors: A Systematic Review of Meta-Analyses. *Curr. Eye Res.* **42**, 1085–1093 (2017).

55. Lachota, M., Lennikov, A., Malmberg, K.-J. & Zagozdzon, R. Bioinformatic Analysis Reveals Central Role for Tumor-Infiltrating Immune Cells in Uveal Melanoma Progression. *J. Immunol. Res.* **2021**, 9920234 (2021).

56. Mantovani, A., Schioppa, T., Porta, C., Allavena, P. & Sica, A. Role of tumor-associated macrophages in tumor progression and invasion. *Cancer Metastasis Rev.* **25**, 315–322 (2006).

57. Carvajal, R. D. *et al.* Advances in the clinical management of uveal melanoma. *Nat. Rev. Clin. Oncol.* **20**, 99–115 (2023).

58. Salvi, S. M. *et al.* Uveal Melanoma Regression after Brachytherapy: Relationship with Chromosome 3 Monosomy Status. *Ocul. Oncol. Pathol.* **3**, 87–94 (2017).

59. Scoles, S. & Ganesh, S. Current Therapies and Potential Strategies for Uveal Melanoma.

vol. 4 (2025).

60. Bai, H., Bosch, J. J. & Heindl, L. M. Current management of uveal melanoma: A review. *Clin. Experiment. Ophthalmol.* **51**, 484–494 (2023).

61. Buder, K., Gesierich, A., Gelbrich, G. & Goebeler, M. Systemic treatment of metastatic uveal melanoma: review of literature and future perspectives. *Cancer Med.* **2**, 674–686 (2013).

62. Hassel, J. C. *et al.* Three-Year Overall Survival with Tebentafusp in Metastatic Uveal Melanoma. *N. Engl. J. Med.* **389**, 2256–2266 (2023).

63. Shao, Y. F. *et al.* Immune Profiling of Uveal Melanoma Liver Metastases and Response to Checkpoint Inhibitors. *J. Immunother. Hagerstown Md 1997* **48**, 189–195 (2025).

64. Sacco, J. J. *et al.* Evolution of the tumor immune landscape during treatment with tebentafusp, a T cell receptor-CD3 bispecific. *Cell Rep. Med.* **6**, 102076 (2025).

65. Staeger, R. *et al.* Tebentafusp elicits on-target cutaneous immune responses driven by cytotoxic T cells in uveal melanoma patients. *J. Clin. Invest.* **135**, e181464 (2025).

66. Hawkins, L. *et al.* Understanding and Exacerbating the Biological Response of Uveal Melanoma to Proton Beam Therapy. *Cancers* **17**, 3104 (2025).

67. Sayan, M. *et al.* Clinical management of uveal melanoma: a comprehensive review with a treatment algorithm. *Radiat. Oncol. J.* **38**, 162–169 (2020).

68. Dendale, R. *et al.* Proton beam radiotherapy for uveal melanoma: results of Curie Institut-Orsay proton therapy center (ICPO). *Int. J. Radiat. Oncol. Biol. Phys.* **65**, 780–787 (2006).

69. Wang, S. *et al.* Real-time tracking of the Bragg peak during proton therapy via 3D protoacoustic Imaging in a clinical scenario. *Npj Imaging* **2**, 34 (2024).

70. Byun, H. K. *et al.* Physical and Biological Characteristics of Particle Therapy for Oncologists. *Cancer Res. Treat.* **53**, 611–620 (2021).

71. Jarczak, J., Karska-Basta, I. & Romanowska-Dixon, B. Deterioration of Visual Acuity

after Brachytherapy and Proton Therapy of Uveal Melanoma, and Methods of Counteracting This Complication Based on Recent Publications. *Med. Kaunas Lith.* **59**, 1131 (2023).

72. Damato, B. E. Treatment selection for uveal melanoma. *Dev. Ophthalmol.* **49**, 16–26 (2012).

73. Chan, A. W. *et al.* Proton Therapy in Uveal Melanoma. *Cancers* **16**, 3497 (2024).

74. Wilkinson, B., Hill, M. A. & Parsons, J. L. The Cellular Response to Complex DNA Damage Induced by Ionising Radiation. *Int. J. Mol. Sci.* **24**, 4920 (2023).

75. Bennett, D. C., Cooper, P. J. & Hart, I. R. A line of non-tumorigenic mouse melanocytes, syngeneic with the B16 melanoma and requiring a tumour promoter for growth. *Int. J. Cancer* **39**, 414–418 (1987).

76. Portantiolo Lettnin, A. *et al.* Protective effect of infrared-A radiation against damage induced by UVB radiation in the melan-a cell line. *J. Photochem. Photobiol. B* **163**, 125–132 (2016).

77. Oba-Shinjo, S. M. *et al.* Melanocyte transformation associated with substrate adhesion impediment. *Neoplasia N. Y. N* **8**, 231–241 (2006).

78. Santana-Filho, A. P. de *et al.* NMR metabolic fingerprints of murine melanocyte and melanoma cell lines: application to biomarker discovery. *Sci. Rep.* **7**, 42324 (2017).

79. de Souza, C. F. *et al.* Mining gene expression signature for the detection of pre-malignant melanocytes and early melanomas with risk for metastasis. *PloS One* **7**, e44800 (2012).

80. Huang, J. L.-Y., Urtatiz, O. & Van Raamsdonk, C. D. Oncogenic G Protein GNAQ Induces Uveal Melanoma and Intravasation in Mice. *Cancer Res.* **75**, 3384–3397 (2015).

81. Moore, A. R. *et al.* GNA11 Q209L Mouse Model Reveals RasGRP3 as an Essential Signaling Node in Uveal Melanoma. *Cell Rep.* **22**, 2455–2468 (2018).

82. Gangemi, R. *et al.* Mda-9/syntenin is expressed in uveal melanoma and correlates with metastatic progression. *PloS One* **7**, e29989 (2012).

83. Richards, J. R., Yoo, J. H., Shin, D. & Odelberg, S. J. Mouse models of uveal melanoma:

Strengths, weaknesses, and future directions. *Pigment Cell Melanoma Res.* **33**, 264–278 (2020).

84. Logan, P., Bernabeu, M., Ferreira, A. & Burnier, M. N. Evidence for the Role of Blue Light in the Development of Uveal Melanoma. *J. Ophthalmol.* **2015**, 386986 (2015).

85. Tsuchida, K. & Sakiyama, N. Blue light-induced lipid oxidation and the antioxidant property of hypotaurine: evaluation via measuring ultraweak photon emission. *Photochem. Photobiol. Sci. Off. J. Eur. Photochem. Assoc. Eur. Soc. Photobiol.* **22**, 345–356 (2023).

86. Chakravarthy, H., Georgyev, V., Wagen, C., Hosseini, A. & Matsubara, J. Blue light-induced phototoxicity in retinal cells: implications in age-related macular degeneration. *Front. Aging Neurosci.* **16**, 1509434 (2024).

87. Johansson, P. A. *et al.* Whole genome landscapes of uveal melanoma show an ultraviolet radiation signature in iris tumours. *Nat. Commun.* **11**, 2408 (2020).

88. Ehlers, J. P., Worley, L., Onken, M. D. & Harbour, J. W. DDEF1 is located in an amplified region of chromosome 8q and is overexpressed in uveal melanoma. *Clin. Cancer Res. Off. J. Am. Assoc. Cancer Res.* **11**, 3609–3613 (2005).

89. Piaggio, F. *et al.* In uveal melanoma Gα-protein GNA11 mutations convey a shorter disease-specific survival and are more strongly associated with loss of BAP1 and chromosomal alterations than Gα-protein GNAQ mutations. *Eur. J. Cancer Oxf. Engl. 1990* **170**, 27–41 (2022).

90. Nguyen, J. Q. N. *et al.* 8q Gain Has No Additional Predictive Value in SF3B1MUT Uveal Melanoma but Is Predictive for a Worse Prognosis in Patients with BAP1MUT Uveal Melanoma. *Ophthalmol. Sci.* **4**, 100413 (2024).

91. da Silva, V. *et al.* CNVRanger: association analysis of CNVs with gene expression and quantitative phenotypes. *Bioinforma. Oxf. Engl.* **36**, 972–973 (2020).

92. Lai, Y.-P. *et al.* iGC-an integrated analysis package of gene expression and copy number alteration. *BMC Bioinformatics* **18**, 35 (2017).

93. Luo, P., Duan, J. & Chen, Q. PTK2 promotes uveal melanoma metastasis by activating epithelial-to-mesenchymal transition. *PTK2 promotes uveal melanoma metastasis by activating epithelial-to-mesenchymal transition* vol. 2 (2023).

94. Liang, F., Lu, X., Wu, B., Yang, Y. & Qin, W. Nucleolar Protein 56 Deficiency in Zebrafish Leads to Developmental Abnormalities and Anemia via p53 and JAK2-STAT3 Signaling. *Biology* **12**, 538 (2023).

95. Liu, C.-H. *et al.* Melanin Bleaching With Warm Hydrogen Peroxide and Integrated Immunohistochemical Analysis: An Automated Platform. *Int. J. Surg. Pathol.* **26**, 410–416 (2018).

96. Yeh, C.-C., Li, Y.-J., Liang, J.-S. & Liao, J.-B. Evaluation of the effects of melanin bleaching in different steps of immunohistochemistry on an automated platform. *Pathol. Res. Pract.* **271**, 156047 (2025).

97. Talevich, E., Shain, A. H., Botton, T. & Bastian, B. C. CNVkit: Genome-Wide Copy Number Detection and Visualization from Targeted DNA Sequencing. *PLoS Comput. Biol.* **12**, e1004873 (2016).

98. Van Loo, P. *et al.* Allele-specific copy number analysis of tumors. *Proc. Natl. Acad. Sci. U. S. A.* **107**, 16910–16915 (2010).

99. Pandiani, C. *et al.* Single-cell RNA sequencing reveals intratumoral heterogeneity in primary uveal melanomas and identifies HES6 as a driver of the metastatic disease. *Cell Death Differ.* **28**, 1990–2000 (2021).

100. Mazloumi, M. *et al.* Accuracy of The Cancer Genome Atlas Classification vs American Joint Committee on Cancer Classification for Prediction of Metastasis in Patients With Uveal Melanoma. *JAMA Ophthalmol.* **138**, 260–267 (2020).

101. Shain, A. H. *et al.* The genetic evolution of metastatic uveal melanoma. *Nat. Genet.* **51**, 1123–1130 (2019).

102. Grossniklaus, H. E. Understanding Uveal Melanoma Metastasis to the Liver: The

Zimmerman Effect and the Zimmerman Hypothesis. *Ophthalmology* **126**, 483–487 (2019).

103. Royer-Bertrand, B. *et al.* Comprehensive Genetic Landscape of Uveal Melanoma by Whole-Genome Sequencing. *Am. J. Hum. Genet.* **99**, 1190–1198 (2016).

104. Vivet-Noguer, R., Tarin, M., Roman-Roman, S. & Alsafadi, S. Emerging Therapeutic Opportunities Based on Current Knowledge of Uveal Melanoma Biology. *Cancers* **11**, 1019 (2019).

105. Tsuchida, K., Sakiyama, N., Ogura, Y. & Kobayashi, M. Skin lightness affects ultraviolet A-induced oxidative stress: Evaluation using ultraweak photon emission measurement. *Exp. Dermatol.* **32**, 146–153 (2023).

106. Wang, H. *et al.* LAPTM4B-mediated hepatocellular carcinoma stem cell proliferation and MDSC migration: implications for HCC progression and sensitivity to PD-L1 monoclonal antibody therapy. *Cell Death Dis.* **15**, 165 (2024).

107. Yang, Y. *et al.* The role and regulatory mechanism of lysosome associated protein transmembrane 4β in tumors. *Front. Oncol.* **15**, 1552007 (2025).

108. Li, Y. *et al.* Amplification of LAPTM4B and YWHAZ contributes to chemotherapy resistance and recurrence of breast cancer. *Nat. Med.* **16**, 214–218 (2010).

109. Choi, S. *et al.* Novel Prognostic Factor for Uveal Melanoma: Bioinformatics Analysis of Three Independent Cohorts. *Anticancer Res.* **40**, 3839–3846 (2020).

110. Kuse, Y. *et al.* Damage of photoreceptor-derived cells in culture induced by light emitting diode-derived blue light. *Sci Rep* **4**, 5223 (2014).